Enhancing Room Temperature Phosphorescence from Organic Molecules by Internal Heavy Atom Effect and External Agents

by

Jaehun Jung

A dissertation submitted in partial fulfillment
of the requirements for the degree of
Doctor of Philosophy
(Macromolecular Science and Engineering)
in The University of Michigan
2018

Doctoral Committee:

Professor Jinsang Kim, Chair
Professor Theodore Goodson III
Professor L. Jay Guo
Professor John Kieffer

@Jaehun Jung
jaehunj@umich.edu
ORCID ID: 0000-0002-5859-3027

2018

Acknowledgement

First, I would like to thank Professor Kim. When I was visiting scholar, he gave me not only insightful advice but also passion on research. After I joined in his group, he always encouraged me and suggested to learn knowledge of a variety of research fields which is helpful to develop my research careers. Although I was trouble to my health during Ph.D. study, I could finish the study thanks for him. I really can't thank enough for his professional and personal supports.

Secondly I must thank my friend and colleague, Dr Minsang Kwon. As senior and Post.doc, he taught me organic chemistry and chemical synthesis. It was the happiest moment in my Ph.D. that we studies and taught each other about photochemistry. Without him, I cannot imagine that I am graduated. Thanks Minsang.

I would like to express my gratitude to my collaborators, Jialiu Ma, Dr. Daniel Hashem, Dr. Huan Wang and Dr Johannes Gierschner. During the collaboration, I got research achievements as well as the opportunities to work with them could expand research into other knowledge arenas.

Of course, I thank the members of our research group. In particular, Dr Dongwook Lee, Dr. Kyeongwoon Chung, Dr Sungbaek Seo and Deokwon Seo helped me to adapt my life to a new school. I thank Dr. David Bilby, Dr Apoorv Shanker for their contribution. I learned great ownership from Dr. David Bilby and Dr Apoorv Shanker and thank their sacrifice of time for lab maintenance. I own thanks to Da Seul Yang and JoonKoo Kang. Also I thank other group members and visiting members for kind assistance.

I would like to add a word of gratitude to my family. I am most grateful to my parents and my sister for supports and encouragement. My wife, Anna Jo, sacrificed a lot of times and just supported me to spend much time for experiments. I Know she felt lonely in Ann Arbor life. I feel sorry and thank her sacrifice. I could finish my Ph.D due to her support and patience. Thanks Anna.

Table of Contents

List of Figures

List of Tables

List of Schemes

Abstract

Room temperature phosphorescence has gained a great deal of attention due to its significant importance in practical application such as phosphorescence organic light emitting diode (PhOLED). Bright room temperature phosphorescence has also been utilized in the field of bio-imaging and oxygen indicators which were not practically achievable by using phosphorescent materials. Heavy-metal complexes such as iridium complex are commonly used for room temperature phosphorescence but their potential toxicity and instability particularly in case of blue phosphors still remain to be solved. Room temperature phosphorescence from metal-free organic phosphors has attracted much attention in recent years since metal-free phosphors were presented as bright as organometallic compounds, quantum dots, and fluorescent molecules at room temperature.

In previous study, our group focused on the development of host-guest systems to suppress vibration of phosphors such as doped crystal, amorphous rigid polymer and immobilization between polymer and phosphors via hydrogen bonding or covalent bonding. However, the quantum yield is still much lower than that of conventional fluorescent dyes. For example, the best quantum yield of room temperature phosphorescence is around 30% in polymer matrix. The low quantum yield prevents it from utilizing real phosphorescent applications.

In this dissertation, we focused on how to improve further phosphorescence quantum yield by improving phosphorescence radiative decay as well as suppressing non-radiative decay. First, general molecular design principles to achieve bright room temperature phosphorescence from metal-free organic phosphors are thoroughly discussed. By synthesizing a series of molecules and analyzing their photophysical properties, we discovered how molecular structures affect the non-radiative decay pathway by intramolecular vibration, and both phosphorescent radiative decay and non-radiative decay by intermolecular vibration. Molecular design strategies to tune the phosphorescent color without significantly decreasing the phosphorescence quantum yield were also discussed. We also developed a new scheme to improve the phosphorescent radiative decay and consequently enhance the emission intensity by incorporating an external component such as plasmonic nanometals and adapting metal organic frameworks (MOFs). Through a systematic

investigation on localized surface plasmon resonance (LSPR) based phosphorescence enhancement, we built insightful understanding on the LSRP based phosphorescence enhancement mechanism and revealed optimized conditions to achieve brightest phosphorescence. Finally, MOF was investigated with organic phosphor molecules as an organic ligand. MOF-polystyrene (PS) composite having a organic phosphor ligand produced bright room temperature phosphorescence by suppressing molecular vibrational dissipation and enhancing the phosphorescent radiative decay. A summary of future perspective of metal-free organic phosphors to overcome their limitations and to realize futuristic potential applications is provided in the last chapter of the dissertation.

Chapter 1

Introduction and background

This chapter describes the fundamental theory of phosphorescence by explaining photoluminescence transitions and spin states. It illustrates the unique features of phosphorescence that affect fluorescence as well as allow potential applications of phosphorescent materials. Recent progress in metal-free phosphors is presented using known design principles and methods to achieve bright room-temperature phosphorescence have also been briefly reviewed, and future research objectives for metal-free phosphors have been suggested. We believe the discussion presented in this chapter give readers proper background information and importance of the metal-free phosphors.

1.1 Phosphorescence and Fluorescence

Photoluminescence is formally divided into two categories: fluorescence and phosphorescence. The definitions of fluorescence and phosphorescence are different depending on inorganic and organic materials. In inorganic dyes, fluorescence is considered as a narrow-full-width at half-maximum (FWHM) emission with a fast lifetime (~ns) and phosphorescence is generally considered as a broad and long-life time emission (<μs). Compared to inorganic, an organic exciton, the so-called Frenkel exciton, is the bound state of the hole and electron. Therefore, the electron configuration of the excited state of organic molecules can be determined, which then determine either fluorescence or phosphorescence.

To understand the novelty of the work presented here, photoluminescence pathway and the concept of electron configuration in organic molecules must be understood. In this chapter, I described the phosphorescence process and their unique features compared to fluorescence and then explained in more complete descriptions by quantum mechanical basis about phosphorescence.

1.1.1 Triplet state

An exciton is a pair of hole and electron or a pair of electron on the HOMO (highest-occupied molecular orbital) and LUMO (lowest-unoccupied molecular orbital). When two

electron spins are anti-parallel or anti-symmetry (↑↓) and the net spin is zero, we call the spin configuration a singlet. If spin is parallel (↑↑) and the net spin is one, it is called a triplet. Generally, the ground state of molecules is in the singlet state. Mostly, only one HOMO having two electrons exists and only the singlet state of electrons can occupy the HOMO owing to the Pauli exclusion principle. A notable exception is oxygen, which has two degenerated HOMOs with two electrons.

When uncorrelated hole and electron are injected into HOMO and LUMO, respectively, and form an exciton, they can have four possible orientations of their collective spin: one singlet and three degenerated triplets. In quantum mechanics, the wavefunction of a singlet is described as

$$\frac{1}{\sqrt{2}}(|\uparrow\downarrow> - |\downarrow\uparrow>)$$

Further, the wavefunctions of a triplet are described as

$$\frac{1}{\sqrt{2}}(|\uparrow\uparrow> + |\uparrow\uparrow>), \qquad \frac{1}{\sqrt{2}}(|\uparrow\downarrow> + |\downarrow\uparrow>), \qquad \frac{1}{\sqrt{2}}(|\downarrow\downarrow> + |\downarrow\downarrow>)$$

For an electroluminescence device or exciton combination from charges, 75% triplet and 25% singlet are generated. Therefore, phosphorescent organic light-emitting diodes (OLEDs) are much more efficient than fluorescence OLEDs because phosphorescent OLEDs can use 75% more excitons.

1.1.2. Photoluminescence pathways

To understand the difference between fluorescence and phosphorescence in organic molecules, the Jablonski diagram must be understood. Fig 1.1 shows a Jablonski diagram including vibration levels that illustrate the electronic states of molecules and the transition between them. The vertical coordination is arranged by energy and the grouped horizontal state is arranged by the electron spin configuration.

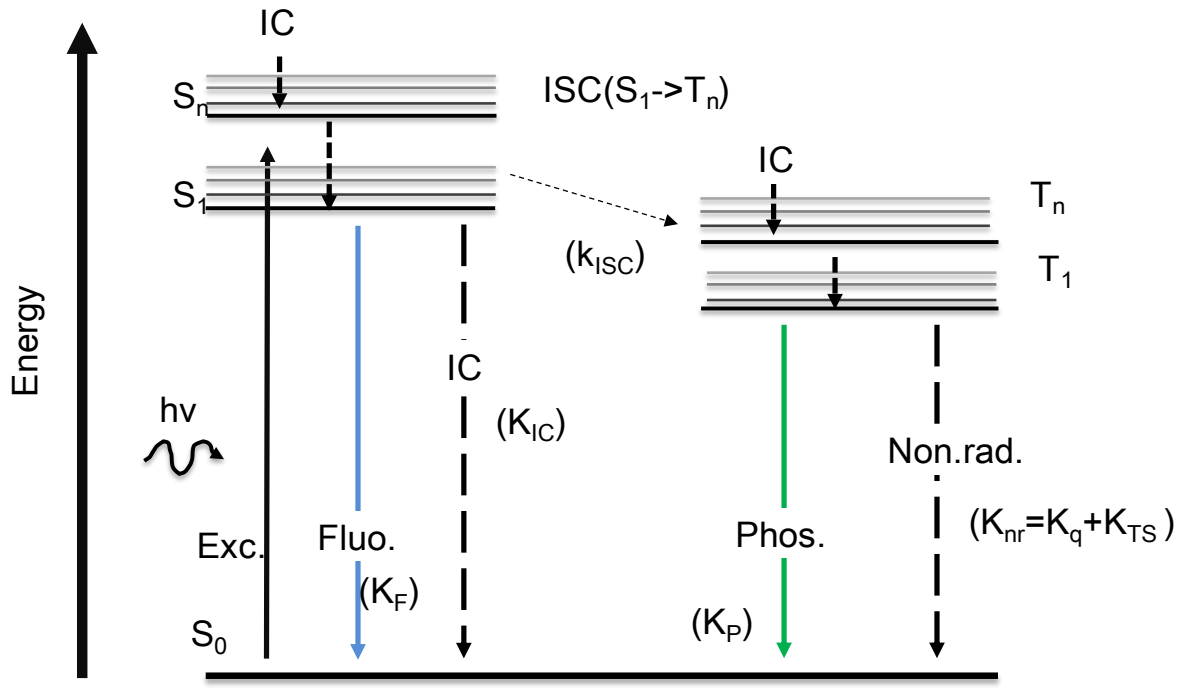

Figure 1.1 Jablonski diagram including vibrational transitions. Radiative transitions such as absorption and emission are identified by solid arrow. Non-radiative transitions are identified by dashed arrow. S_0 is the ground state of singlet molecules. S_n is the higher energy level of singlet states. T_n is the energy level of triplets.

The first transition in the diagrams is the photon *absorption* that an electron of the molecule is excited from a ground level (S_0) to a higher energy level, as much as the particular energy of the absorbed photon. Absorption is the subset of excitation. Only certain wavelengths of light can be absorbed because for efficient absorption the energy of a photon should correspond to the energy difference between the two energy levels. Specifically, the energy difference between the eigenstates of the molecules because of the electronic level is coupled with the vibrational levels. Absorption transition exclusively or mostly occurs from S_0 to S_n, not from S_0 to T_n owing to the selection rule ($\Delta S=0$). The total momentum of molecules has to be conserved after the absorption of light, which has a one-integer angular momentum. Even though some metal complexes show S_0 to T_n transition during absorption, S_0 to S_n is much more dominant.

The absorption process is a very fast transition, on the order of 10^{-15} seconds. Therefore, absorption is vertically transitioned without the change in molecular geometry. After the excitation and vibrational energy relaxation, the molecular geometry changes to a more thermodynamically stable one in the excited state. This process is called *internal conversion*

(IC). Internal conversion typically occurs on vibrational levels. Owing to the small energy of vibrational levels (100 cm^{-1}), the transition is very fast, on the order of 10^{-14} to 10^{-11} seconds, which is extremely likely to occur immediately following the absorption.

The S_n to S_{n-1} transition can occur from a vibration level in S_n to another vibration level in S_{n-1} state because vibration energy levels can strongly overlap two electronic energy levels. This process is also called internal conversion and is identical to vibration relaxation. Although a molecule can be excited to various excited states by absorbing photon energies, the higher-order state most likely quickly relaxes to the S_1 state, a phenomenon known as *Kasha's rule*. The only exception of Kasha's rule is that vibration levels of S_2 and S_1 are not likely to overlap because of the large energy difference between them. Therefore, S_1 is generally considered as the excited state from which the emission comes.

When the excited electron is relaxed to S_1, the three possible subsequent processes compete with each other: *fluorescence*, internal conversion, and *Intersystem crossing* (ISC). The fluorescence of organic molecule is a radiative decay transition between an excited singlet to a ground state of singlet. Fluorescence is a slower process, on the order of 10^{-9} to 10^{-6} seconds (~ns), than internal conversion from S_n to S_{n-1}; thus, the wavelength of fluorescence is generally matched to the energy gap between S_1 to S_0. In general, when the orbital configurations of the excited state and the ground state are similar, the rate of fluorescence (k_F) is high (high oscillation strength). Because of the energy loss from the vibration relaxation before fluorescence, the wavelength of absorption is different from that of fluorescence, and the wavelength difference is called *Stokes shift*. The speed of internal conversion from S_1 to S_0 is comparable to that of fluorescence but slower than that of IC from S_n to S_{n-1} owing to a much larger energy difference of the internal conversion. If a molecule has many vibrational modes and rotational modes, the internal conversion process is largely facilitated, resulting in fluorescent quenching. The internal conversion can be affected by various environmental factors such as solvent. The third common route to singlet relaxation is *intersystem crossing* (ISC), a non-radiative decay process involving a transition between the two electronic states with different state spin multiplicity. The singlet excited state of a molecule can be converted to the triplet state by changing the electron spin. However, the spin flipping violates the law of conservation of angular momentum and is therefore forbidden by the selection rule. Hence, the intersystem crossing from singlet S_n to T_n is very slow and typically not competitive with fluorescence and internal conversion unless there is an applied external energy. Consequently, in many cases the triplet state cannot be accessible

by photoexcitation.

Spin-orbit coupling is the term to express the electromagnetic interactions between the electrons' spin and the induced magnetic field generated by the electrons' orbiting around the nucleus. Strong spin-orbit coupling can change the selection rule from $\Delta S=\pm 0$, $\Delta L=1,-1$ to $\Delta J(S+L)=0,\pm 1$ and enables the spin flipping. Generally, the electron's orbiting around a heavy nucleus can generate strong magnetic fields, which leads to largely enhanced spin-orbit coupling. Intersystem crossing of the molecules having strong spin-orbit coupling is much faster than or compatible with fluorescence and/or internal conversion, on the order of 10^{-12} to 10^{-9} seconds. Because intersystem crossing occurs between vibrational levels of the singlet and triplet, the rate (k_{ISC}) becomes higher when the energy difference between the two electronic states is small. More details of spin-orbit coupling and the rate of intersystem crossing will be described in Chapter 1.3.

Once the singlet electron flips its spin through the intersystem crossing, the electron at T_n state relaxes to T_1 state via fast internal conversion. Then two possible relaxations from T_1 state to the ground state compete with each other: radiative decay of phosphorescence (k_p) and non-radiative decay via lattice vibration and heat generation (k_{nr}). Because of the conservation law of angular momentum and selection rule, basically phosphorescence is a forbidden transition. Therefore, phosphorescence is much slower and observed on a much longer timescale than fluorescence. For metal-free organic molecules, phosphorescence lifetime is typically in the range of microseconds to seconds depending on the strength of the spin-orbit coupling.

The non-radiative decay process from T_1 to S_0 consists of two possible components: intersystem crossing from T_1 to S_0, so called the *intramolecular vibration* (k_{TS}), and the Dexter-type triplet-triplet energy transfer, so called the *intermolecular collisional quenching* (k_q)[1]. Intersystem crossing from T_1 to S_0, a forbidden transition, is a vibrational relaxation and is thus similar to the internal conversion except for the required spin-flipping. Therefore, the intersystem crossing is influenced by vibration modes and the spin-orbit coupling. Further, spin-orbit coupling promotes not only the phosphorescence radiative decay process but also the intersystem crossing simultaneously. The details of intramolecular vibration will be described in Chapter 1.3.

Owing to the much longer lifetime of the triplet state, the excited state of molecules has more chances to collide to their surroundings before the triplet exciton relaxes to the ground state. During the collision, the triplet energy of molecules can move to the triplet state of the

surroundings such as solvent molecules or a polymer matrix. The rate of the process follows the Arrhenius equation. Owing to the weak spin-orbit coupling of organic molecules, the intermolecular collisional quenching is dominant against the intramolecular vibration quenching during the intersystem crossing at room temperature (in general, $k_q >> k_{TS}$). Therefore, the suppression of the intermolecular collisional quenching is crucial to reduce the non-radiative decay and to achieve bright phosphorescence from organic molecules. For example, phosphorescence from organic molecules is generally observed at only low temperatures because molecular motions can be restricted at a low temperature thereby suppressing the collisional vibration. In contrast, organometallic compounds, such as Ir complexes, can emit bright phosphorescence with a very fast nanosecond lifetime that are not sensitive to temperature and the environment ($k_{TS} >> k_q$) because of their strong spin-orbit coupling induced by heavy metals. The details of the intermolecular vibration quenching will be discussed in Chapter 1.3.

Now we can understand the photoluminescence process, especially the phosphorescence, and the competitive processes. The nature of the triplet state gives molecules unique properties: 1) varying phosphorescence lifetime depending on spin-orbit coupling, 2) sensitivity to oxygen, and 3) sensitivity to the environment. These features can be utilized as design parameters to devise bright phosphorescence materials and a wide variety of applications such as sensing and imaging.

1.1.3 Phosphorescence quantum yield, lifetime, and kinetic constants

In this section, I will briefly explain the definition of phosphorescence quantum yield, phosphorescence lifetime, and how the kinetic constant of each transition can be obtained from experimental data.

The phosphorescence quantum yield is defined as

Φ_p= #(photon of phosphorescence)/#(photon of absorbance)

The photoluminescence process is as follows:

$$[I]^* \rightarrow [I]^0 + hv$$

The rate is expressed as

$$\text{Rate} = d[I]/dt = k[I]$$

Finally, the time-dependent luminescent intensity equation is

$$I = I^0 e^{-(t/\tau)}$$

From the measurement of the phosphorescence emission intensity, we can obtain the phosphorescence *lifetime* τ, by plotting the emission intensity versus time and fitting the data.

For photoluminescent kinetics, the quantum yields are defined as

$$\Phi_f = \frac{k_f}{k_f+k_{ISC}+k_{IC}}, \Phi_{ISC} = \frac{k_{ISC}}{k_f+k_{ISC}+k_{IC}}, \Phi_p = \Phi_{ISC}\frac{k_p}{k_p+k_{nr}} = \Phi_{ISC}k_p\tau_p, \tau_p = \frac{1}{k_p+k_{nr}},$$

Φ_f: fluorescence quantum yield
Φ_{ISC}: ISC from S to T yield
Φ_p: phosphorescence quantum yield
τ_f: phosphorescence lifetime
k_f: fluorescence radiative decay rate constant
$k_{ISC:}$ intersystem crossing rate constant
k_{IC}: Internal conversion rate constant
k_{nr}: non-radiative decay rate constant
k_p: phosphorescence radiative decay rate constant

Molecular oxygen is a small, non-polar, paramagnetic molecule, having a diradical electron spin or a triplet state on the ground state. Therefore, oxygen can take the energy from the triplet state of neighboring molecules and quench their phosphorescence emission. The 20.8% of oxygen in air effectively quenches the phosphorescence emission limits the utility of phosphorescent materials for applications requiring bright emission. However, this oxygen quenching phenomenon can be usefully implemented in bio-sensing and imaging applications because oxygen is of significant importance for living organisms and its level is quite relevant to the human cell activity.

Very recently, many research groups have demonstrated phosphorescent imaging based on oxygen concentration using metal-free phosphors[2-4]. This research field will grow rapidly because metal complexes have the unknown toxicity issue due to the transition metal inclusion and no conventional phosphorescent molecules are used in bio-applications. In this chapter, I will discuss the principle of phosphorescence quenching via oxygen and their potential applications.

1.2 Oxygen quenching

1.2.1 Quantum chemistry of oxygen

The ground state of molecules is generally singlet because a HOMO or each HOMO is filled by two electrons. The two electrons are anti-symmetrical owing to the Pauli exclusion principle. As shown in Fig 1.2 (right), a fluorine molecule has two HOMOs with four filled electrons. Therefore, the molecules exhibit a ground singlet state in general. Oxygen is a

notable exception. The molecular configuration is such that each electron occupies each HOMO.

The electrons are symmetrical because of the energetically stable state based on Hund's rule of maximum multiplicity[5]. Therefore, oxygens are paramagnetic molecules and have the unique ground triplet state.

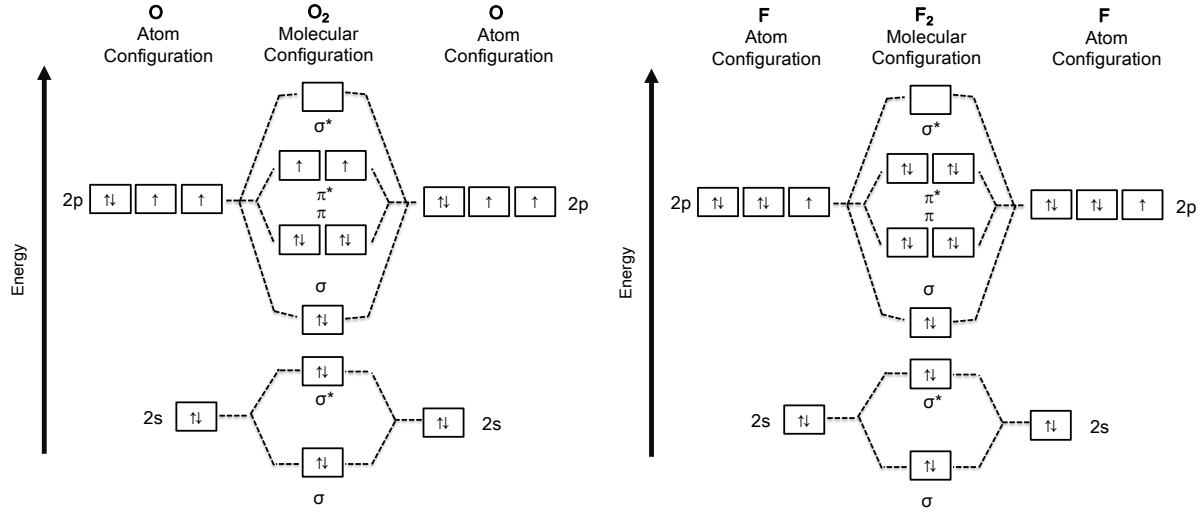

Figure 1.2 Molecular orbital configuration and spin state. Left is oxygen and right is fluorine.

1.2.2 Energy transfer mechanism

The energy transfer could take place via the interactions between a donor molecule and an acceptor molecule, excited molecules, and ground-state molecules without emitting a photon. Generally, two energy transfer processes are referred: the Forster energy transfer and the Dexter energy transfer. The Forster energy transfer is a mechanism where a donor molecule may transfer energy to an acceptor via through the space, long-range, dipole–dipole interactions. This phenomenon is similar to re-absorption except for photon emission. The efficiency of the Forster energy transfer is inversely proportional to the sixth power of the distance between two molecules.

The Dexter energy transfer is a mechanism describing energy transfer between the donor and acceptor via the exchange of electrons. Because of the electron exchange mechanism, it can only occur at a much shorter distance compared to the Forster energy transfer.

Fig 1.3 describes the possible energy transfer considering the molecules' spin multiplicity. The Forster energy transfer only allows a singlet-to-singlet energy transfer. Triplet-to-singlet and singlet-to-triplet are forbidden by both the Forster energy transfer and Dexter energy

transfer due to the Wigner conservation spin law. Triplet-to-triplet energy transfer is also forbidden by the Forster energy transfer because of dipole–dipole coupling mechanism, meaning that the ground singlet state to the excited triplet state transition of an acceptor is forbidden by the selection rule.

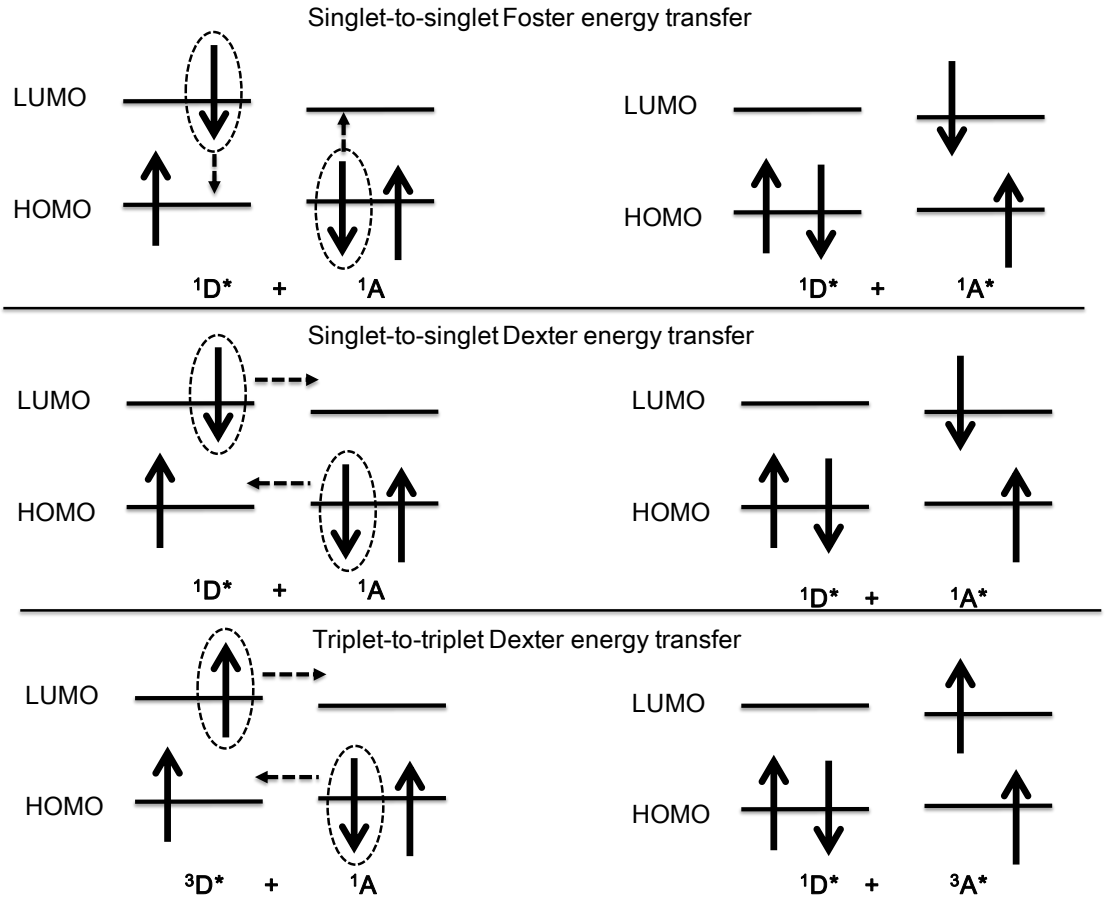

Figure 1.3 Schematic diagram for the Foster and Dexter energy transfer.

Both singlet-to-singlet and triplet-to-triplet energy transfer are allowed by the Dexter energy transfer. Because of the electron exchange mechanism, the mechanism does not follow the selection rule. In general, the distinction between the two mechanisms is not important in photochemistry but the Dexter mechanism is very important in photochemistry, and recently, in EL devices. As described in chapter 1.1.1, 75% triplet and 25% singlet exciton are generated via charge recombination in EL devices. To design 100% exciton energy efficiency, the Dexter energy transfer must be realized.

1.2.3 Singlet oxygen generation and phosphorescence quenching

It is well known in the field of phototherapy that ground-state triplet oxygen molecules

convert the excited triplet state via energy transfer from the excited state of triplet molecules. As shown in Fig 1.4, molecules can generate the triplet state via intersystem crossing after photo-absorption. Before emitting phosphorescence, the triplet state of a molecule can relax to the ground singlet state without emitting phosphorescence via energy transfer to oxygen. This process is called photosensitization.

This phenomenon causes phosphorescence quenching under oxygen or air environment. The detailed energy transfer mechanism is not clearly understood yet. Because of the ground triplet state of oxygen, triplet-to-singlet energy transfer from molecules to oxygen becomes an allowed transition by the Wigner conservation spin law. The widely accepted mechanism for the singlet oxygen generation via energy transfer is the Dexter energy transfer, an electron exchange mechanism,[6] because triplet-to-singlet transition is a forbidden transition. The probability of absorption or the oscillation strength of the triplet-to-singlet transition of oxygen molecule looks weak. However, the spin-orbit coupling of oxygen is relatively strong and thus the phosphorescence lifetime of oxygen is in the order of microseconds. Several studies claimed that the rate of the energy transfer is faster than the expected rate of the Dexter energy transfer, which implies that the Forster energy transfer mechanism is also valid for singlet oxygen generation.[7,8]

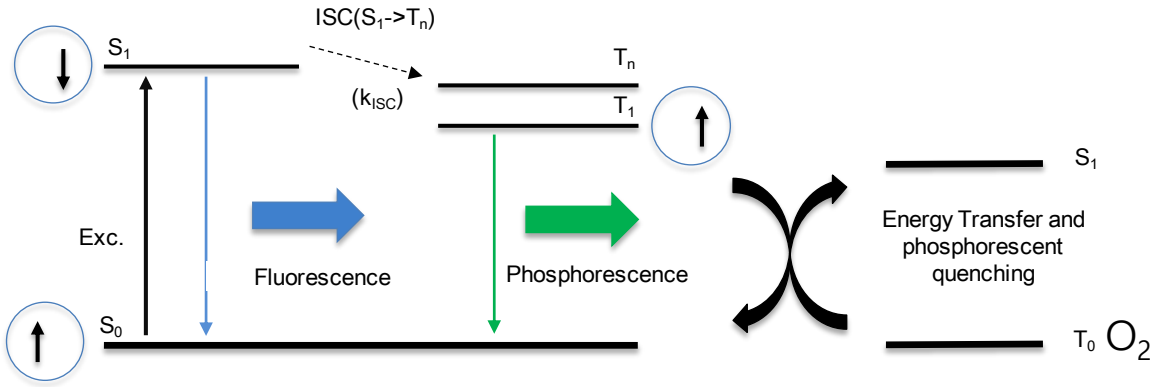

Figure 1.4 Schematic Jablonski diagram for singlet oxygen generation.

1.2.4 Applications of phosphorescent molecules: bio-imaging

Compared to fluorescent imaging, phosphorescent materials can provide high-resolution images because the longer lifetime of phosphorescence can exclude noise signals such as background noise. For example, a microsecond phosphorescence can be selectively recorded after complete decay of the scattering from the excitation pulse and the autofluorescence having a nanosecond lifetime from the environmental cells. However, phosphorescence from

metal-free organics is very sensitive to environment conditions. For example, 20.8% oxygen in atmospheric air causes phosphorescence quenching and hinders bright phosphorescent images.

Very recently, Pu el al. demonstrated the proof of concept application of metal-free phosphors nano-crystals with ultralong phosphorescence for in-vivo afterglow imaging.[3,9] Because of the ultralong phosphorescence lifetime, the luminescent signal can be detected after the removal of external light source (Fig 1.5a). Phosphorescence from the crystal is inert to oxygen owing to its low oxygen permeability. Through a top-down formulation of the nano-crystal inside polymer nanoparticles, the phosphorescence of the nanoparticles renders the bright imaging of lymph nodes in living mice under ambient conditions (Fig 1.5b). With a high resolution due to the elimination of tissue autofluorescence (Fig 1.5c), the nanoparticle allows the afterglow mapping of lymph nodes in living mice at a high signal-to-noise ratio of 40 (Fig 1.5d). This study shows the possibility and the advantage of phosphorescence applications in bio-imaging. However, the maximum excitation and emission wavelengths are less than 600 nm, which cannot penetrate the tissues.

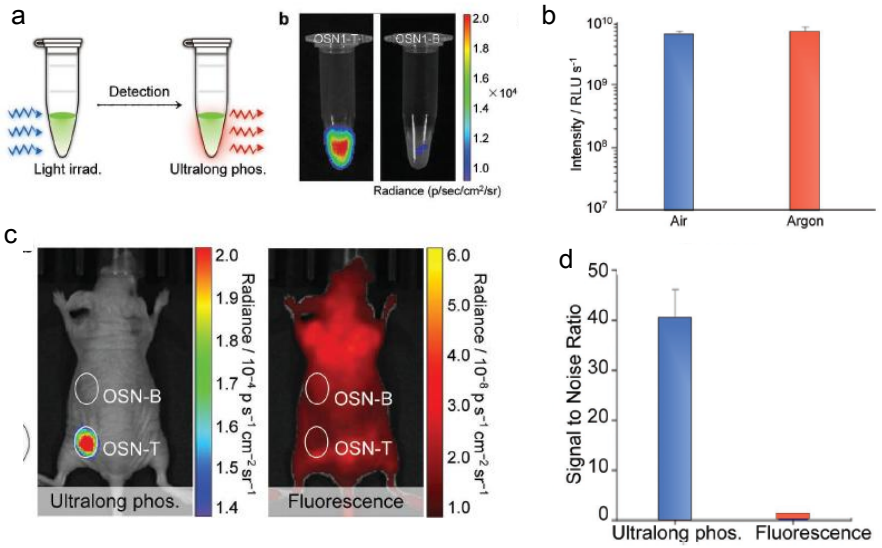

Figure 1.5 A sampling of phosphorescent bio-imaging (a) Schematic illustration of activation and detection of ultralong phosphorescence in solution (b) The ultralong phosphorescence intensities of OSN1-T solution purged with air or argon (c) Ultralong phosphorescence and fluorescence imaging of a mouse with the subcutaneous inclusions of nanoparticles including phosphorescent nanocrystal (d) Signal-to-noise ratio for ultralong phosphorescence and fluorescence imaging of lymph node in living mice. Images from Zhen *et al. Adv. Mater.* **2017**, 1606665.

1.2.5 Applications of phosphorescent molecules: oxygen indicator

Owing to the oxygen quenching, the phosphorescent intensity is strongly affected by the oxygen concentration. The high oxygen sensitivity of phosphorescence enables human activity tracking and provides tissue oxygen mapping. For example, the Fraser group demonstrated the map of a tumor cell which is hypoxia because the cell consumes oxygen enormously[3]. Because of the unique feature of dual fluorescent and phosphorescent dyes, they can obtain hypoxia oxygenation mapping based on fluorescence and phosphorescence ratio (Fig 1.6). Fluorescence is a reference signal to measure the relative intensity of phosphorescence indicating oxygen concentration.

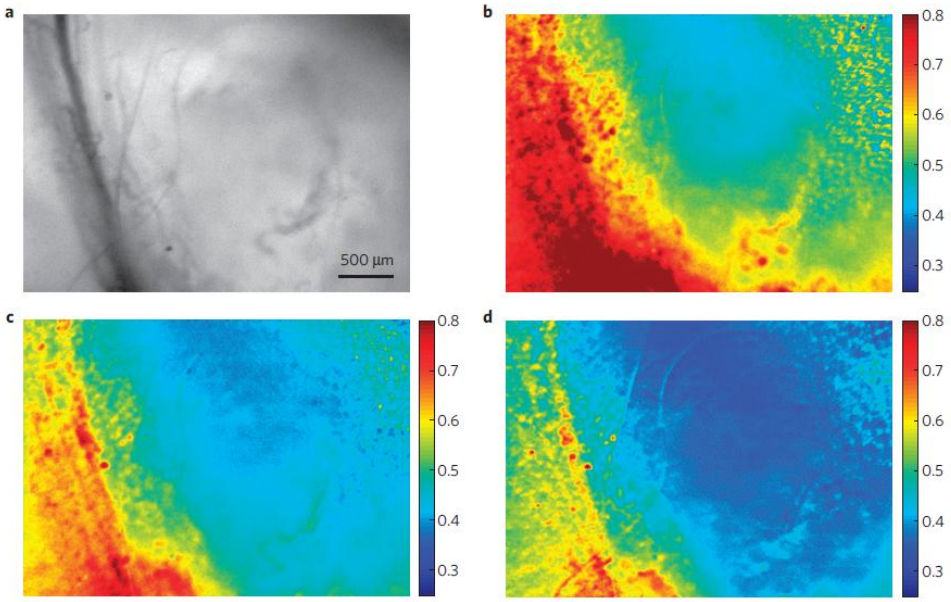

Figure 1.6 Tumor hypoxia imaging with phosphorescent nanoparticles. (a) Bright-field image. Fluorescence/phosphorescence ratio mapping with (b) 95% O_2, (c) 21% O_2, and (d) 0% O_2. Images from Zhang *et al. Nat. Mater*. **2009**, 8, 747.

Another method to map oxygen concentration using a phosphorescence signal is to measure the lifetime of the samples rather than just the intensity[10]. This method is more common than the measurement of intensity because an intensity signal can vary depending on the dye concentration (Fig 1.7). Oxygen leads to the increase in non-radiative decay and the decrease of phosphorescence lifetime; thus, oxygen concentration can be imaged via the Stern–Volmer calibration plot[11].

Phosphorescent metal complexes have intrinsic drawbacks for bio-imaging and oxygen sensing. First, they have the unknown toxicity issue in the human body owing to the

transitional metal inclusion[12]. Next, the metal complex does not show fluorescence generally because of very strong spin-orbit coupling, prevenging a ratiometic detection. In contrast, metal-free phosphors have relatively strong fluorescence that can be used as a reference signal against a phosphorescence signal. For these reasons, metal-free phosphors are much desirable for bio-applications. However, the wavelength of excitation and the emission of the reported bright molecules are less than 650 nm, preventing *in vivo* imaging.

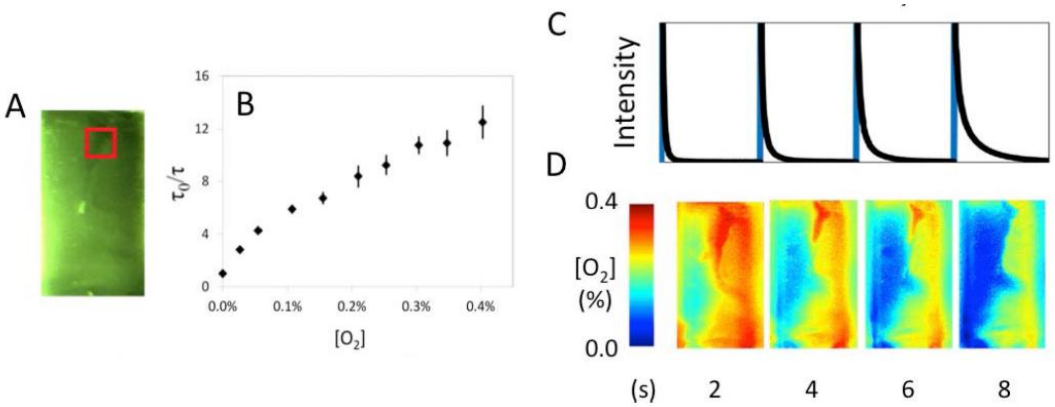

Figure 1.7 A mapping of phosphorescence lifetime. a) Image of phosphorescence with the region of interesting highlighted in a red box, b) Stern–Volmer calibration plot, and c) raw camera intensity plot of a region of interest during imaging aligned with d) the fully processed oxygen color maps. Image from Mathew *et al., Anal Methods*. **2016**, 8, 3109–3114.

1.3. Rate of intersystem crossing from singlet to triplet (k_{ISC})

Intersystem crossing is the non-radiative transition between two electronic states of different multiplicities. The transition is formally forbidden in the non-relativistic quantum theory. To realize the transition, spin-orbit coupling (SOC) has to be invoked. Both the intersystem crossing from singlet to triplet and phosphorescent transition require the electron spin flipping and thus the molecular design to achieve strong spin-orbit coupling is one of the critical parameters to develop bright phosphorescence.

Several formalisms are given[13] in literature for estimating the ISC rate. The most simplified form is given as[14]

$$k_{ISC} \propto \frac{< S_k|H_{so}|T_n >^2}{(\Delta E_{ST})^2},$$

where, H_{so} is the spin-orbit operator for calculating the coupling between the k^{th} singlet S^k

and the n^{th} triplet state T_n, and ΔE_{ST} is the energy difference between the two states. In this section, the molecular design to obtain high k_{ISC} or strong spin-orbit coupling will be simply described. For more complete descriptions of the quantum mechanical basis of spin-orbit coupling and k_{ISC}, see the cited reference[15].

1.3.1 El-Sayed's rules

The El-Sayed's rule states that the rate of intersystem crossing is fast when the radiation-less transition involves a change in orbital type. For example, the intersystem crossing from $^1(\pi,\pi*)$ to $^3(n,\pi*)$ is faster than the intersystem crossing from $^1(\pi,\pi^*)$ to $^3(\pi,\pi^*)$. Therefore, ISC from $^1(\pi,\pi*)$ to $^3(n,\pi*)$ is an somewhat allowed transition and the intersystem crossing from $^1(\pi,\pi*)$ to $^3(n,\pi*)$ is a forbidden transition by El-Sayed's rule (note that it is true when the heavy-atom effect or other spin-orbit coupling processes are not involved).

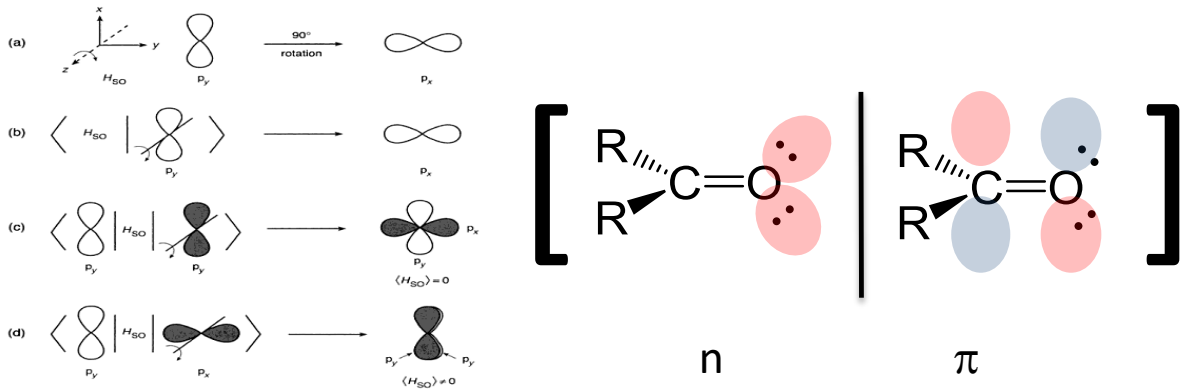

Figure 1.8. Orbital description with spin-orbit coupling operator. Image from N.J. Turro, *Modern Molecular Photochemistry* 1978.

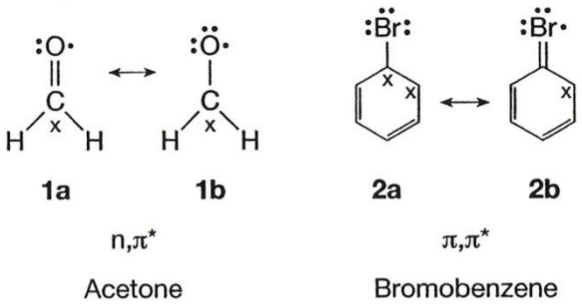

Figure 1.9 Lewis structure representations of the n, π^*state of acetone and the π,π^*state of bromobenzene.

The rule is fairly easily explained from the mathematical structure of the spin-orbit coupling operator. The Hamiltonian (H_{so}) can be split into two: pure imaginary operator and heavy-atom constant (or operator governed by the interaction of the electron's spin and the magnetic field generated by the electrons' orbiting around the nucleus). The pure imaginary operator rotates an orbital wavefunction at 90° (Fig 1.8b). Therefore, $^1(\pi,\pi*)$ to $^3(\pi,\pi*)$ is forbidden because the spin-orbit coupling operator couples the out-of-plane π orbitals and becomes zero. In contrast, the spin-orbit coupling operator couples the out-of-plane π orbital and the in-plane n orbital, resulting in strong spin-orbit coupling and allowing $^1(\pi,\pi*)$ to $^3(n,\pi*)$ or $^1(n,\pi*)$ to $^3(\pi,\pi*)$ transition.

Benzophenone (Fig 1.10,left) is a well-known photosensitizer molecule. The intersystem crossing occurs from S_1 $^1(n,\pi*)$ to T_2 $^3(\pi,\pi*)$, which is allowed by the El-Sayed rule. The rate of intersystem crossing of benzophenone is faster than 10^9 s, a comparable scale of rate of fluorescence. The intersystem crossing of acetone (Fig 1.10, middle) also follows the El-Sayed rule. The rate of intersystem crossing from S_1 $^1(n,\pi*)$ to T_2 $^3(\pi,\pi*)$ is higher than that from S_1 $^1(n,\pi*)$ to T_1 $^3(\pi,\pi*)$ although the energy gap between S_1 $^1(n,\pi*)$ and T_2 $^3(\pi,\pi*)$ is larger. The rate of intersystem crossing of acetone is much lower than that of benzophenone because of the large energy gap between the singlet and triplet.

To generate the triplet state efficiently, the rate of intersystem crossing must be higher among the competitive transitions such as fluorescence. Like benzophenone, the intersystem crossing is allowed by the El-Sayed rules and facilitated by a small energy difference. If one of these condition is not satisfied, the rate of intersystem crossing is lower or comparable with the competitive transitions, resulting in the yield of intersystem crossing becoming smaller. For this reason, only a small number of molecules including the carbonyl group and/or the non-bonding electron atom could be used as photosensitizers or triplet agents.

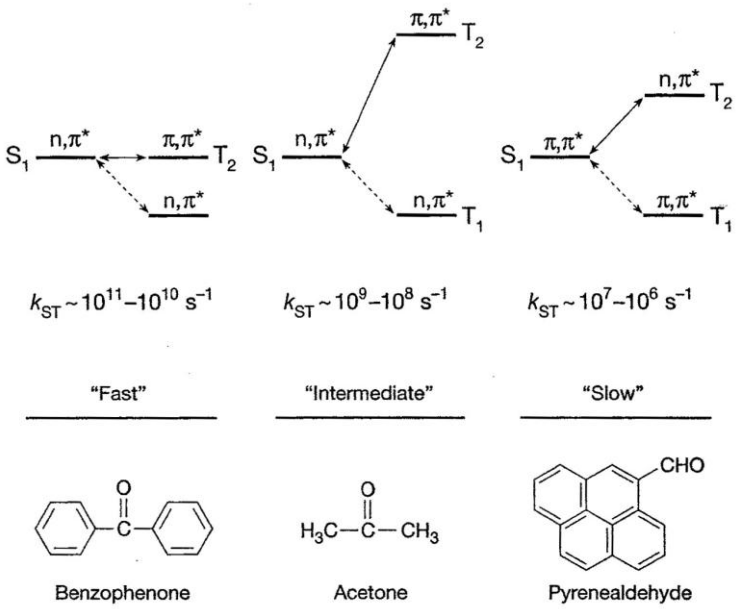

Figure 1.10. Schematic diagram of the energy levels with spin multiplicity. Solid arrow is allowed transition and dashed arrow is forbidden transition by El-Sayed rules. Image from N.J. Turro, *Modern Molecular Photochemistry* 1978.

1.3.2 Heavy-atom effect

As described earlier, spin-orbit coupling is the spin-orbit interaction due to the electromagnetic interactions between the electrons' spin and the magnetic field generated by the electrons' orbiting around the nucleus. With the increase in atomic number, the induced magnetic field becomes stronger. Therefore, the heavy-atom effect is simply a spin-orbit coupling enhancement produced by a heavy atom. It is known that spin-orbit coupling in an atom is proportional to the 4^{th} order of the atomic number. However, the heavy-atom effect on a molecule is a local event. Therefore, the heavy-atom effect on a molecule does not follow the 4^{th} order of the atomic number but the portion of the excited electron moving around the heavy atom. For example, as illustrated in Fig 1.11, the heavy bromine atom is connected to the π-conjugated benzene by sp3-sp2. Because the excited electron is usually located in the π-orbital, the travel of electron into the heavy atom through sp3-sp2 may not be easy. If a quinoidal structure is involved by resonance in the excited state, the electron can move into the heavy atom through sp2-sp2 and the electron could feel the magnetic field from heavy nucleus, thus enhancing spin-orbit coupling.

Halides are well-known heavy-atom units on organic molecules, and are key to enhance

spin-orbit coupling and enable phosphorescence. Spin-orbit coupling is generally enhanced as the size of halides increases.

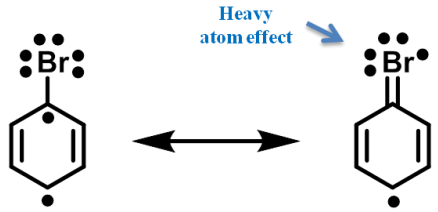

Figure 1.11. Possible resonance structure of 1-bromobenzene in the excited state. Aromatic structure (left) and quinoidal structure (right) in the excited state.

1.3.3 Metal-to-ligand charge transfer (MLCT)

Metal complexes based on the third-row transition metal ions such as Ir(III) and Pt(II) are well suited as the heavy metal center, which can induce significant spin-orbit coupling. Because of very strong spin-orbit coupling, even singlet-to-triplet absorption transition, a forbidden transition by the selection rule, can be detected[16]. A common misperception is that the heavy-atom effect can explain why metal complexes with heavy atoms like tris(2-phenylpyridine)iridium ($Ir(ppy)_3$) are phosphorescent while metal complexes with light atoms such as tris(8-hydroxyquinolinato)aluminum (Alq_3) are predominantly fluorescent[17]. For example, it was reported that some copper complexes[18] exhibit strong spin-orbit coupling compared to an Ir complex, which results in a very short triplet emission decay time of microseconds. Metal complexes can become phosphorescent regardless of the heavy-atom effect.

The strong spin-orbit coupling of metal complexes comes from zero-field splitting (ZFS). The d-orbital of metal-to-ligand interaction (or MO geometry) can induce electrostatic field, so called the crystal field. The crystal field can induce the spin degeneracy of two or more unpaired electrons in a metal complex in the absence of the magnetic field, zero-field splitting. Zero-field splitting can break selection rules like the Zeeman effects, which are the spin degeneracy under magnetic field. For more detailed information about zero-field splitting, see cited reference[19].

Metal-to-ligand charge transfer is the electron or charge transfer from MO with metal-like characters such as d-orbital to those of ligand-like characters having low-lying π^* orbital. Like the molecular local event of the heavy-atom effect, spin-orbit coupling is enhanced when excited electrons move through the metal-ligand coordination structure. Fig 1.12 describes the strength of spin-orbit coupling in a metal complex according to the ratio of the

MLCT character to the ligand-centered character (LC or intraligand charge transfer, ILCT). LC is a transition between HOMO and LUMO of a ligand molecule. It is noted that the lowest triplets of $[Ru(bpy3)]^{3+}$ are characterized as ligand-centered LC states with very small metal admixtures. In contrast, those of $[Ru(bpy3)]^{2+}$ represent the MLCT state. Therefore, $[Ru(bpy3)]^{2+}$ exhibits strong spin-orbit coupling and fast triplet emission decay of microseconds but the spin-orbit coupling of $[Ru(bpy3)]^{3+}$ is very weak in comparison.

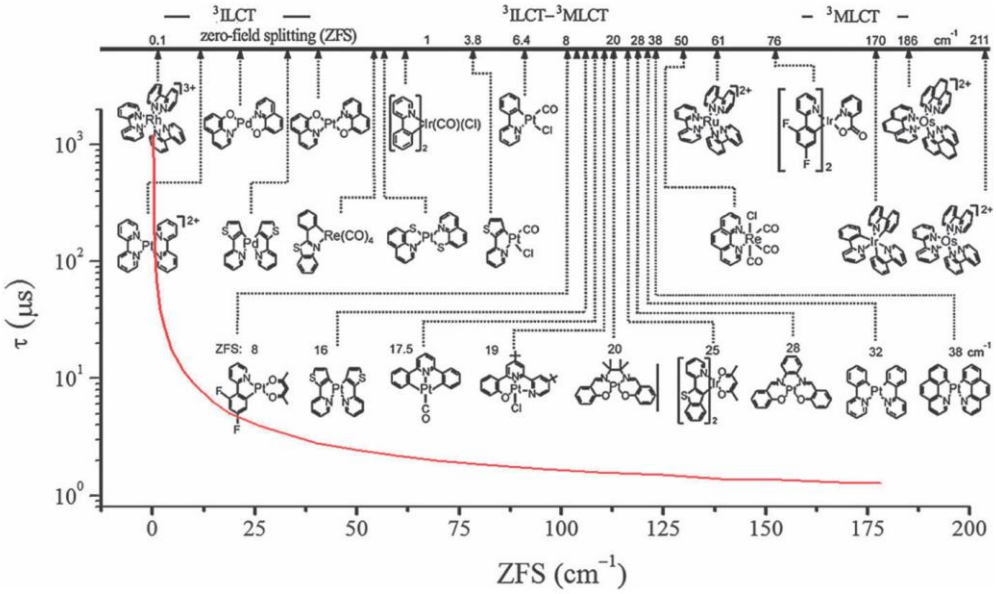

Figure 1.12. Phosphorescence lifetime (300 K) versus ZFS and ordering scheme showing metal complexes with increasing MLCT character in the emissive triplet state for metal complexes. Image from *Chem. Soc. Rev.* **2013**, 42, 6128-6185.

1.3.4 The energy difference between singlet and triplet state

A variety of nonradiative electronic processes pertain to the energy gap dependence of the nonradiative rate, so called the *energy gap law*. In the weak coupling limit, the changes in the equilibrium geometries between the initial and final states are relatively small. In this case, the energy gap law follows the exponential decay of the nonradiative rate for the energy gaps, i.e., the smaller the energy gap the faster the nonradiative rate[20]. The energy gap law was examined and applied for internal conversion and intersystem crossing. For example, the rate of internal conversion from S_n to S_{n-1}($\Delta E \sim 100$ cm^{-1}) is approximately 10^{-12} S^{-1} but the rate from S_1 to S_0 is approximately 10^{-9} S^{-1} ($\Delta E > 1000$ cm^{-1}). Therefore, intersystem crossing can be efficient with the low energy gap between singlet and triplet states even though spin-orbit coupling is small.

A notable example of triplet efficient harvesting is the thermally activated delayed

fluorescence (TADF). In low temperatures, the TADF molecule exhibits weak phosphorescence with the second order lifetime owing to weak spin-orbit coupling. Because of the low energy gap between singlet and triplet, intersystem crossing from singlet to triplet and reverse intersystem crossing via thermal energy are very efficient. The energy gap between singlet and triplet can be described by the equations below:

$$E_0 = 0 \text{ (by definition)}$$

$$E_S = E_0 + K + J$$

$$E_T = E_0 + K - J$$

$$\Delta E_{ST} = E_S - E_T = 2 \times J$$

K is the Columbic correction between two electrons and J is a quantum mechanical correction via electrons repulsion due to Pauli exclusion principle 6. The design principle of TADF molecules to minimize the energy gap is the separation of HOMO and LUMO in a molecule. The separation can reduce electrons repulsion due to the Pauli exclusion principle and then lead to a small energy gap. The key molecular designs for the TADF are i) donor and acceptor structure and ii) almost 90° (but not 90°) between donor and acceptor.

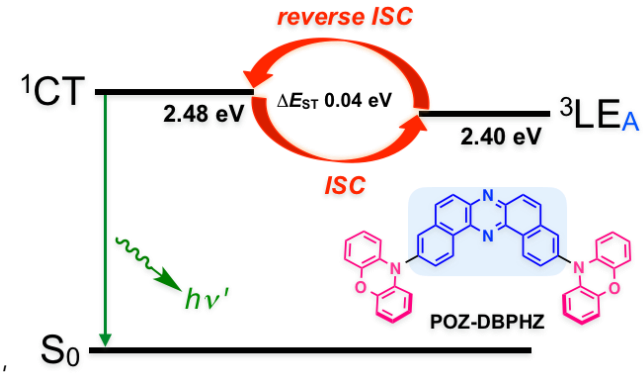

Figure 1.13 Jablonski diagram and molecular structure of TADF molecule. Image from *Angew. Chem. Int. Ed.* 2016, 55, 5739 –5744.

Recently, phosphorescent molecules having TADF-like molecular structures are reported.[21,22] The energy gap between singlet and triplet is not small enough for efficient reverse intersystem crossing but is not too large for feasible intersystem crossing. The research outcome indicated that triplet harvesting, which is the first step for phosphorescence after absorption, can be possible with weak spin-orbit coupling.

1.4 The theoretical explanation of non-radiative decay via vibration between T_1 to S_0

The theoretical work to develop understanding on the non-radiative processes was begun in the 1960s and 1970s but the nature of these processes is still not well understood. For phosphorescent materials, the processes are even more complicated because the spin factor must be considered. In addition, phosphorescence is sensitive to the environment such as solvent, polymer matrix, and temperature due to the slow kinetic dynamics compared to fluorescence. In this section, the theoretical explanation was summarized from references [1–6].

1.4.1 The "Loose Bolt" effect: The effect of molecular rigidity on non-radiative decay by intramolecular vibration

Molecular rigidity is one of the important structural requirements to achieve a high fluorescent quantum yield. The representative examples of the role of molecular rigidity that affect intramolecular vibrations are the flexible stilbene and their rigid cyclic derivatives (Fig 1.14). Trans- and cis-stilbene (**1,2**) are only weakly fluorescent in fluid solutions at room temperature. In contrast, the fluorescent quantum yield of their rigid stilbene derivatives (**3,4**) are unity at room temperature. The vibrational energy dissipation of the flexible stilbene is due to the free rotor effect around the C=C bonds. A schematic representation of the energy surface touching induced by twisting the C=C bond is shown in Fig 1.15. On the surface near r_c (surface-touching region), the same vibration causes vibronic mixing of the excited state and ground state orbitals, which causes a radiationless transition from the excited state to the ground state. The energy dissipation through the radiationless transition occurs on the touching surface, which is not a vertical transition like the Frank–Condon transition.

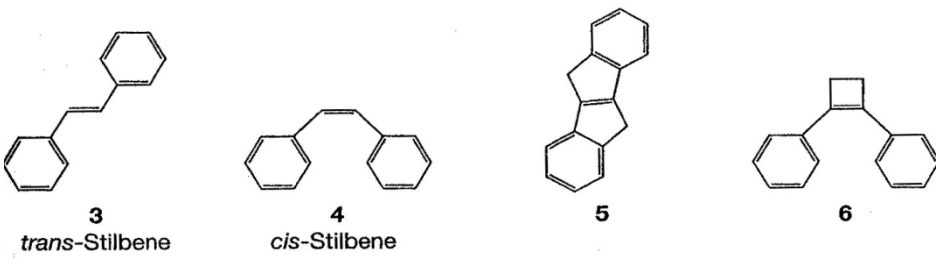

3 *trans*-Stilbene

4 *cis*-Stilbene

5

6

Temperature	*trans*-Stilbene **3**	*cis*-Stilbene **4**	**5**	**6**
25 °C	0.05	0.00	1.0	1.0
77 K	0.75	0.75	1.0	1.0

Figure 1.14 Phosphorescence quantum yields of a series of stilbene molecules at 25 ℃ and 77 K. Image from N.J. Turro, *Modern Molecular Photochemistry* 1978.

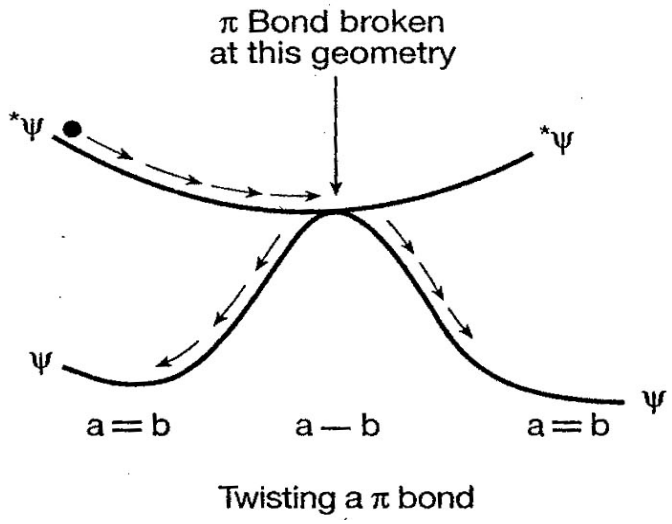

Figure 1.15 Schematic representation of energy surface from twisting a π bond. At a 90° twist, the double bond is broken and becomes a single bond. Image from N.J. Turro, *Modern Molecular Photochemistry* 1978.

When a structural rigidity is built into the molecular structure like in (**5**) and (**6**) the twisting motion is largely restricted regardless of temperature. These rigid stilbene derivatives show ~1.0 fluorescent quantum yield (Φ_f) at room temperature and 77 K. In contrast, both temperature and environmental aspects can contribute to the vibrational radiationless transition and consequent fluorescent quantum yield of flexible molecules. For example, trans-stilbene (**3**) exhibits 0.05 for Φ_f at room temperature in fluid solutions and 0.75 for Φ_f at 77 K in the solid solution. The Φ_f of (**3**) increases from the case in nonviscous organic solvents to the case in viscous glycerol (Φ_f ~ 0.15). A rigid environment can prevent the rotation of flexible molecules by putting an energy barrier to the potential energy surface of molecular rotation. The energy barrier impedes the non-radiative decay transition of the "Loose bolt" effect. In rigid environments, the mechanism of vibrational energy dissipation follows the Frank–Condon transition such as internal conversion.

1.4.2 Non-radiative decay by intramolecular vibration, intersystem crossing from T_1 to S_0[6,23]

When a molecular structure is rigid or its environment is rigid, there are no geometries along the reaction coordination in that the two energy surfaces of the ground state and one the excited state approach to the same energy like the "Loose bolt" model. In this case, a

radiationless transition between the two surfaces can be possible via the Frank–Condon transition. The transition would be relatively slow compared to the “Loose bolt” but can be compatible with other transitions such as radiative transition. Non-radiative decay by intramolecular vibration from S_1 to S_0 is of the same mechanism as internal conversion.

Non-radiative decay via intramolecular vibration from T_1 to S_0 is also one subset of internal conversion, vibrational relaxation. The difference is that the total spin is not conserved during the T_1 to S_0 relaxation process and thus the process is also called intersystem crossing. Like phosphorescence, non-radiative decay by intramolecular vibration from T_1 to S_0 is much slower than the non-radiative decay by intramolecular vibration from S_1 to S_0. The rate of non-radiative decay via intramolecular vibration is determined by the Femi golden rule, in which the rate of process is proportional to the density of final states, and by the energy gap law. The transition should be considered by the prohibition factors associated with the electronic (f_e), the nuclear (or vibrational change in position or motion, f_v), and the spin configuration change (f_s). fs is unity for the transition for which there are no spin changes such as singlet-to-singlet transition.

The rate of non-radiative decay by intramolecular vibration can be described as

$$k_{TS} \sim f_s f_e f_v p_e \sim f_s \exp(-\Delta E/\hbar\omega)\exp(-\Delta E/kT)\Upsilon$$

$$f_v \sim \Upsilon \exp(-\Delta E/\hbar\omega)$$

where, p_e is the number of vibrational energy levels per unit energy, or the density of states, and Υ is related to the density of state. ω is the largest vibration frequency, typically C-C and C-H vibrations. The prohibition factors associated with the spin configuration change, f_s, is related to spin-orbit coupling. f_s for non-radiative decay by intramolecular vibration during the phosphorescence is 10^{-9} to 10^{-3}. In general, f_s for aromatic compounds with weak spin-orbit coupling (e.g., Naphthalene) is approximately 10^{-9} and 10^{-3} for metal complexes involved with MLCT. Therefore, strong spin-orbit coupling can enhance phosphorescent as well as intersystem crossing including T_1 to S_0.

It is known that only some vibrational modes are important in radiationless transitions. The critical vibration modes are typically determined by a large vibrational frequency mode, e.g., the C-H asymmetrical stretch in aromatic molecules. This is because the higher the energy of a vibration, the fewer the number of quanta required to match an electronic gap with the vibrational energy. The high frequency vibration serves as the major intramolecular vibrations for the leakage of electronic into vibrational energy. Therefore, deuterium isotope or fluorine isotope can be expected to reduce vibrational energy dissipation from T_1(or S_1) to

S_0 because of their lower vibrational frequency. For example, at 77 K both benzene-h6 and benzene-d6 possess phosphorescent radiative decay (k_p) of 0.03 s but K_{TS} of benzene-d6 is much lower (Table 1). This result provides a strong evidence that the triplet loses electronic energy via C-H vibrations for rigid aromatic hydrocarbon.

Table 1.1 Representative values of triplet energy, phosphorescent radiative rates, intersystem crossing rates, and phosphorescent quantum yields. Table from N.J. Turro, *Modern Molecular Photochemistry* 1978

Molecule	E_T	k_P	k_{TS}	Φ_P
Benzene-h_6	85	~0.03	0.03	0.20
Benzene-d_6	85	~0.03	<0.001	~0.80
Naphthalene-h_8	60	~0.03	0.4	0.05
Naphthalene-d_8	60	~0.03	<0.01	~0.80
$(CH_3)_2C{=}O$	78	~50	1.8×10^3	0.043
$(CD_3)_2C{=}O$	78	~50	0.6×10^3	0.10

a. In organic solvents at 77 K. E_T in kcal mol^{-1}, k, in s^{-1}.

In addition to the Frank–Condon factor, f_s, the value of k_{TS} can be affected by spin-orbit coupling due to the heavy-atom effect or by the El-Sayed rule (Table 1.2). This is because the radiationless transition from T_1 to S_0 is the subset of the Frank–Condon transition which follows the selection rule or spin conservation law. Strong spin-orbit coupling is required to break down the selection rule. With heavier halide atoms attachment to naphthalene, both k_p and K_{TS} increases. The effect on Φ_p is not predictable because both k_p and K_{TS} are influenced by the heavy atom.

Table 1.2 Internal heavy-atom effects on transition between states. Table from N.J. Turro, *Modern Molecular Photochemistry* 1978

Molecule	k_F^0	k_{ST}	k_P^0	k_{TS}	Φ_F	Φ_P
Naphthalene	10^6	10^6	10^{-1}	10^{-1}	0.55	0.05
1-Fluoronaphthalene	10^6	10^6	10^{-1}	10^{-1}	0.84	0.06
1-Chloronaphthalene	10^6	10^8	10	10	0.06	0.54
1-Bromonaphthalene	10^6	10^9	50	50	0.002	0.55
1-Iodonaphthalene	10^6	10^{10}	500	100	0.000	0.70
Perylene	2×10^8	10^7			0.98	
3-Bromoperylene	2×10^8	10^7			0.98	

a. Data for rigid solution at 77 K. At room temperature, k_{TS} is often dominated by bimolecular deactivation of T_1 or by reactions of T_1. Rate constants are approximate in s^{-1}.

Recently, Hirata *et. al.* systematically studied the relationship between molecular structures and intramolecular vibration decay from T_1 to S_0 (Fig 1.16). Heavier substituents around the aromatic core reduce the vibration frequency or f_v but increases f_s because of the simultaneous heavy-atom effect. The experimental results indicate that deuterium substitution results in a small $k_{TS} \sim f_s f_v$ compared to the hydrated or fluorinated aromatics.

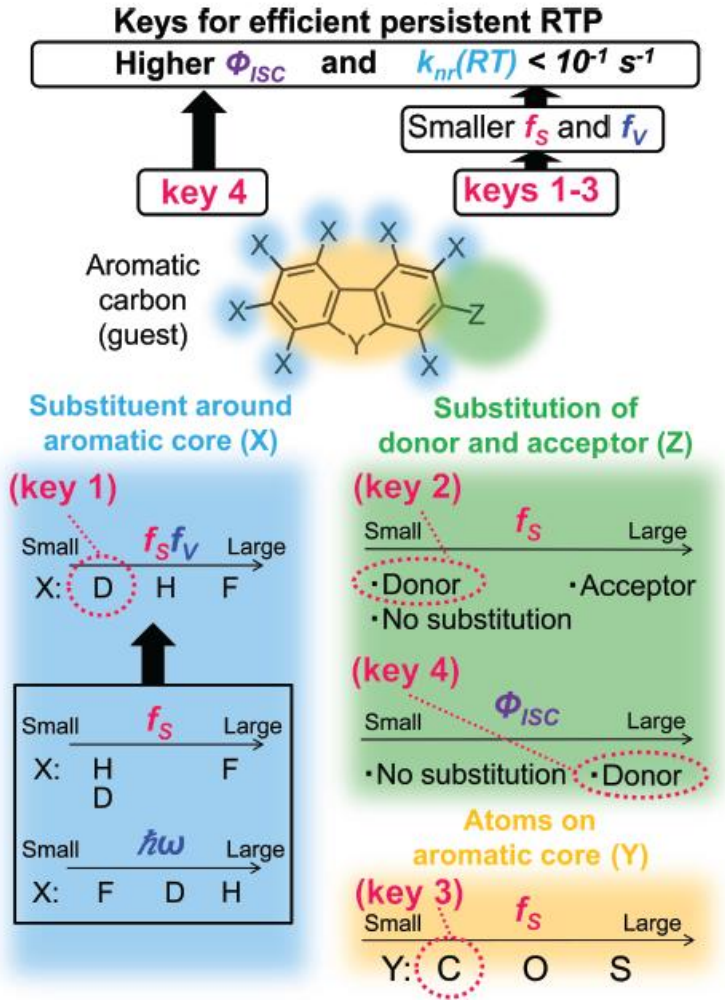

Figure 1.16 Molecular design of a guest compound for efficient and persistent RTP. Efficient and persistent RTP can be obtained by controlling key molecular elements (keys 1 to 4). Image from *Adv. Funct. Mater.* **2013**, *23*, 3386–3397.

In summary, the radiationless transition from T_1 (or S_1) to S_0 of flexible molecules in fluid solution is the "Loose bolt" effect, which is not the Frank–Condon transition and occurs on a potential touching surface. The radiationless transition via Frank–Condon transition is considered by the i) Fermi golden rule, ii) Frank-Condon prohibition factors, and iii) energy gap law. Vibration dissipation occurs on high frequency vibrations such as C-H stretching.

Because of the selection rule, the radiationless transition from T_1 (or S_1) to S_0 is influenced by spin-orbit coupling.

1.4.3 Non-radiative decay by intermolecular vibration from T_1 to S_0[1,23]

There are four possible triplet quenching mechanisms via intermolecular interactions: i) the Dexter energy transfer from phosphors to other molecules having a lower T_1 energy level, ii) collision-based quenching between phosphors and their environmental matrix, iii) aggregation quenching in high concentration, and iv) interactions between phosphors and oxygen, oxygen quenching. Low-concentration solutions or doped polymer films are generally used for phosphorescent systems to avoid aggregation quenching and to achieve bright phosphorescence. Further, the Dexter energy transfer from phosphors to host molecules does not occur because the host molecules are organic solvents or nonconjugated polymers that have a much higher T_1 energy level that the T_1 energy level of phosphors. Oxygen quenching was discussed in the section above. Therefore, the major non-radiative decay mechanism by intermolecular vibrations is typically the collision-based quenching between phosphors and their environmental matrix. In this section, collision-based quenching is described.

Phosphorescence from organic molecules is significantly influenced by temperature and their environments. For example, phosphorescence of benzophenone in a degassed PMMA was reported to decay exponentially at 250–320 K (β-relaxation temperature/α-relaxation temperature)[24]. The decay temperature of phosphorescence in a degassed polystyrene was 100 K, which is the r-relaxation of polystyrene[25]. These results suggest some deactivation processes associated with the side-chain relaxation of the polymer. In contrast, fluorescence from organic molecules and phosphorescence from organometalic compounds are generally insensitive to temperature and their environment. This is because phosphorescence from organic molecules is manifested through a very slow process, comparable to the thermal (or diffusional) motion of polymers. The triplet exciton of organic molecules cannot survive before collision between dyes and polymer matrices. The chance for host—guest collision is very high before the triplet exciton of organic molecules relaxes via the Frank-Condon transition such as radiation transition or intramolecular vibration relaxation.

The intramolecular vibration relaxation of a triplet is a non-radiative decay by intramolecular vibration from T_1 to S_0. The quenching mechanism is known as the Dexter-type triplet–triplet energy transfer between host and guest (phosphor) molecules. The

mechanism follows the Arrhenius equation ~A_0exp(-ΔG/kT). ΔG is the activation energy of the Dexter-type triplet–triplet energy transfer[26] and is proportional to the difference of the T_1 energy of the host and guest. A_0 is the collision frequency constant. Therefore, the use of host materials having a high T_1 energy or a guest material having a low T_1 energy can maximize the activation energy (ΔG), which minimizes the energy transfer process.

Hirata *et. al.* reported the method to reduce the non-radiative decay via intermolecular vibrations of phosphors. As shown in Fig 1.17, a decay in phosphorescent intensity or an increase in kq can be caused by the thermal motion of the host. For example, weak local motions such as β-relaxation of PMMA decreases phosphorescence quantum yield single exponentially. Below α`-relaxation, the phosphorescent intensity decays with double exponential because the two thermal motions of the polymer activate the collision between phosphors and the side-chain of the polymer. kq at room temperature is in the order of 10^2 or higher, which is much higher than $k_{TS.}$ To achieve bright room temperature phosphorescence from organic molecules, $K_{nr}(=k_q+k_{TS})<<K_p$ is required. Therefore, intermolecular vibration relaxation should be suppressed for bright room temperature phosphorescence. In general, metal-free phosphors without any halide or carbonyl exhibit k_p of one order magnitude, indicating that bright room temperature phosphorescence cannot be achieved due to k_p $(10^0)<<$ $k_q+k_{TS}(10^2)$ (PMMA samples in Fig 1.17). The use of rigid matrices such as β-estradiol (Fig 1.17) can suppress the thermal motion of the matrix at room temperature, which then enables the $K_{nr}(=k_q+k_{TS})<<K_p$ condition.

Nonradiative decay by intermolecular vibrations from T_1 to S_0 is the dominant process to quench triplet excitons from metal-free phosphors. To reduce the nonradiative decay and enhance phosphorescence, i) increase activation energy by using hosts having a high T_1 energy level of or guests having a low T_1 energy level, and ii) choose the host having its thermal-motion triggered at a much higher temperature than room temperature. Because k_q is much higher than k_{TS} at room temperature, the development of methods to suppress intermolecular vibration plays a key role in achieving bright room temperature phosphorescence.

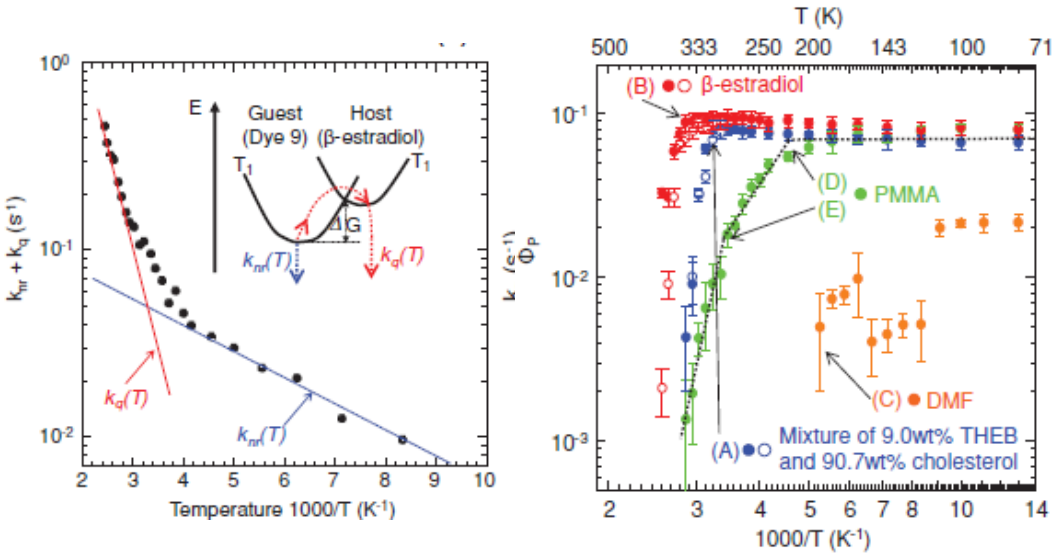

Figure 1.17. Left) Rate constant of the nonradiative deactivation pathway as a function of temperature for the material composed of phosphors and matrix. The inset shows that the nonradiative deactivation pathway is ascribed to the nonradiative deactivation and the Dexter-type T–T energy transfer from phosphor to matrix, based on the Arrhenius equation. Right) Quenching of the triplet exciton of phosphors was dispersed in various matrices. In this paper, the author uses the kinetic constant of intramolecular vibration relaxation as k_{nr} instead of k_{TS}. Image from *Adv. Funct. Mater.* **2013**, *23*, 3386–3397.

1.5 Recent progress in metal-free organic phosphors

Metal-free organic materials have been considered to be non-phosphorescent at room temperature because of their low intersystem crossing efficiency and prevailing nonradiative decay. Recent studies on metal-fee phosphors revealed possible strategies to suppress vibration relaxation and to achieve room temperature phosphorescence. Currently, metal-free phosphors have attracted much attention owing to their potential applications in display, solid state lighting, optical imaging, and sensors. The methods to enhance room temperature phosphorescence can be classified into two categories: i) host–guest system or doped polymer matrix, and ii) phosphorescent crystal. It is generally accepted that the polymer system for metal-free phosphors is much better for potential applications because crystal quality affecting phosphorescence properties is quite difficult to predictably control. Very recent studies[9] demonstrated that the crystal system can suppress vibrational dissipation significantly and consequently enable bright and persistent phosphorescence having a ultraslow phosphorescence lifetime as slow as in the order of seconds. The crystal system is more applicable for bio-imaging because of the insensitivity to oxygen and the afterglow.

In this section I have reviewed the two phosphorescent systems i) doped polymer matrix and ii) persistent phosphorescent crystal.

1.5.1 Polymer as host and metal-free phosphors as guest system for room temperature phosphorescence

In the field of photochemistry, the triplet lifetime and the decay phenomena of triplet excitons in polymer matrixes were extensively studied in the 1970s. The phosphorescence or triplet exciton decays at a certain transition temperature because the thermal motion of the polymer matrix causes collisions between phosphorescent molecules such as benzophenone and the polymer matrix. The transition temperature or the type of thermal motion (transition) causing the phosphorescence decay varies depending on the polymer. For example, the phosphorescence of benzophenone starts to decay at the β-relaxation temperature of PMMA but at the γ-relaxation temperature of PS. The transition temperature is generally lower than the room temperature. Therefore, phosphorescent decay occurs at a temperature lower than the room temperature, preventing bright room temperature phosphorescence in polymer systems.

Kwon *et. al.* devised an effective immobilization strategy by incorporating strong hydrogen bonding between a phosphor and polyvinyl alcohol (PVA)[27] in order to suppress the molecular motions (Fig 1.18). The new metal-free phosphor (G1) has a bromobenzaldehyde core and carboxylic acid side chains. The side chain periphery allows the formation of strong hydrogen bonding between G1 and the selected amorphous matrix, PVA, having hydrogen-bonding capability. The role of the intermolecular hydrogen-bonding was unquestionably supported by comparing the G1-PVA80 and the hydrogen-bonding-free analogous system, Br6A-PVA80. The Br6A-doped PVA80 film produced green phosphorescence at room temperature but the phosphorescence quantum yield was only 2.2%, which is much lower than 13% from G1-doped PVA80. PVA100 has 25% more hydrogen bonding sites than PVA80. By using PVA100 much strong green phosphorescence emission up to 24% was achieved from G1. To the best of my knowledge, this is the first development of the immobilization method to suppress vibrations between the phosphor and the matrix.

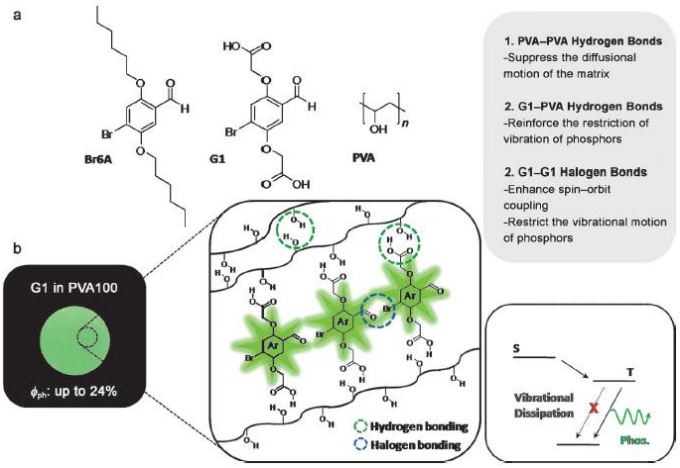

Figure 1.18 Schematic illustration of the immobilization method by incorporating hydrogen bonding between a phosphor and PVA a) Chemical structure of Br6A, G1, and PVA. B) Phosphorescence image of G1 embedded in PVA100 under UV light (365 nm). Schematic illustration of phosphorescence process in the G1-PVA composite. Image from *Angew. Chem. Int. Ed.* **2014**. 53. 11177.

In addition, Kwon *et. al.* incorporated covalent cross links between polymer matrixes and embedded phosphors to suppress their molecular motions.[28] The resulting cross-linked phosphor (DA1)-doped polymer system shows highly efficient room temperature phosphorescence with the phosphorescence quantum yield up to 28%, which is ca. 2—5 times higher than that of the control having no such covalent linkages, the phosphor (Br6A)-polymer blend system. Interestingly, the phosphorescence quantum yield of the cross-linked DA1-doped polymer is higher at room temperature although the phosphorescent decay temperature is much lower than that of the Br6A-doped polymer. Detailed spectroscopic studies on both polymer blend systems revealed that the restricting molecular motions by increasing rigidity of their local environment suppressed intermolecular vibration by decreasing the collision frequency and intramolecular vibrations (intersystem crossing from T_1 to S_0) by reducing vibronic mixing between zero-order electronic states of T_1 and S_0. Previous studies indicated that choosing a polymer having a high transition temperature for phosphorescent decay is an important design parameter to achieve bright room-temperature phosphorescence (e.g., the T_g difference of aPMMA and iPMMA). The active immobilization methods are more effective in achieving bright room-temperature phosphorescence than the passive choice of a polymer having a high transition temperatures.

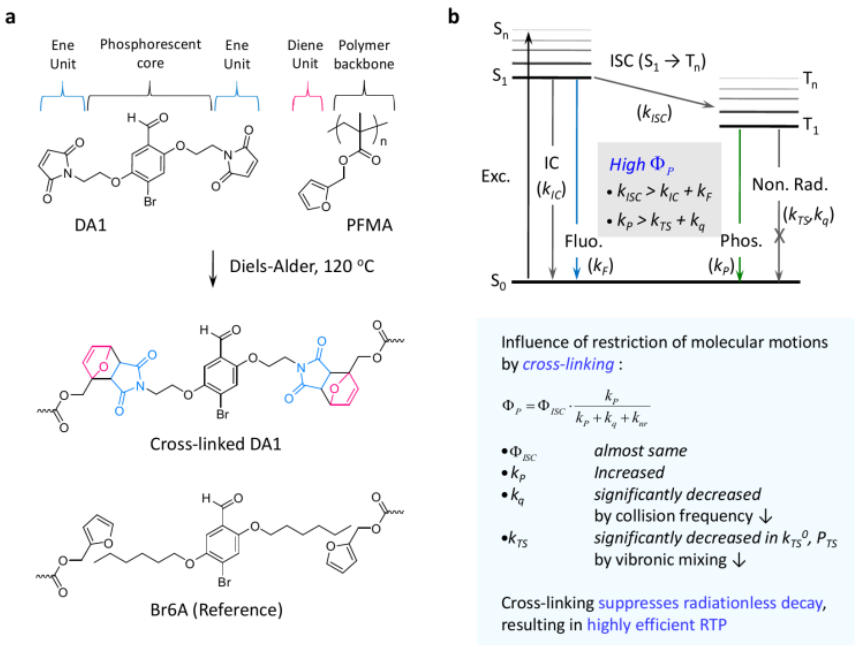

Figure 1.19 Description of immobilization methods for enhanced RTP from organic materials. Image from *Nat. Comm.* **2015**, 6, 1-9.

Persistent phosphorescence from a phosphors-doped choresterol-like matrix[23] (Fig 1.17) and from the phosphors inserted into MOFs[29] (Fig 1.20) have been reported. To suppress vibration efficiently at room temperature, they chose rigid host matrices having a high transition temperature than room temperature, and observed that the phosphorescence intensity at room temperature in the host matrices was the same as the intensity at 77 K.

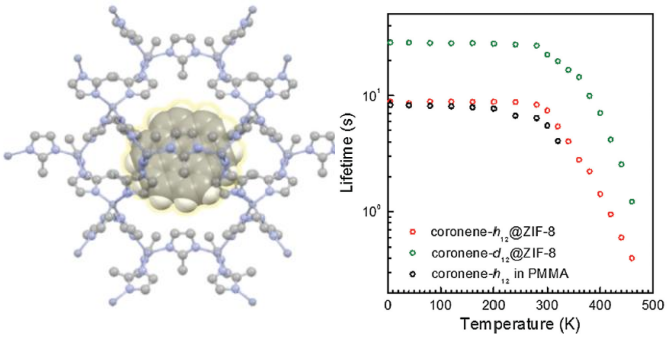

Figure 1.20 Illustration of phosphors@ZIF-8 MOFs. Left image is the structure of phosphors@ZIF-8 MOFs. Right image is temperature dependence of phosphorescence lifetime of coronene doped into PMMA, coronene@ZIF-8, and deuterated coronene@ZIF-8. Image from *Adv. Optical Mater.* **2016**, 7, 1015-1021.

1.5.2 Persistent phosphorescence in organic crystals

Persistent phosphorescence is delayed emission or afterglow, which can be observed by the naked eyes after the end of an excitation, UV, or visible light. The lifetime is in the order of seconds or even much longer. The persistent phosphorescence can be observed from both organic molecules and inorganic compounds. The persistent phosphorescence from inorganic crystals (or elements) is insensitive to oxygen because the Wannier–Mott exciton in an inorganic crystal cannot distinguish between a singlet and triplet. Further, oxygen quenching is not observed from the organic crystals owing to the low oxygen permeability of the crystals. It seems that both phosphors can be utilized as high-resolution bio-imaging without autofluorescence. However, metal-free phosphors would be a better choice considering various facts. First, inorganic compounds have generally a low extinction coefficient or low absorbance and hence the high intensity of phosphorescence signal in low doping concentrations is difficult to obtain. In addition, rare-earth metals or heavy metals such as europium are generally considered to be toxic to the human body.[30] A recently published paper showed[31] that in-vivo toxicity was not observed from their organic phosphorescent compounds. Therefore, persistent phosphorescence from organic crystals is very promising in the field of bio-imaging.

The lifetime of persistent phosphorescence is generally a few seconds, which means that the radiative decay constant (k_p) is in the order of 10^{-2} or 10^{-3} S^{-1}. The rate constant of intersystem crossing from T^1 to S^0 is also in the same order. The nonradiative decay by intermolecular vibration in polymers is generally over the order of 10^{23} S^{-1}, which is much higher than the k_p of persistent phosphorescence. Therefore, reducing the nonradiative decay constant to as much as 10^0 S^{-1} is the key to achieve bright persistent phosphorescence at room temperature. Organic crystals can suppress intermolecular vibration very efficiently because i) the free volume of crystals is smaller than that of polymers, and ii) secondary bonding interactions in crystals prevent vibration. However, the quantum yield of persistent phosphorescence is typically lower than 10%. The ultra-long phosphorescence lifetime indicates weak spin-orbit coupling, which causes inefficient triplet exciton generation due to inefficient intersystem crossing from singlet to triplet and a lower phosphorescence radiative decay constant than the nonradiative decay constant by intermolecular vibration.

Huang *et. al.* reported ultra-long phosphorescence in a variety of pure organic molecules at room temperature (Fig 1.21). They suggested a basic design principle for manipulating the long triplet exciton lifetime in organic materials. Through molecular H-aggregation, the

triplet exciton can be stabilized as long as ultra-long-lived luminescence is manifested (>1 s). The strong crystal packing suppresses molecular motions and reduces intermolecular vibration efficiently. The principle provides a convenient access to visible room temperature phosphorescence with a ultra-long lifetime. Owing to the weak spin-orbit coupling and the low yield of triplet generation, the phosphorescence quantum yield is approximately 1.25%, which is a very low quantum yield for bio-applications. However, their follow-up study[4] demonstrated that the phosphorescence intensity of the crystal associated with polymer nanoparticles could be comparable to that of inorganic luminescent nanoparticles, which suggested the possibility of persistent phosphorescence from organic crystals for real applications.

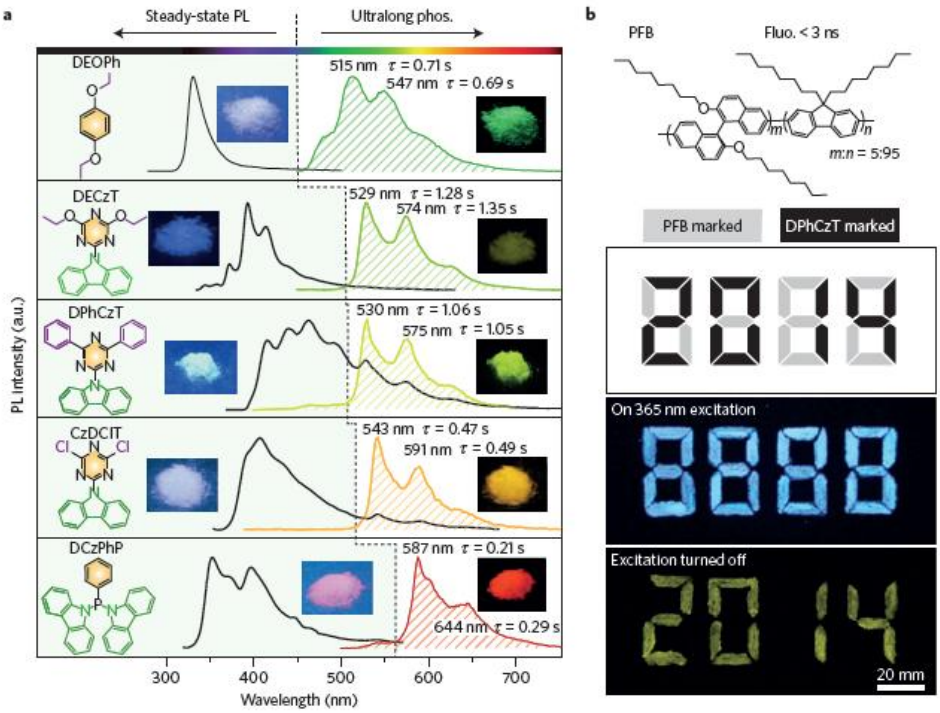

Figure 1.21 Examples of Persistent phosphorescence from organic crystal and their security application. a) Steady-state photoluminescence (left) and ultralong phosphorescence (right) spectra of a series of molecules. Insets shows the corresponding photographs taken before (left) and after (right) the excitation source is turned on. b) Demonstration of lifetime encoding for security applications using DPhCzY in combination with a PFB dye molecule. Image from *Nat. Mater*. **2015**, 14, 685-690.

Liu *et. al.* reported persistent room temperature organic crystals with bright red phosphorescence.[31] C-C-Br_4 (Fig 1.22) exhibits a quantum yield of 11%. Their design principle is to introduce a free-chain linker between carbazole and benzophenone, which significantly enhances the intermolecular interactions between them in the crystal. Those results showed that strong intermolecular electronic coupling and intermolecular heavy-atom effect led to bright phosphorescence. They prepared phosphorescent nanocrystals in aqueous media with excellent biocompatibility. The series of study on persistent phosphorescence pave the way for further exploration of real applications in the biological world. However, the excitation wavelength of the molecules is shorter than 400 nm which can damage the skin or cell.

1.6 Conclusion

Phosphorescence is a type of photoluminescence related to fluorescence. Unlike fluorescence, phosphorescence from organic molecules has slow emission, oxygen sensitivity, and vibration sensitivity. The unique features of phosphorescence are associated with the triplet state, which is related to the forbidden transition in quantum mechanics or the spin conservation law. These features provide several advantages for potential applications. Their longer lifetime provides a high resolution imaging capability with a low signal-to-noise ratio owing to the exclusion of autofluorescence and excitation light. In addition, oxygen sensitivity and thermal sensitivity can be utilized in sensing applications by utilizing phosphorescence intensity and/or lifetime as a sensory signal. From these advantages, phosphorescence from organic materials is gaining interests from new and existing research fields. However, bright room temperature phosphorescent organic materials are still challenging to devise because the design principle of such organic phosphors is not well established.

To achieve bright room temperature phosphorescence from metal-free phosphors the following conditions must be satisfied: i) strong spin-orbit coupling to overcome the forbidden transitions such as intersystem crossing from singlet to triplet and phosphorescent radiative decay, and ii) efficient suppression of vibrational motions between the host matrix and phosphors or of the molecules themselves. Aromatic aldehyde and the halide group can enhance spin-orbit coupling and thus are key design parameters for metal-free phosphors. Rigid polymer matrix and crystal packing can suppress vibrational motions and accordingly enhance room temperature phosphorescence. Even though for some applications the oxygen

quenching phenomenon can be a drawback, the same oxygen quenching property can be used for oxygen sensing applications. Therefore, depending on the application, the type of phosphorescent system must be chosen logically. Phosphorescent crystals are better for imaging and phosphorescence in doped polymer films is much more feasible for body activity monitoring based on oxygen concentration.

Recent progress in metal-free phosphors demonstrates the possibility of their real applications. However, bright room temperature phosphorescence without metal is still limited within specific systems. To develop new generations of organic phosphors, generally applicable molecular design principles of phosphorescence must be established.

1.7 References

1. Hirata, S., "Recent Advances in Materials with Room Temperature Phosphorescence: Photophysics for Triplet Exciton Stabilization." *Adv. Optical Mater.* **2017**, 1700116.
2. Yu, Y., Kwon, M.S., Jung, J., Zeng, Y., Kim, M., Chung, K., Gierschner, J., Youk, J.H., Borisov, S.M. and Kim, J., "Room Temperature Phosphorescence based Dissolved Oxygen Detection by Core-shell Polymer Nanoparticles having Metal-free Organic Phosphor." *Angew. Chem. Int. Ed.* **2017**, 129, 16425-16429.
3. Zhang, G., Palmer, G.M., Dewhirst, M.W. and Fraser, C.L., "A Dual-Emissive-Materials Design Concept Enables Tumour Hypoxia Imaging." *Nat. Mater.* **2009**, 8, 747-751.
4. Zhen, X., Tao, Y., An, Z., Chen, P., Xu, C., Chen, R., Huang, W. and Pu, K., "Ultralong Phosphorescence of Water-soluble Organic Nanoparticles for in vivo Afterglow Imaging." *Adv. Mater.* **2017**, 29, 1606665.
5. Levine, I.N., *Quantum Chemistry* (Prentice-Hall, Upper Saddle River, NJ ,1991)
6. Turro, N.J. *Modern Molecular Photochemistry* (University Science Books, Sausalito CA, 1991)
7. Schweitzer, C. and Schmidt, R., "Physical Mechanisms of Generation and Deactivation of Singlet Oxygen", *Chem. Rev.* **2003**, *103*, 1685-1757.
8. Tian, W., Deng, L., Jin, S., Yang, H., Cui, R., Zhang, Q., Shi, W., Zhang, C., Yuan, X. and Sha, G., "Singlet Oxygen Phosphorescence Lifetime Imaging Based on a Fluorescence Lifetime Imaging Microscope." *J. Phys. Chem. A* **2015**, 14 3393-3399.
9. An, Zhongfu, Chao Zheng, Ye Tao, Runfeng Chen, Huifang Shi, Ting Chen, Zhixiang Wang et al. "Stabilizing Triplet Excited States for Ultralong Organic Phosphorescence." , *Nat. Mater*. **2015**, 14, 685-690.
10. Zhong, W., Urayama, P. and Mycek, M.A., "Imaging Fluorescence Lifetime Modulationof a Ruthenium-based Dye in Living Cells: The Potential for Xxygen Sensing." *J. Phys. D- Appl. Phys.* **2003**, *36*, 1689.
11. Mathew, A.S., DeRosa, C.A., Demas, J.N. and Fraser, C.L., "Difluoroboron β-diketonate Materials with Long-lived Phosphorescence Enable Lifetime based Oxygen Imaging with a Portable Cost Effective Camera." *Anal. Methods* **2016**, 8, 3109-3114.
12. Lo, K.K.W., Lee, P.K. and Lau, J.S.Y., "Synthesis, Characterization, and Properties of Luminescent Organoiridium (III) Polypyridine Complexes Appended with an Alkyl Chain and their Interactions with Lipid Bilayers, Surfactants, and Living Cells."

Organometallics **2008**, *27*, 2998.

13. Lee, D., Ma, X., Jung, J., Jeong, E.J., Hashemi, H., Bregman, A., Kieffer, J. and Kim, J., "The Effects of Extended Conjugation Length of Purely Organic Phosphors on their Phosphorescence Emission Properties." *Phys. Chem. Chem. Phys.* **2015**, 29 19096-19103.
14. Rogers, J.E., Cooper, T.M., Fleitz, P.A., Glass, D.J. and McLean, D.G., "Photophysical Characterization of a Series of Platinum (II)-Containing Phenyl−Ethynyl Oligomers" *J. Phys. Chem. A* **2002**, 106, 10108-10115.
15. Marian, C.M., "Spin–orbit Coupling and Intersystem Crossing in Molecules", *WIREs Comput Mol Sci* **2012**, 2, 187–203.
16 Wang, H., Liao, Q., Fu, H., Zeng, Y., Jiang, Z., Ma, J. and Yao, J., "Ir (ppy) 3 Phosphorescent Microrods and Nanowires: Promising Micro-phosphors." *J.Mater.Chem.* **2009**, 19, 89-96.
17. Tang, C.W. and VanSlyke, S.A., "Organic Electroluminescent Diodes." *Appl. Phys. lett.* **1987**, *51*, 913-915
18. Leitl, M.J., Krylova, V.A., Djurovich, P.I., Thompson, M.E. and Yersin, H., "Phosphorescence versus Thermally Activated Delayed Fluorescence.", J. *Am. Chem. Soc.* **2014**, *136*, 16032–16038
19. Krzystek, J., Telser, J., Pardi, L.A., Goldberg, D.P., Hoffman, B.M. and Brunel, L.C., "High-frequency and -field Electron Paramagnetic Resonance of High-spin Manganese (III) in Porphyrinic Complexes." *Inorg. Chem.* **1999**, 3*8*, 6121-6129.
20. Bixon, M., Jortner, J., Cortes, J., Heitele, H. and Michel-Beyerle, M.E., "Energy Gap Law for Nonradiative and Radiative Charge Transfer in Isolated and in Solvated Super molecules", *J. Phys. Chem.* **1994**, 98, 1289-7299.
21. Mao, Z., Yang, Z., Mu, Y., Zhang, Y., Wang, Y.F., Chi, Z., Lo, C.C., Liu, S., Lien, A. and Xu, J., "Linearly Tunable Emission Colors Obtained from a Fluorescent–Phosphorescent Dual-Emission Compound by Mechanical Stimuli", *Angew. Chem. Int. Ed.* **2015**, 54, 6270 –6273
22. Gong, Y., Chen, G., Peng, Q., Yuan, W.Z., Xie, Y., Li, S., Zhang, Y. and Tang, B.Z., "Achieving Persistent Room Temperature Phosphorescence and Remarkable Mechanochromism from Pure Organic Luminogens", *Adv. Mater.* **2015**, 27, 6195–6201
23. Hirata, S., Totani, K., Zhang, J., Yamashita, T., Kaji, H., Marder, S.R., Watanabe, T. and Adachi, C., "Efficient Persistent Room Temperature Phosphorescence in Organic

Amorphous Materials under Ambient Conditions.", *Adv. Funct. Mater.* **2013**, 23 3386-3397.

24. Horie, K. and Mita, I.,"Photochemistry in Polymer Solids. Decay of Benzophenone Phosphorescence in Poly (methyl methacrylate).", *Chem. Physics Letters* **1982**, 93, 61-65
25. Horie, K., Tsukamoto, M., Morishita, K. and Mita, I., "Photochemistry in Polymer Solids V. Decay of Benzophenone Phosphorescence in Polystyrene and in Polycarbonate." *Polymer journal* **1985**, 17 517-524
26. Adachi, C., Baldo, M.A., Thompson, M.E. and Forrest, S.R., "Nearly 100% Internal Phosphorescence Efficiency in an Organic Light-Emitting Device.", *Appl. Phys. Lett.* **2001**, 79, 2082.
27. Kwon, M.S., Lee, D., Seo, S., Jung, J. and Kim, J., "Tailoring Intermolecular Interactions for Efficient Room-temperature Phosphorescence from Purely Organic Materials in Amorphous Polymer Matrices." *Angew. Chem. Int. Ed*. **2014**, 53, 11177-11181.
28. Kwon, M.S., Yu, Y., Coburn, C., Phillips, A.W., Chung, K., Shanker, A., Jung, J., Kim, G., Pipe, K., Forrest, S.R. Youk, J.H., Gierschner, J., and Kim, J., "Suppressing Molecular Motions for Enhanced Room-temperature Phosphorescence of Metal-free Organic Materials." *Nat. Commun.* **2015**, 6, 1-9.
29 Mieno, H., Kabe, R., Notsuka, N., Allendorf, M.D. and Adachi, C., "Long-Lived Room-Temperature Phosphorescence of Coronene in Zeolitic Imidazolate Framework ZIF-8." *Adv. Opt. Mater.* **2016**, 4, 1015-1021.
30. Andrews, R.E., Shah, K.M., Wilkinson, J.M. and Gartland, A., "Effects of Cobalt and Chromium Ions at Clinically Equivalent Concentrations after Metal-on-metal Hip Replacement on Human Osteoblasts and Osteoclasts: Implications for Skeletal Health." *Bone* **2011**, *49*, 717.
31. Fateminia, S.M., Mao, Z., Xu, S., Yang, Z., Chi, Z. and Liu, B., "Organic Nanocrystals with Bright Red Persistent Room-Temperature Phosphorescence for Biological Applications." *Angew. Chem. Int. Ed*. 2**017**, 56, 12160-12164.

Chapter 2

Molecular design for fluorene-based metal-free phosphors in amorphous polymer matrices

In order to achieve bright room-temperature phosphorescence, collision-based vibration quenching, so-called Dexter-type triplet–triplet energy transfer, should be suppressed, and spin–orbit coupling should be enhanced. Many recent papers have reported polymer matrixes for suppressing intermolecular vibration quenching and bright metal-free phosphors by adapting basic molecular design principles such as using aldehyde and halide group. This chapter illustrated the general design principle of metal-free phosphors in amorphous polymer matrices. We studied the correlation between the molecular structure of phosphors and three transition processes: i) intramolecular vibrational nonradiative decay, iii) phosphorescence radiative decay, and iii) intermolecular vibrational nonradiative decay. The results of our study clarified the design of the phosphorescent molecule and suggested a method for achieving bright room-temperature phosphorescence without phosphorescent decay below room temperature

2.1 Introduction

Room-temperature phosphorescence (RTP) has attracted a great deal of attention in the fields of optoelectonric devices[1], high contrast bio-imaging[2], photodynamic therapy[3], photocatalytic reactions[4], and oxygen indicators[5]. Although RTP was generally considered the sole function of organometallic complexes, RTP from metal-free organic phosphors has attracted considerable interests for optical imaging in biology and medicine because of the unclear toxicities of the standard metal complexes[6]. However, the development of metal-free organic phosphor systems is challenging due to limited design principles for i) efficient intersystem crossing (ISC) through spin–orbit coupling (SOC) (k_{ISC}, k_p) and ii) nonradiative quenching deactivation by intramolecular vibration (k_{TS}) and collisional interactions with the surrounding matrix[7] (k_q).

A common molecular design for metal-free phosphors with enhanced SOC commonly involves carbonyl groups or/and heavy halogens attached to the aromatic unit. Aromatic carbonyls are attractive moieties for designing metal-free organic phosphors due to the generation of $n\pi^*$ states. For example, benzophenone shows approximately 100% ISC (i.e., Φ_{ISC}=1) because ISC from S_1 $^1(n,\pi*)$ to T_2 $^3(\pi,\pi*)$ is allowed by El Sayed's rule, and the S_1–T_2 energy gap is very small[8]. Therefore, triplet states are generally not generated in organic molecules if both (i) small S–T gap and (ii) orthogonality criterion (i.e., El-Sayed's rule allowed $^1(\pi\pi^*)\leftrightarrow{}^3(n\pi^*)$) are not simultaneously met. Molecular design rules to tune the energy level of singlet and triplet n,π* states are limited, however. Thus, only a few examples of bright RTP aromatic carbonyl compounds without halides have been reported[9].

The heavy atom effect is a well-known design strategy for SOC enhancement that promotes spin-forbidden processes such as singlet-to-triplet ISC and phosphorescence radiative decay from the triplet to the singlet ground state. . However, not all metal-free organic compounds having halides for the heavy atom effect are phosphorescent. For instance, diiodo-boron-dipyrromethene (diiodo-BODIPY) exhibits 70% singlet oxygen generation, which is a triplet-quenching process by triplet oxygen[10], indicating that triplet generation is highly efficient, but the photosensitizer does not show efficient phosphorescence, even at 77 K[11]. In addition, reported attempts to enhance phosphorescent properties by multi-halide substitution on dyes such as anthraquinone, fluorene, benzophenone, and BODIPY were not successful[12]. Apparently, halide substitution on organic molecules alone is not a pathway for

developing RTP materials.

Considering that the radiative decay rate of metal-free organics is very slow in a mostly millisecond regime, controlling the competitive non-radiative deactivation plays a key role in enhancing RTP of metal-free phosphors. Rigid environmental conditions restrict the thermal motion of the host matrix and decrease the collision frequency between the host and phosphors. This phenomenon significantly reduces the Dexter-type triplet energy transfer process from the metal-free phosphors to the host (k_q), which is the main radiationless relaxation of triplet excitions at room temperature (r.t.)[7]. A common method to enhance RTP in metal-free phosphors is to fabricate phosphorescent single crystal, co-crystal, and doped-crystal[13]. Here, polymorphism, crystal quality, and secondary interactions in the crystal are important parameters affecting largely the nonradiative deactivation[14]. A more technically viable method to enhance RTP in metal-free phosphors is to embed phosphors in rigid amorphous matrices such as poly(methyl methacrylate) (PMMA), poly(vinyl alcohol), micelles, and steroid analogues[15]. However, minor weak local motions of the polymer such as β-relaxation significantly influence the phosphorescent properties of metal-free phosphors. Effectively restricting these weak local motions in amorphous matrices can greatly reduce the rate of nonradiative decay, allowing even afterglow or persistent phosphorescence. Although the relationship between k_q and polymer relaxation or crystal structure has been investigated[7,16], the effect of the molecular structure on k_q in a polymer matrix is not fully understood, thus limiting the development of bright RTP applications in polymer matrices.

Herein, we present a general molecular design approach to developing bright RTP from metal-free organic phosphors in an amorphous polymer matrix. To that end, we chose 2,7-disubstituted 9,9-dihexyl-fluorene derivatives (Fig. 2.1) based on a rational design concept encompassing the following points: (1) BrFL1, a fluorene compound (Fig. 2.1), was previously reported to exhibit strong RTP with a quantum yield (QY) of Φ_P=5.9%, even in a chloroform solution under inert conditions. (2) The rigid molecular structure of fluorene may prevent it from changing molecular geometry during excitation and deactivation, which may not only suppress the nonradiative decay process but also allow to investigate the electronic distribution during the excition and relaxation process. (3) The RTP-active BrFL1 is a good reference compound for studying the influence of the 2,7 substitutions (including different halogens) vs. (known) non-RTP compounds in the same family (HFL1, BrFLBr, and IFL1). Although molecules showing persistent or ultralong phosphorescence have recently attracted

the attention of researchers, their QY when embedded in a polymer film does not exceed 10% without carbonyl, halide, or deuterium in the molecule.[7,17] (4) Collision-based quenching by Dexter-type triplet energy transfer (k_q) of BrFL1 is activated upon the γ-relaxation, not β-relaxation, of PMMA, which is a well-known thermal motion of PMMA that activates collision quenching. To the best of our knowledge, this phenomenon has not been studied until now. Overall, this study suggests generally applicable molecular design parameters for achieving bright RTP from metal-free phosphors in polymer systems.

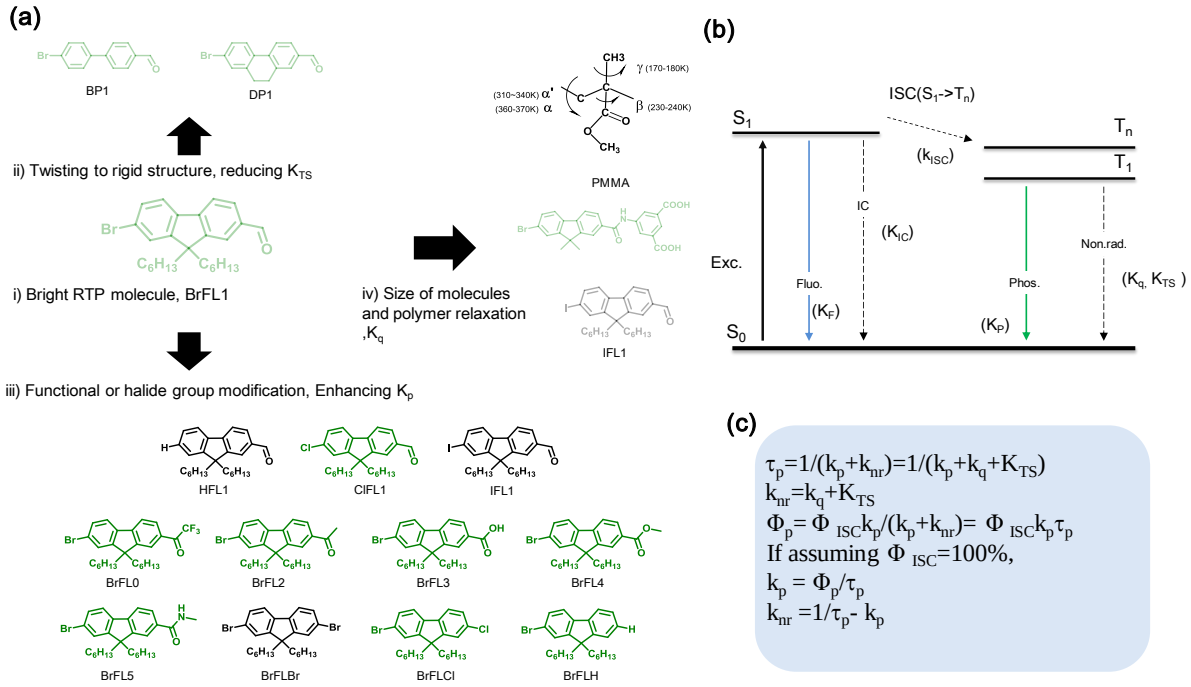

Figure 2.1 Chemical structures of designed phosphors and PMMA. (a) Chemical structure of BrFL1 and the newly designed phosphors. (b) A general Jablonski diagram for absorption, fluorescence, and phosphorescence. (c) Equations describing the phosphorescent lifetime, kinetics rate, and QY.

2.2 Experiments

2.2.1 General Methods

All chemicals used were purchased from Sigma Aldrich and Fisher Scientific and used without further purification. BP1 (4'-bromo-[1,1'-biphenyl]-4-carbaldehyde) was purchased from Sigma Aldrich. DP1 (UV absorption measurements were collected using a Varian Cary 50 Bio spectrometer with a solution sample held in a quartz cuvette. Photoluminescence (PL) emission, excitation, and QY data were collected using a Photon Technologies International

(PTI) QuantaMaster system equipped with an integrating sphere. Quantum lifetime data were collected using a PTI LaserStrobe. Quantum lifetimes were calculated using Origin 8.0 Pro. Low-temperature measurements were conducted on a Janis VPF-1000 cryostat.

2.2.2 Synthesis of molecules.

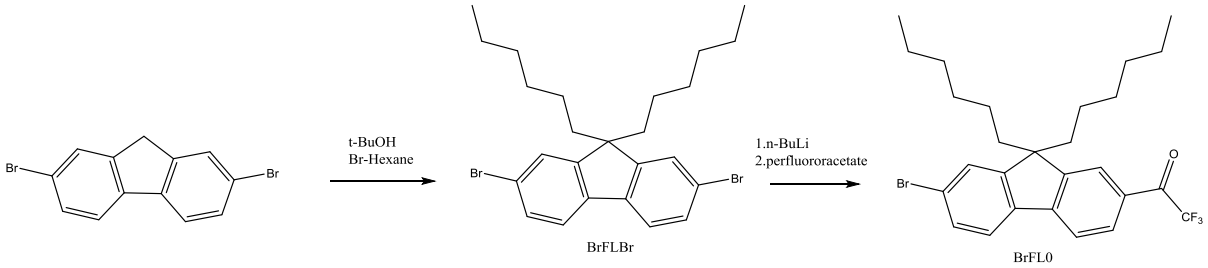

Scheme 2.1 Synthetic route to BrFLBr and BrFL0.

Synthesis of 2,7-dibromo-9,9-dihexyl-9H-fluorene (BrFLBr). First, t-BuOH powder (3 equiv.) was added to the solution of **2,7-dibromo-9H-fluorene** (1 equiv.) in anhydrous tetrahydrofuran (THF) at 0℃. The resulting solution was stirred for 30 min, and 1-bromohexane (3 equiv.) was then added. The reaction was stirred at r.t. overnight. The reaction was quenched by adding water and extracted with hexanes. The organic layer was collected and dried over $MgSO_4$ before being filtered and evaporated under reduced pressure. Purification was performed by column chromatography with hexane. White powder was collected in a yield of 63%. ^{1}H-NMR (400 MHz, $CDCl_3$): δ 7.52 (d, 2H), 7.46 (m, 2H), 2.0 (m, 4H), 1.12-0.98 (m, 12H), 0.8 (t, 6H), 0.6 (m, 4H).

Synthesis of 1-(7-bromo-9,9-dihexyl-9H-fluoren-2-yl)-2,2,2-trifluoroethan-1-one (BrFL0). BrFLBr (1 equiv.) was placed into a flame-dried reaction flask and vacuum purged with argon. Anhydrous THF was then added, and the reaction flask was cooled to -78℃. Next, n-BuLi (2.5 M, 1 equiv.) was added dropwise, and the reaction was stirred for 1 hour, followed by the addition of ethyl perfluororacetate (1 equiv.). After stirring for 1 hour, the resulting mixture was allowed to warm to r.t. overnight. The reaction was carefully quenched with NH_4Cl and extracted with ethyl acetate. The extracted organic layer was dried over $MgSO_4$, filtered, and evaporated under reduced pressure. Purification was performed by silica column chromatography with dichloromethane/hexane. White powder was collected in a yield of 80%. ^{1}H-NMR (400 MHz, $CDCl_3$): δ 7.77 (s, 1H), 7.69 (s, 2H), 7.58 (d, 1H), 7.47 (d, 2H), 1.96 (m, 4H), 1.14-0.97 (m, 12H), 0.76 (t, 6H), 0.55 (m, 4H).

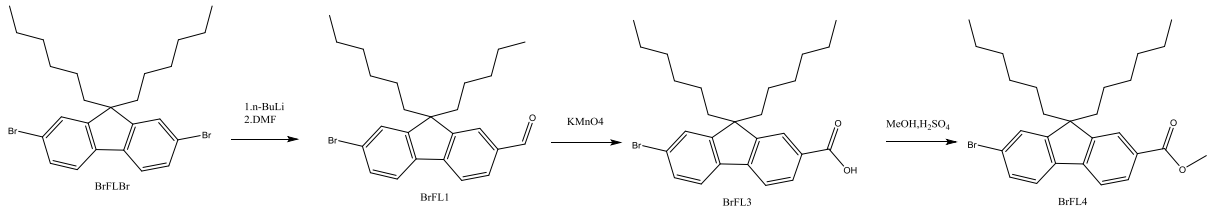

Scheme 2.2 Synthetic route to BrFL1, BrFL3, and BrFL4.

Synthesis of 7-bromo-9,9-dihexyl-9H-fluorene-2-carbaldehyde (BrFL1). BrFLBr (1 equiv.) was placed into a flame-dried reaction flask and vacuum purged with argon. Anhydrous THF was added, and the reaction flask was cooled to -78℃. Next, n-BuLi (2.5 M, 1.1 equiv.) was added dropwise and the reaction was stirred for 1 hour, followed by the addition of dimethylformamide (DMF, 3 equiv.). After stirring for 1 hour, the resulting mixture was allowed to warm to r.t. overnight. The reaction was quenched by adding ethyl acetate and water, and the resulting solution was extracted with ethyl acetate. The extracted organic layer was dried over $MgSO_4$, filtered, and evaporated under reduced pressure. Purification was performed by silica column chromatography with dichloromethane/hexane. White powder was collected in a yield of 49%. ^{1}H-NMR (400 MHz, $CDCl_3$): δ 10.0 (s, 1H), 7.85-7.83 (m, 2H), 7.79-7.77 (d, 1H), 7.62-.7.60 (d, 1H), 7.49-7.48 (m, 2H), 1.96 (m, 4H), 1.12-0.973 (m, 12H), 0.74 (t, 6H), 0.56 (m, 4H).

Synthesis of 7-bromo-9,9-dihexyl-9H-fluorene-2-carboxylic acid (BrFL3). The solution of BrFL1 (1 equiv.) in acetone and the solution of KMnO4 in water were mixed at a 1:1 ratio in a flask. After stirring overnight, KMnO4 was quenched by adding HCl, and the precipitate was removed by filtration. The resulting solution was extracted with ethyl acetate. The extracted organic layer was dried over $MgSO_4$, filtered, and evaporated under reduced pressure. Purification was performed by silica short column chromatography with chloroform. Powder was collected in a yield of 80%. ^{1}H-NMR (400 MHz, $CDCl_3$): δ 8.16 (d, 1H), 8.08 (s, 1H), 7.75 (d, 1H), 7.63 (d, 1H), 7.51 (s, 1H), 7.50 (d, 1H), 1.99 (m, 4H), 1.14-0.99 (m, 12H), 0.76 (t, 6H), 0.58 (m, 4H).

Synthesis of methyl 7-bromo-9,9-dihexyl-9H-fluorene-2-carboxylate (BrFL4). BrFL3 (1 equiv.) was dissolved in an excess amount of MeOH. HCl (0.1 equiv.) was added to the reaction solution, and the solution was refluxed overnight. After cooling, the resulting solution was extracted with ethyl acetate. The extracted organic layer was dried over $MgSO_4$, filtered, and evaporated under reduced pressure. Purification was performed by silica short column chromatography with chloroform. Powder was collected in a yield of 90%. ^{1}H-NMR (400 MHz, $CDCl_3$): δ 8.03 (d, 1H), 7.98 (s, 1H), 7.69 (d, 1H), 7.59 (d, 1H), 7.48 (s, 1H), 7.47 (d, 1H), 3.94 (s, 3H), 1.96 (m, 4H), 1.13-0.97 (m, 12H), 0.75 (t, 6H), 0.58 (m, 4H).

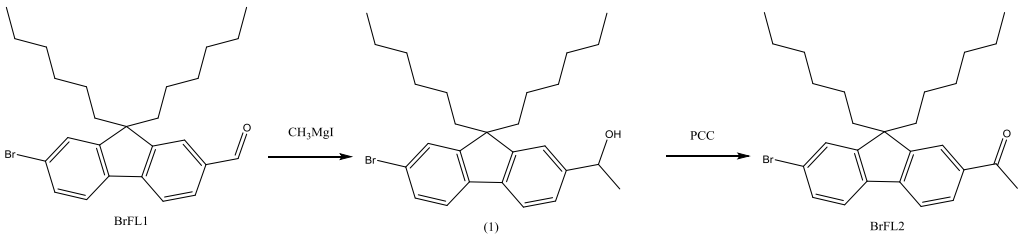

Scheme 2.3 Synthetic route to BrFL2.

Synthesis of 1-(7-bromo-9,9-dihexyl-9H-fluoren-2-yl)ethan-1-ol (Compound 1). BrFL1 (1 equiv.) was placed into a flame-dried reaction flask and vacuum purged with argon. Anhydrous THF was added, and the reaction flask was cooled to 0℃. CH_3MgI (3 M in diethyl ether, 3 equiv.) was slowly added to the solution. After stirring for 1 hour, the reaction was quenched by adding water. The resulting solution was extracted with diethyl ether, and the organic layer was washed with brine. The extracted organic layer was dried over $MgSO_4$, filtered, and evaporated under reduced pressure. Purification was performed by silica column chromatography with dichloromethane/hexane. White powder was collected in a yield of 40%. ^{1}H-NMR (400 MHz, $CDCl_3$): δ 7.62 (d, 1H), 7.53 (s, 1H), 7.46 (s, 1H), 7.43 (s, 1H), 7.35-7.31 (m, 2H), 4.98 (m, 1H), 4.77 (q, 1H), 1.83 (m, 4H), 1.54 (s, 3H), 1.14-0.98 (m, 12H), 0.77 (t, 6H), 0.60 (m, 4H).

Synthesis of 1-(7-bromo-9,9-dihexyl-9H-fluoren-2-yl)ethan-1-one (BrFL2). Starting materials (Compound 1) and PCC (pyridinium chlorochromate) were dissolved in dichloromethane. After stirring for 18 hours, the resulting solution was extracted with

dichloromethane, and the organic layer was washed with brine. The extracted organic layer was dried over $MgSO_4$, filtered, and evaporated under reduced pressure. Purification was performed by silica column chromatography with dichloromethane/hexane. White powder was collected in a yield of 20%. ^{1}H-NMR (500 MHz, $CDCl_3$): δ 7.97 (m, 2H), 7.74 (d, 1H), 7.63 (d, 1H), 7.50-7.48 (m, 2H), 2.66 (s, 3H), 2.05 (m, 4H), 1.12-0.98 (m, 12H), 0.8 (t, 6H), 0.6 (m, 4H).

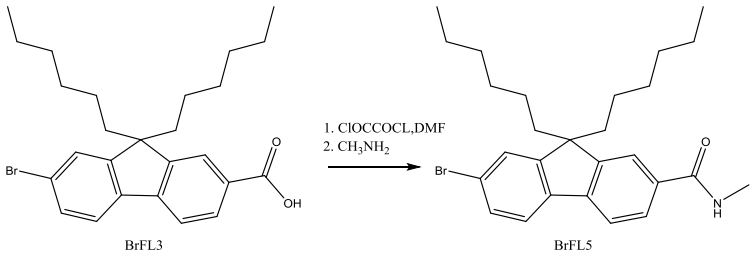

Scheme 2.4 Synthetic route to BrFL5.

Synthesis of 7-bromo-9,9-dihexyl-N-methyl-9H-fluorene-2-carboxamide (BrFL5). BrFL3 (1 equiv.) was loaded into anhydrous dichloromethane under an argon atmosphere. Oxalyl chloride (1.1 equiv.) was slowly added to the solution. After stirring for 30 min, a catalytic amount of anhydrous DMF was added, and the resulting solution was then stirred for 1 hour. This reaction solution was evaporated under reduced pressure. The resulting compound was dissolved in anhydrous dichloromethane. Next, CH_3NH_2 was added to the solution, and the solution was stirred overnight. The reaction solution was extracted with dichloromethane. The extracted organic layer was dried over $MgSO_4$, filtered, and evaporated under reduced pressure. Purification was performed by silica column chromatography with dichloromethane/hexane. White powder was collected in a yield of 79%. ^{1}H-NMR (500 MHz, $CDCl_3$): δ 7.98 (s, 1H), 7.68 (t, 2H), 7.57 (d, 1H), 7.49-7.46 (m, 2H), 6.02 (br, 1H), 3.06 (s, 3H), 1.96 (m, 4H), 1.13-0.99 (m, 12H), 0.76 (t, 6H), 0.54 (m, 4H).

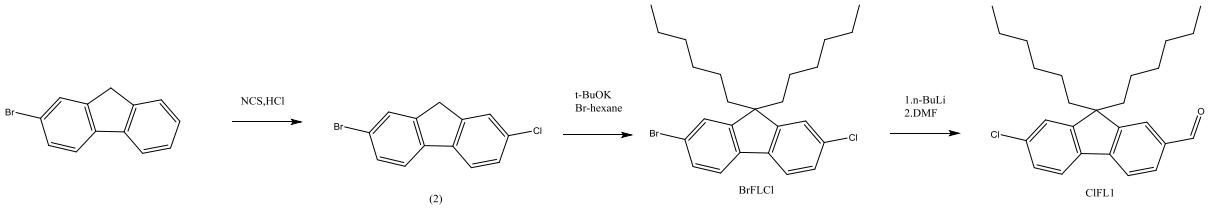

Scheme 2.5 Synthetic route to BrFLCl and ClFL1.

Synthesis of 2-bromo-7-chloro-9H-fluorene (Compound 2). 2-Bromo-9-H-fluorene (1 equiv.) and NCS (N-chlorosuccinimide) (2.5 equiv.) was dissolved in MeCN (acetonitrile, 1 g of each starting material per 1 mL of MeCN). The resulting solution was mechanically stirred in an ice bath. Saturated HCl (1 mL of HCl per 5 mL of MeCN) was added to the solution. The reaction temperature had to be kept below the boiling point of MeCN but above r.t. After adding HCL, the solution became clear, and a yellow powder precipitated after the temperature started to fall. The suspension was stirred overnight. The precipitated powder was filtrated and washed with MeCN and methanol. White powder was collected by recrystallization from methanol in a yield of 25%. ^{1}H-NMR (400 MHz, $CDCl_3$): δ 7.67 (s, 1H), 7.65 (d, 1H), 7.60 (d, 1H), 7.50 (d, 1H), 7.35 (d, 1H), 3.87 (s, 2H),

Synthesis of 2-bromo-7-chloro-9,9-dihexyl-9H-fluorene (BrFLCl). The reaction procedure was the same as that for the alkylation of 9H-fluorene for BrFLBr. Powder was collected in a yield of 63%. ^{1}H-NMR (400 MHz, $CDCl_3$): δ 7.56 (d, 1H), 7.51 (d, 1H), 7.4 (d, 1H), 7.43 (s, 1H), 1.91 (m, 4H), 1.16-1.00 (m, 12H), 0.77 (t, 6H), 0.58 (m, 4H).

Synthesis of 7-chloro-9,9-dihexyl-9H-fluorene-2-carbaldehyde (ClFL1). The reaction procedure was the same as that for the n-BuLi reaction of BrFLBr for BrFL1. Powder was collected in a yield of 67%. ^{1}H-NMR (400 MHz, $CDCl_3$): δ 10.07 (s, 1H), 7.87 (d, 1H), 7.86 (s, 1H), 7.70 (d, 1H), 7.37-7.35 (m, 2H), 2.04 (m, 4H), 1.14-1.00 (m, 12H), 0.77 (t, 6H), 0.56 (m, 4H).

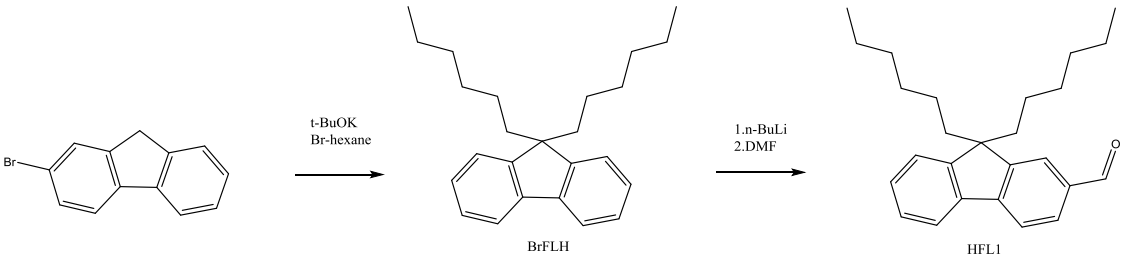

Scheme 2.6 Synthetic route to BrFLH and HFL1.

Synthesis of 2-bromo-9,9-dihexyl-9H-fluorene (BrFLH). The reaction procedure was the same as that for the alkylation of 9H-fluorene for BrFLBr. An oily liquid was collected in a yield of 63%. ^{1}H-NMR (400 MHz, $CDCl_3$): δ 7.66 (m, 1H), 7.55 (d, 1H), 7.46-7.42 (m, 2H), 7.33-7.30 (m, 3H), 1.95 (m, 4H), 1.16-0.99 (m, 12H), 0.77 (t, 6H), 0.60 (m, 4H).

Synthesis of 1-(7-bromo-9,9-dihexyl-9H-fluoren-2-yl)ethan-1-one (HFL1). The reaction procedure was the same as that for the n-BuLi reaction of BrFLBr for BrFL1. An oily liquid was collected in a yield of 71%. ^{1}H-NMR (400 MHz, $CDCl_3$): δ 10.06 (s, 1H), 7.87 (s, 1H), 7.85-7.82 (m, 2H), 7.80-7.75 (m, 1H), 7.39-7.35 (m, 3H), 2.00 (m, 4H), 1.13-0.98 (m, 12H), 0.75 (t, 6H), 0.58 (m, 4H).

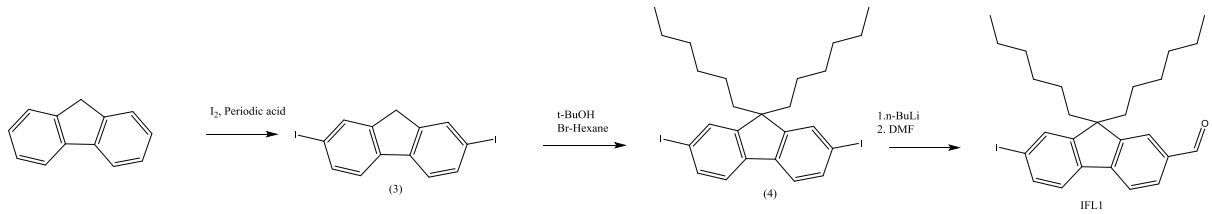

Scheme 2.7 Synthetic route to IFL1.

Synthesis of 2,7-diiodo-9H-fluorene (Compound 3). 9-H fluorene (1 equiv.) was added to the mixture of acetic acid, water, and H_2SO_4 (100:20:3). Periodic acid/iodine (0.33 equiv./0.75 equiv.) was added to the solution and dissolved at high temperature (~105℃). After cooling to 80℃, the resulting solution was stirred for 4 hours. The precipitate was filtered and washed with a 2 N Na_2CO_3 aqueous solution and water. Powder was collected by recrystallization from hexane in a yield of 25%. ^{1}H-NMR (400 MHz, $CDCl_3$): δ 7.88 (s, 2H), 7.70 (d, 2H), 7.50 (d, 2H), 3.84 (s, 2H)

Synthesis of 9,9-dihexyl-2,7-diiodo-9H-fluorene (Compound 4). The reaction procedure was the same as that for the alkylation of 9H-fluorene for BrFLBr. Powder was collected in a yield of 66%. ^{1}H-NMR (400 MHz, $CDCl_3$): 7.65-7.62 (m, 4H), 7.40 (d, 2H), 1.89 (m, 4H), 1.14-0.98 (m, 12H), 0.78 (t, 6H), 0.58 (m, 4H).

Synthesis of 9,9-dihexyl-7-iodo-9H-fluorene-2-carbaldehyde (IFL1). The reaction procedure was the same as that for the n-BuLi reaction of BrFLBr for BrFL1. Powder was collected in a yield of 53%. ^{1}H-NMR (400 MHz, $CDCl_3$): δ 10.05 (s, 1H), 7.88-7.30 (m, 2H), 7.80 (d, 1H), 7.71-7.69 (m, 2H), 7.51 (d, 1H), 1.97 (m, 4H), 1.14-0.98 (m, 12H), 0.76 (t, 6H), 0.56 (m, 4H).

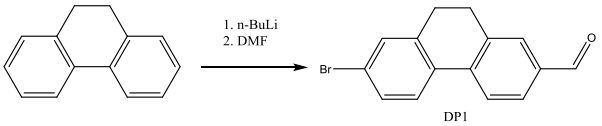

Scheme 2.8 Synthetic route to DP1.

Synthesis of 7-bromo-9,10-dihydrophenanthrene-2-carbaldehyde (DP1). The reaction procedure is the same as that for the n-BuLi reaction of BrFLBr for BrFL1. The powder was collected in a yield of 34%. ^{1}H NMR (400 MHz, CDCl3): δ 10.01 (s, 2 H). 7.95 (d, 2 H), 7.83 (d, 2 H), 7.77 (s, 2 H), 2.97 (s, 4 H).

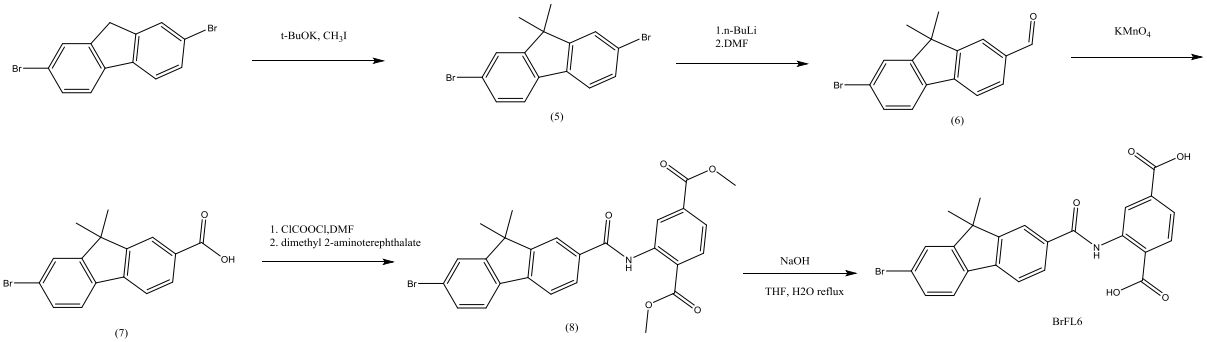

Scheme 2.9 Synthetic route to BrFL6.

Synthesis of 2,7-dibromo-9,9-dimethyl-9H-fluorene (Compound 5). The reaction procedure was the same as that for the alkylation of 9H-fluorene for BrFLBr, except that the alkylation compound was CH_3I instead of 1-bromohexane. Powder was collected in a yield of 50%. ^{1}H NMR (300 MHz, CDCl3): δ 7.52 (d, 2 H), 7.51 (d, 2 H), 7.43 (d, 2 H), 1.44 (s, 6 H).

Synthesis of 7-bromo-9,9-dimethyl-9H-fluorene-2-carbaldehyde (Compound 6). The reaction procedure was the same as that for the n-BuLi reaction of BrFLBr for BrFL1. Crude powder was collected in a yield of 55%. ^{1}H-NMR (300 MHz, $CDCl_3$): δ 10.0 (s, 1H), 7.96 (s, 1H), 7.86 (dd, 2H), 7.69-.7.63 (d, 2H), 7.54 (d, 1H), 1.96 (m, 4H), 1.54 (m, 6H).

Synthesis of 7-bromo-9,9-dimethyl-9H-fluorene-2-carboxylic acid (Compound 7). The reaction procedure was the same as that to oxidize BrFL1 for BrFL3. Powder was collected in a yield of 29%.^{1}H-NMR (300 MHz, DMSO-d6): δ 12.9 (br, 1H), 8.10 (s, 1H), 7.96 (s, 2H), 7.89 (d, 1H), 7.58 (d, 1H), 1.48 (m, 6H).

Synthesis of dimethyl 2-(7-bromo-9,9-dimethyl-9H-fluorene-2-carboxamido)terephthalate (Compound 8). Compound 7 (1 equiv.) was loaded into anhydrous dichloromethane under an argon atmosphere. Oxalyl chloride (1.1 equiv.) was slowly added to the solution. After stirring for 30 min, a catalytic amount of anhydrous DMF was added, and the resulting solution was stirred for 1 hour. Then, the reaction solution was evaporated under reduced pressure. The resulting powder was dissolved in anhydrous dichloromethane. Dimethyl 2-aminoterephthalate (1 equiv.) was added to the solution, and the solution was stirred overnight. The organic layer extracted by dichloromethane was collected and dried over $MgSO_4$ before being filtered and evaporated under reduced pressure. Purification was performed by column chromatography with hexane/dichloromethane. Powder was collected in a yield of 80%.^{1}H-NMR (300 MHz, CDCl3): δ 12.07 (br, 1H), 9.59 (s, 1H), 8.16 (s, 1H and d, 1H), 8.02 (d, 1H), 7.80 (s, 1H and d, 1H), 7.62 (s, 1H and d, 1H), 7.50 (d, 1H), 1.48 (m, 6H). 4.00 (s, 3H), 3.96 (s, 3H), 1.53 (s, 6H)

Synthesis of 2-(7-bromo-9,9-dimethyl-9H-fluorene-2-carboxamido)terephthalic acid (BrFL6). Compound 8 was dissolved into the THF solution, and then, saturated NaOH aqueous solution was added. The reaction was refluxed overnight. After cooling, saturated HCl was carefully added to the reaction solution in an ice bath until a white powder precipitated. The powder was filtrated and washed with water and dried before being collected in a yield of 90%. ^{1}H-NMR (300 MHz, DMSO-d6): δ 9.28 (s, 1H), 8.15 (s, 1H and d, 1H), 8.08 (d, 1H), 7.99-7.90 (m, 3H), 7.73 (d, 1H), 7.61 (d, 1H), 1.48 (m, 6H). 4.00 (s, 3H), 1.52 (s, 6H)

2.3 Results and Discussion

2.3.1 Effect of structural rigidity on phosphorescence

The effect of structural rigidity on fluorescence has been well investigated. For example, rigid fluorene has a higher fluorescent QY of up to 100% than twisting biphenyl, which has only a 20% QY. This lower QY is caused by the increased internal conversion rate (K_{IC}) originated from intramolecular rotational motion. The rigid polymer matrix can suppress the intramolecular motion and increase the fluorescent QY. For example, the AIE (aggregation-induced emission) or AIEE (aggregation-induced enhanced emission) molecules are

nonemissive or weakly emissive in solution but can emit intensely in a polymer matrix[18] due to the restricted rotational motion of the molecule. We investigated how molecular rigidity of metal-free organic phosphors influences their RTP in a polymer matrix. For this study, we chose BrFL1 as the rigid molecule, DP1 as the bridged biphenyl derivative, and BP1 as the unfixed molecule. These three molecules have a similar core structure of linked bond two benzene rings

The three molecules were embedded into atactic poly(methyl methacrylate) (aPMMA) and the resulting blend was sandwiched between two glass substrates with epoxy sealing in order to prevent oxygen quenching. BrFL1, DP1, and BP1 in aPMMA showed similar spectra with green phosphorescence (Fig. 2.2). The emission spectra of more rigid molecules achieved by bridging between the benzene rings have a more defined structure. BrFL1 exhibits bright phosphorescence with a QY of Φ_p=29.7% and a phosphorescent lifetime of τ_p=17.0 ms (Table 2.1). Compared to that of BrFL1, a lower QY was observed for DP1 (Φ_p =15.1%, τ_p=10.3 ms) and BP1 (Φ_p=13.0%, τ_p=8.82 ms). Interestingly, the calculated rate constants of phosphorescent radiative decay of BrFL1 (K_p=17.5 s^{-1}) was not very different from those of DP1 (14.6 s^{-1}) and BP1 (13.7 s^{-1}). Due to the similar T1 energy level of these molecules based on their emission spectra, their activation energies of Dexter-type triplet energy transfer (K_q) are similar, implying that their K_q values are also similar with each other. Therefore, the lower phosphorescent QY with a lack of molecular rigidity can be explained by the increase in nonradiative decay rate caused by intramolecular vibration (K_{TS}). In a recent paper, Hirata[16] reported that twisting aromatic framework relaxes the spin-forbidden process during the T_1–S_0 transition, which increases the prohibition factors caused by changes in the spin configuration, thus increasing K_{TS}. The K_{nr} of BP1 (98.6 s^{-1}) is higher than those of BrFL1 (41.4 s^{-1}) and DP1 (60.6 s^{-1}), indicating that the lack of rigidity can dominantly affect K_{TS}. Thus, to achieve bright phosphorescence in a polymer system, a rigid molecular structure is of high importance.

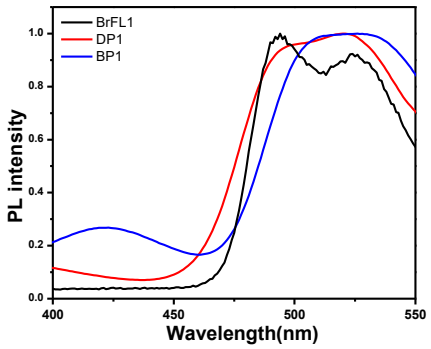

Figure 2.2 Steady-state emission spectra of BrFL1-, DP1-, and BP1-embedded aPMMA film at r.t..

Table 2.1 Photophysical data of BrFL1-, DP1- and BP1-embedded aPMMA film at r.t.

	Φ_p(%)	τ_p(ms)	K_p(S^{-1}) if ISC=100%	K_{nr}(S^{-1}) if ISC=100%
BrFL1	29.7	17.0	17.5	44.1
DP1	15.1	10.3	14.6	60.6
BP1	13.0	8.82	13.7	98.6

2.3.2 Effect of modifying halide and functional group on phosphorescent radiative decay (K_p)

Unlike BrFLBr, BrFL1 exhibits RTP (Figure 2.1). In the previous study, the aldehyde and bromine of FL1 were identified as essential design elements to achieve RTP[11]. However, the effect of combining a carbonyl group and a halide was not investigated. Since the excited electron in the n,π* state is localized on the carbonyl group, intramolecularly the n,π* state may not be under the influence of the heavy-atom effect of the halide.

Time-dependent density functional theory (TD-DFT) was used to understand the role of the substitution in the phosphorescence of BrFL1. As shown in Fig. 2.3(d), ISC from $S_1(n\pi^*)$ to $T_3(\pi\pi^*)$ is allowed by the El Sayed rule; then, $T_3(\pi\pi^*)$ relaxes to $T_1(\pi\pi^*)$, which is governed by the heavy-atom effect during the phosphorescent transition. According to the computation, the aldehyde in fluorene plays a critical role in singlet-to-triplet ISC, and bromine enhances the SOC of the T_1-to-S_0 transition, providing efficient phosphorescence.

We synthesized and characterized the photophysical properties of BrFL1 derivatives,

HFL1, ClFL1, and IFL1, in a chloroform solution and embedded in a polymer. Although the ISC from the singlet to triplet state is the same pathway in these molecules, and their energy gaps are almost identical, the difference in the size or the existence of the halide influences their fluorescence QY and the ISC. The fluorescence QY (Φ_f) of HFL1 is 4.53%, and Φ_f decreases gradually as the size of the halide increases. Thus, IFL1 is very weakly fluorescent in the chloroform solution, with Φ_f=0.3% (see Table 2.2). The weak fluorescence in this series of molecules indicates efficient singlet-to-triplet ISC. The molecular orbital configurations of the S_0-to-S_1 transition are very similar due to the almost identical shape of their absorption spectra (Fig. 2.3(a)), which can suggest very similar fluorescence oscillation strengths in the series of molecules. Therefore, with the increase in the size of halide, it is concluded that ISC from singlet-to-triplet becomes more efficient based on the very low fluorescence intensity. Although S_1 is $n\pi^*$ that is not governed by the heavy-atom effect, the experimental results suggest that singlet-to-triplet ISC is promoted by the heavy-atom effect owing to the $S_2(\pi\pi^*)$-$S_1(n\pi^*)$ mixing promoted by the low energy gap between S_2 and S_1 (<0.3 eV)[19]. The energy level of $S_1(n\pi^*)$ can be affected by the solvent polarity, indicating that the energy level obtained from the TD-DFT calculation in vacuum conditions can be different from that in chloroform solution[19,20]. The aldehyde and halide attached to the fluorene moiety can promote ISC from $S_2(\pi\pi^*)$-$S_1(n\pi^*)$ mixing to $T_3(\pi\pi^*)$ via the El-Sayed rule as well as the heavy-atom effect.

To compare the phosphorescent properties, aPMMA films having the phorphors were prepared with the same epoxy sealing in order to prevent oxygen quenching. Green phosphorescence was observed only from ClFL1 and BrFL1. The SOC of the $T_1(\pi\pi^*)$-to-$S_0(\pi\pi)$ transition is only enhanced by the heavy-atom effect of the halide. Thus, For that reason, HFL1 without having any halogen has weak SOC of this transition and hence does not exhibit RTP. The phosphorescent QY and lifetime of ClFL1 were measured (Φp=8.05%, τ_p=19.4 ms), and the calculated rate of radiative decay (k_p) of ClFL1 is much lower than that of BrFL1 due to the lighter chlorine atom. The experimental data demonstrate that singlet-to-triplet ISC and phosphorescent radiative decay process of BrFL1 derivatives are largely governed by the halide. Although IFL1 exhibits bright phosphorescence at 77 K, RTP from IFL1 was not observed. Because IFL1 is highly sensitive to polymer relaxation, the phosphorescent intensity starts to decrease even at a low temperature and becomes too weak at r.t., which will be discussed in the next section.

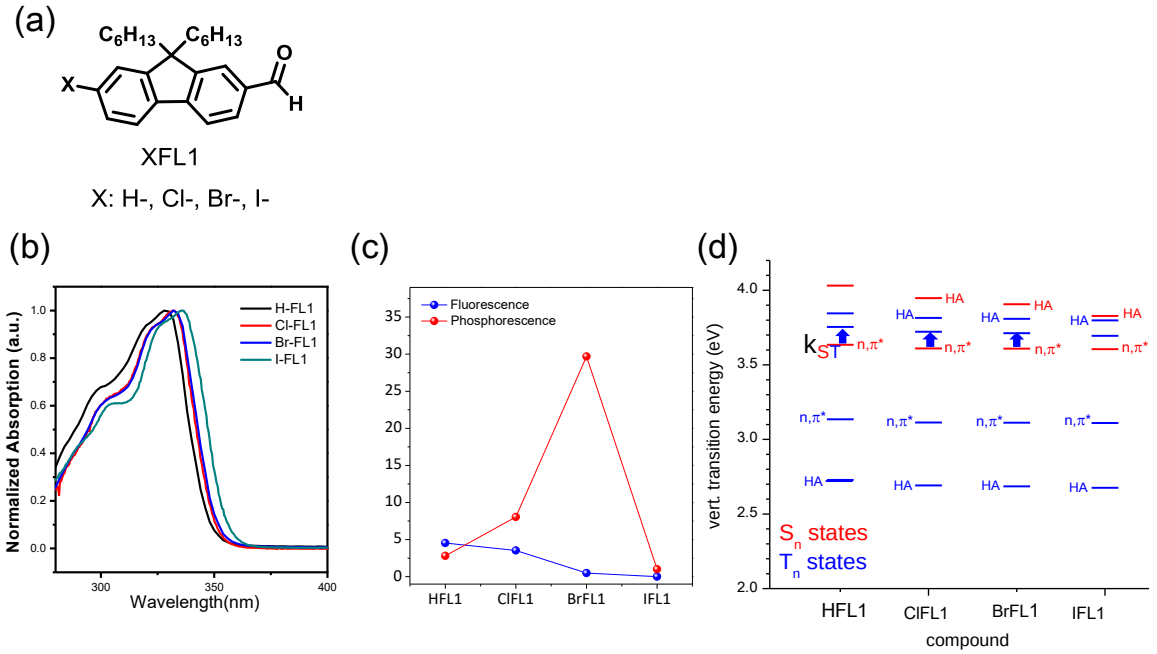

Figure 2.3 (a) Chemical structure of compounds H-, Cl-, Br- and IFL1. (b) Absorption spectra of the compounds in chloroform solution (2×10^{-5} molL^{-1}). (c) Fluorescence and phosphorescence QY of the compounds. (d) Singlet and triplet energy diagram of the molecules as calculated by TD-DFT.

Table 2.2 Photophysical data of HFL1, ClFL1, BrFL1, and IFL1

	Absorption(nm) [a]	Phosphorescence Emission(nm) [b]	Fluorescence quantum yield(%) [a]	Phosphorescence quantum yield(%) [b]	Phosphorescence lifetime(ms)	Radiative constant (Kp,S^{-1}) if ISC=100%
H-FL1	328	525	4.53	2.8	Not determined	Not determined
Cl-FL1	330	524	3.53	8.05	19.4	4.15
Br-FL1	330	525	0.49	29.7	17.0	17.5
I-FL1	337	535	<0.1%	<1%	Not determined	Not determined

[a] Measured in 2×10^{-5} molL^{-1} $CHCl_3$ solution. [b] Measured from dye-doped aPMMA film under inert conditions.

Although using a heavy halide is key to achieving strong SOC for the $T_1(\pi\pi^*)$-to-$S_0(\pi\pi)$ transition and the resulting bright phosphorescence, the aldehyde moiety is also critical to RTP of bromofluorene derivatives. For example, dibromofluorene (BrFLBr) exhibits very weak phosphorescence[12]. To systematically investigate the role of the aldehyde group, we designed various carbonyl groups with the aldehyde group the aldehyde group such as trifluoro-ethanone (BrFL0), ketone (BrFL2), carboxylic acid (BrFL3), ester (BrFL4), and amide (BrFL5) (Fig. 2.4). From BrFL0 to BrFL5, the absorption and phosphorescent emission spectra are blue-shifted because the resonance of carbonyl becomes stabilized.

Electron-releasing groups such as O and N reduce the resonance energy of carbonyl and reduce the double-bond character of C=O that is conjugated to the fluorene, thus increasing the band gap and the T_1 energy level of the molecules.

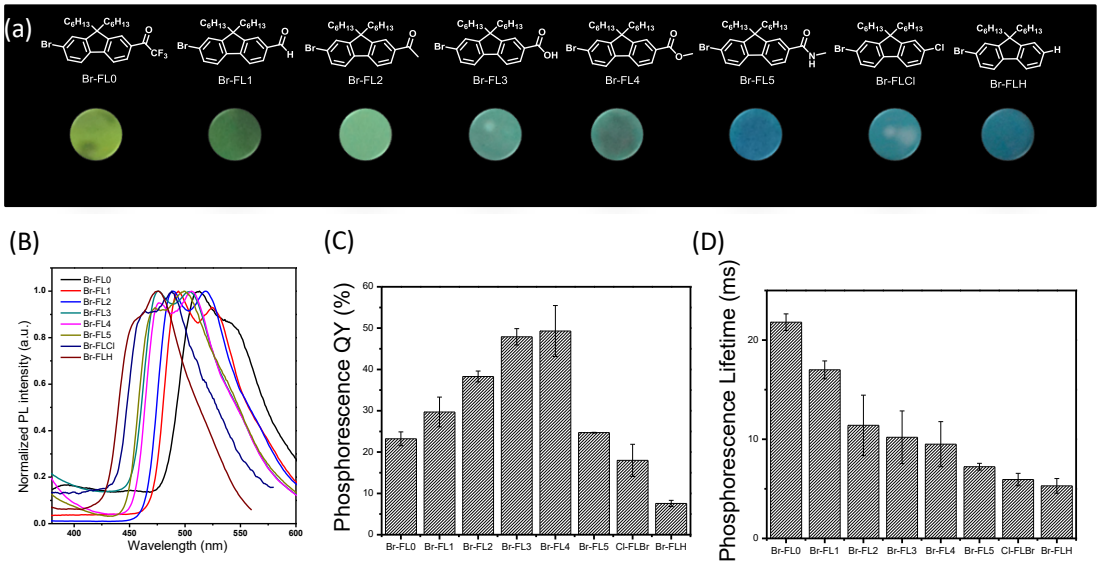

Figure 2.4 (a) Chemical structure of compounds BrFL molecules and images of their phosphorescent colors upon UV irradiation (365 nm) under N_2. (b) Steady-state emission spectra of BrFL compounds in aPMMA films. (c) QY of BrFL compounds. (d) Phosphorescence lifetime of BrFL compounds.

Phosphorescent properties of dye-doped aPMMA films with epoxy sealing were measured at r.t. BrFL0 having an electron-withdrawing group connected to the carbonyl is brightly phosphorescent, with a QY of Φ_p=23.2% and lifetime of τ_p=21.8 ms at λ_{max}=543 nm. As we explained above, the red-shifted emission of BrFL0 relative to that of BrFL1 is caused by the higher energy of resonance stabilization of the carbonyl. Bright phosphorescence was observed for BrFL2 (Φ_p=38.3%, τ_p=11.4 ms), BrFL3 (Φ_p=47.9%, τ_p=10.2 ms), BrFL4 (Φ_p=49.3%, τ_p=9.50 ms), and BrFL5 (Φ_p=24.7%, τ_p=7.23 ms) (Table 2.3). Remarkably, the fluorescent QYs of BrFL3 and BrFL4 are over 20%, which are much higher than those of the rest of the series of molecules, indicating that singlet-to-triplet ISC is less efficient, although their phosphorescence are brightest.

Table 2.3 Photophysical data of BrFL molecules

	Absorption(nm)[a]	Phosphorescence Emission(nm)[b]	Fluorescence quantum yield(%)[a]	Phosphorescence quantum yield(%)[b]	Phosphorescence lifetime(ms)[b]	Radiative constant (K_p,S^{-1}) if ISC=100%	Non Radiative constant (K_{nr},S^{-1}) if ISC=100%
BrFL0	340	543	2.49	23.2	21.8	10.6	35.1
BrFL1	330	525	0.49	29.7	17.0	17.5	41.4
BrFL2	327	520	0.12	38.3	11.4	33.6	54.1
BrFL3	321	505	28.9	47.9	10.2	47.0	51.1
BrFL4	317	505	22.8	49.3	9.50	51.9	53.3
BrFL5	317	497	0.26	24.7	7.23	34.2	104
BrFLCl	315	489	3.53	18.0	5.94	30.3	138
BrFLH	309	475	2.02	7.57	5.3	14.3	174.7

[a] Measured in 2×10^{-5} $molL^{-1}$ $CHCl_3$ solution. [b] Measured from dye-doped aPMMA film under inert conditions.

To identify the reason for the brightest phosphorescence of BrFL3 and BrFL4, the logarithm of the calculated rate of nonradiative decay (k_{nr}) is plotted as a function of the T_1 energy level (Fig. 2.5), $\log(k_{nr})$ is proportional to the T_1 energy level. Quenching caused by Dexter-type triplet energy transfer (k_q) is governed by the Arrhenius equation, and the activation energy becomes smaller when the T_1 of the guest molecule is close to that of the aPMMA matrix. From BrFL0 to BrFL5, the energy level of T1 increases, and hence, the activation energy of k_q decreases; thus, the plot of $\log(k_{nr})$ vs. T_1 should be linear. Although the k_{nr} values of BrFL3 and BrFL4 are higher, their phosphorescent QYs are higher than those of BrFL0, BrFL1, and BrFL2, which suggests that the higher phosphorescent QY cannot be explained solely by lowering the phosphorescent quenching or non-radiative decay.

Interestingly, even though the value is underestimated due to their low Φ_{ISC}, the calculated rated of phosphorescent radiative decay of BrFL3 (k_p=47.0 s^{-1}) and BrFL4 (k_p=51.9 s^{-1}) are much higher than those of BrFL0 (k_p=10.6 s^{-1}), BrFL1 (k_p=17.5 s^{-1}), BrFL2 (k_p=33.6 s^{-1}) and BrFL5 (k_p=34.2^{-1}). Because the $T_1(\pi\pi^*)$-to-$S_0(\pi\pi)$ radiative transition is spin forbidden, a spin inversion mechanism is required to achieve bright phosphorescence. The strong SOC from $T_1(\pi\pi^*)$ to $S_0(\pi\pi)$ is governed by the heavy-atom effect. Therefore, the high value of k_p of BrFL3 and BrFL4 can be explained by a strong heavy-atom effect in the molecules. It has been reported that an efficient photosensitizer including iodine or bromine cannot exhibit phosphorescence, even at 77 K.

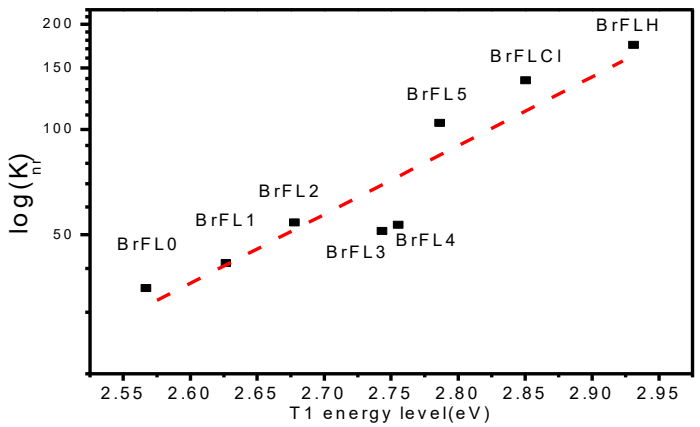

Figure 2.5 Plot of log(K_{nr}) vs. T1 energy level of BrFL molecules.

To examine the role of carbonyl further, we synthesized bromo-fluorene derivatives having an electron-withdrawing group instead of carbonyl. If this functional substitution has a similar effect on SOC in radiative transition, then the molecules can exhibit bright phosphorescence. BrFLCl and BrFLH show blue-shifted absorption and phosphorescent emission spectra because the electron-withdrawing power of Cl and H is weaker than that of carbonyl in terms of mesomeric effects. The phosphorescent QY and lifetime were measured for BrFLCl (Φ_p=18.0%, τ_p=7.57 ms) and BrFLH (Φ_p=5.94%, τ_p=5.30 ms). The Arrhenius plot of k_{nr} versus T_1 energy was linearly fitted for BrFL0-BrFL5. The results clearly indicate that carbonyl and other functional groups can influence the magnitude of SOC and heavy-atom effect of Br on the other side of the molecule, thus enhancing phosphorescence even at r.t.

Although k_p of BrFLCl (k_p=30.3 s^{-1}) is much higher than that of BrFL0 (k_p=10.6 s^{-1}), the phosphorescent QY of BrFLCl is lower due to its higher T_1 energy and the consequent larger k_{nr}. Bright blue phosphorescence from metal-free phosphors in embedded polymers is much more challenging than green or red phosphorescence because a high T1 energy decreases the activation barrier of Dexter-type triplet energy transfer (k_q) and hence promotes phosphorescence quenching. Thanks to the large Stokes shift of phosphorescence, red phosphorescence from metal-free phosphors would be more promising for bioapplications.

2.3.3 The correlation between the molecular structure and type of polymer relaxation to quench phosphorescence

The phosphorescent intensity and photophysical processes of metal-free phosphors in a polymer matrix are strongly affected by thermal motion, glass transition, and other secondary interactions between the polymer matrix and phosphors[7,15]. It has been reported that the phosphorescent intensity of metal-free phosphors such as benzophenone, Br6A, and the fluorene-based phosphors in aPMMA, decayed at the β-relaxation temperature (T_β ~250 K), the onset of the rotational motion of the ester group (Fig. 2.1) and the α'-relaxation temperature ($T_{\alpha'}$~300 K), considering the onset of local motion of the main CH_2 chain of the PMMA matrix. Although aPMMA is a well-known bio-applicable material due to its good biocompatibility, easy manipulation in hospital settings, thermal stability, chemical inertness, because β-relaxation occurs at a much lower temperature than body temperature, the prevailing non-radiative decay and consequent phosphorescence quenching prevent aPMMA from certain bioapplications when it is used with metal-free organic phosphors. Temperature-dependent measurements showed that the phosphorescent intensity of metal-free phosphors in aPMMA begins to decay at different temperatures depending on the molecular structure of the phosphors. This finding may represent a method to overcome the limitations of aPMMA in phosphorescent bioapplications or photodynamic therapy.

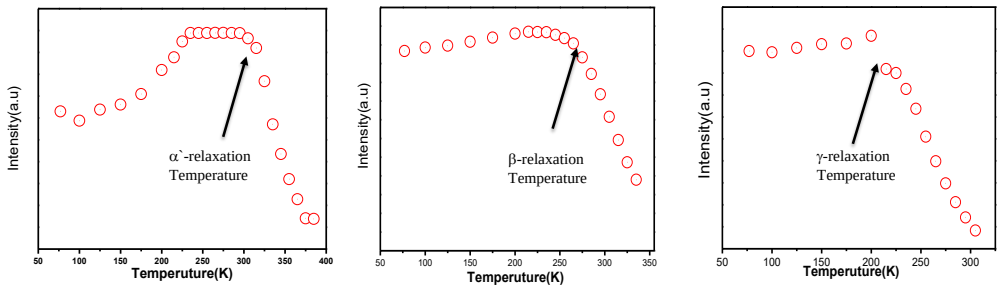

Figure 2.6 Phosphorescence intensity of BrFL1-, BrFL6-, and IFL1-embedded aPMMA at various temperatures under vacuum.

We prepared aPMMA films having embedded phosphors and measured their phosphorescent intensity at various temperatures under vacuum (<10^{-4} Torr) (Fig. 2.6). The phosphorescent intensity generally decreases with increasing temperature due to the activation of thermal motion; however, the intensity of BrFL1 in PMMA at r.t. is higher than

that at 77 K. We found that the intensity at 300 K is 1.44 times brighter than that at 77 K, which is almost the same as their absolute QY ratio of 1.43)[21], indicating that the result is not measurement error. The calculated rate of radiative decay at 77 K of k_p=7.98 s^{-1} is less than half of that at 300 K. We believe that the promoted out-of-aromatic-ring-plane vibration modes at 300K enhance the singlet-to-triplet ISC, driven by Herzberg–Teller vibronic coupling, thereby, the relative inefficient singlet-to-triplet ISC at 77 K may cause an underestimation of the calculated k_p compared to the k_p at 300K.[22].

Interestingly, the phosphorescent intensity of BrFL1 was observed to decrease with increasing temperature above 300 K, i.e., α'-relaxation, indicating that the active motion to quench phosphorescence of BrFL1 is the local motions of the aPMMA chains, not the rotation of the ester groups. The phosphorescence of flexible phosphors[23] and rigid molecules with ultra emission phosphorescence (e.g., coronene and deuterated coronene[24] in aPMMA) was reported to experience emission quenching at above 250 K, i.e., β'-relaxation. In contrast to the outcome of these previous studies, the phosphorescent behavior of BrFL1 in aPMMA cannot be explained by the rigidity of the molecule or the lifetime of the triplet state.

The phosphorescent intensity of IFL1 decreases with increasing temperature starting at 200 K, approximately the γ'-relaxation temperature, which corresponds to the rotation of the methyl group of aPMMA, up to room temperature. Therefore, IFL1 is much more sensitive to the thermal motion of aPMMA than coronene and BrFL1 because the motion of γ'-relaxation is smaller than that of β'- or α'-relaxation. Despite strong phosphorescence of IFL1 in aPMMA at 77 K with a shorter lifetime (~τ_p ms), the phosphorescence is significantly quenched when the temperature increases above 200 K. Therefore, no RTP was observed from IFL1. We believe that the shorter lifetime of IFL1 is not the reason for this result because a smaller number of collisions between the polymer and phosphors is expected during the faster decay of the triplet excimers. Since the only difference between BrFL1 and IFL1 is the halide substitution or the size of the halide, we hypothesize that the large size of iodine on fluorene causes IFL1 to be more sensitive to small motions of polymer relaxation such as γ'-relaxation.

To devise bright metal-free phosphors based on the BrFL framework whose phosphorescence is quenched not by γ'-relaxation but by β'-relaxation, we did thorough literature study. Hirata *et. al.* reported fluorene-based metal-free phosphors that exhibit phosphorescence quenching with increasing temperature at the β'-relaxation temperature of

aPMMA. We note that those reported fluorene-based metal-free phosphors have bulkier side groups than BrFL1. Based on the size of the molecule, we designed and synthesized BrFL6 (Scheme 2.9), which has a similar molecular structure to that of BrFL5 in terms of phosphor moiety. Because the amide linkage can break the π conjugation between fluorene and the terephtalic acid moiety, BrFL6 can exhibit similar intrinsic photophysical properties (λ_{max}=497 nm, τ_p=8.6 ms) with BrFL5 (Fig. 2.7)[25]. The overall size of and structure of BrFL6 are similar to those of the reported fluorene-based metal-free phosphors. Indeed, the phosphorescence of BrFL6 in aPMMA was observed to decay above 250 K, the β'-relaxation temperature. Owing to the higher quenching temperature, the triplet lifetime or phosphorescence lifetime of BrFL6 (τ_p=8.6 ms) is shorter than that of BrFL5. Although the overall size of BrFL6 is larger than that of IFL1, it turned out that IFL1 is more sensitive to the thermal motion of matrix polymer. We believe that the effect of molecular size in the out-of-aromatic-ring-plane (IFL1) and in-plane (BrFL6) directions must be investigated further to understand these distinct phenomena more clearly.

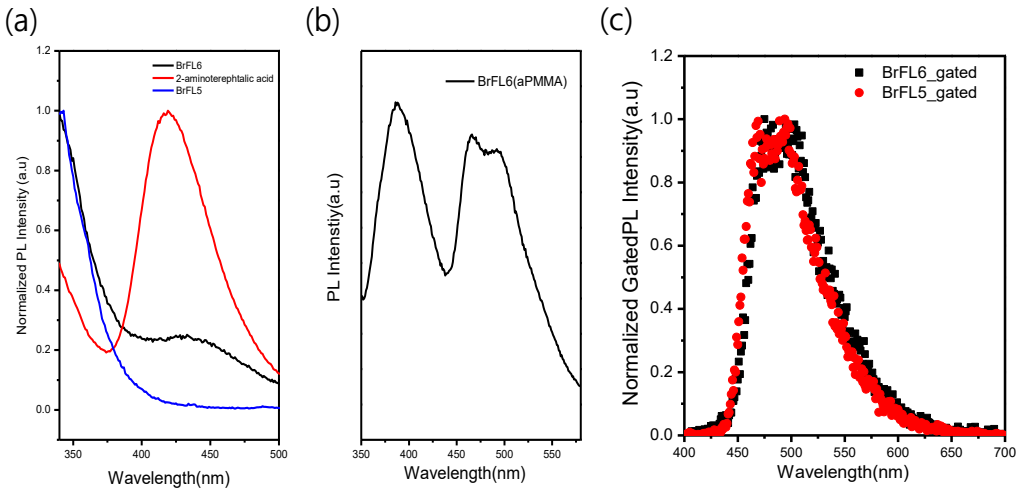

Figure 2.7 (a) Normalized steady-state PL spectra of BrFL5, BrFL6 and 2-aminophthalic acid in DMF. (b) Steady-state PL spectrum of BrFL6-doped aPMMA film. (c) Gated PL spectra of BrFL5- and BrFL6-doped aPMMA film.

The above study suggests that a small metal-free phosphor is more promising for achieving RTP in a polymer matrix. In particular, iodine-containing metal-free phosphors turned out to be very sensitive to the thermal motion of polymer matrix and consequently do not produce RTP. However, efficient RTP from a boron-chelating molecule attached to iodine

and poly(lactic acid) has been reported[2]. The interactions between metal-free phosphors and thermal motion may be different in different polymer matrixes. Additional systematic studies to understand these phenomena will be conducted in the future.

2.4. Conclusion

In summary, we have developed a new molecular design for metal-free phosphors with highly efficient RTP. Rigidity of the molecular structure is important for suppressing intramolecular vibration quenching and enhancing the RTP of metal-free phosphors. Functional group substitution on metal-free phosphors via halogen variation and carbonyl modification can largely influence SOC from T_1 to S_0 and the heavy-atom effect. The size of the molecules or halide affects the sensitivity of the phosphors to polymer relaxation. Therefore, generally the triggering temperature for phosphorescence quenching varies by the molecular size. Our experimental and theoretical studies may provide a useful guideline for developing phosphors for various applications such as bio-imaging, sensing, and photodynamic therapy.

2.5 References

1. a) Baldo, M. A., O'brien, D. F., You, Y., Shoustikov, A., Sibley, S., Thompson, M. E., and Forrest, S. R. "Highly Efficient Phosphorescent Emission from Organic Electroluminescent Devices." *Nature* **1998**, 395, 151-154; b) Anzenbacher, P., Pérez-Bolívar, C., Takizawa, S.Y. and Brega, V., "Room-temperature Electrophosphorescence from an All-organic Material." *J. Lumin.* **2016**, 180, 111-116; c) Chaudhuri, D., Sigmund, E., Meyer, A., Röck, L., Klemm, P., Lautenschlager, S., Schmid, A., Yost, S.R., "Metal-Free OLED Triplet Emitters by Side-Stepping Kasha's Rule." *Angew. Chem. Int. Ed*. **2013**, 52, 13449-13452
2. a) Zhang, G., Palmer, G.M., Dewhirst, M.W. and Fraser, C.L.,"A Dual-emissive-Materials Design Concept Enables Tumour Hypoxia Imaging." *Nat. Mater.* **2009**, 8, 747-751; b) Zhen, X., Tao, Y., An, Z., Chen, P., Xu, C., Chen, R., Huang, W. and Pu, K., "Ultralong Phosphorescence of Water-soluble Organic Nanoparticles for in vivo Afterglow Imaging." *Adv. Mater.* **2017**, 29, 1606665
3. Sterenborg, H.J.C.M., de Wolf, J.W., Koning, M., Kruijt, B., van den Heuvel, A. and Robinson, D.J., "Phosphorescence-fluorescence Ratio Imaging for Monitoring the Oxygen Status During Photodynamic Therapy." *Opt. Express.* **2004**, 12, 1873-1878.
4. a) Telitel, S., Dumur, F., Telitel, S., Soppera, O., Lepeltier, M., Guillaneuf, Y., Poly, J., Morlet-Savary, F., Fioux, P., Fouassier, J.P. and Gigmes, D., "Photoredox Catalysis Using a New Iridium Complex as an Efficient Toolbox for Radical, Cationic and Controlled Polymerizations under Soft Blue to Green Lights." *Polym. Chem.*, **2015**, 6, 613-624; b) Garcia-Garibay, M.A., "Advances at the Frontiers of Photochemical Sciences," *J. Am. Chem. Soc*. **2012**, 134, 8289-8292
5. a) Mathew, A.S., DeRosa, C.A., Demas, J.N. and Fraser, C.L.,"Difluoroboron β-diketonate Materials with Long-lived Phosphorescence Enable Lifetime based Oxygen Imaging with a Portable Cost Effective Camera." *Anal. Methods* **2016**, 8, 3109-3114; b) Yu, Y., Kwon, M.S., Jung, J., Zeng, Y., Kim, M., Chung, K., Gierschner, J., Youk, J.H., Borisov, S.M. and Kim, J., "Room-temperature-phosphorescence-based Dissolved Oxygen Detection by Core-shell Polymer Nanoparticles Containing Metal-free Organic Phosphors." *Angew. Chem. Int. Ed*. **2017**, 56, 162071-16211.

6. a) Andrews, R.E., Shah, K.M., Wilkinson, J.M. and Gartland, A., "Effects of Cobalt and Chromium Ions at Clinically Equivalent Concentrations after Metal-on-metal Hip Replacement on Human Osteoblasts and Osteoclasts: Implications for Skeletal Health." *Bone* **2011,** 49**,** 717-723; b) Plaza, S.M., "The Safety and Efficacy of High-dose Chromium." *Altern. Med. Rev.* **2002**, 7, 218-235.

7. a) Kwon, M.S., Yu, Y., Coburn, C., Phillips, A.W., Chung, K., Shanker, A., Jung, J., Kim, G., Pipe, K., Forrest, S.R. Youk, J.H., Gierschner, J., and Kim, J., "Suppressing Molecular Motions for Enhanced Room-temperature Phosphorescence of Metal-free Organic Materials." *Nat. Commun.*, **2015**, 6, 1-9; b) Hirata, S., Totani, K., Zhang, J., Yamashita, T., Kaji, H., Marder, S.R., Watanabe, T. and Adachi, C., "Efficient Persistent Room-temperature Phosphorescence in Organic Amorphous Materials under Ambient Conditions." *Adv. Funct. Mater.* **2013**, 23, 3386-3397.

8. Turro, N. J., *Modern Molecular Photochemistry* (University Science Books, Sausalito CA, **1991**)

9. Sarkar, S., Hendrickson, H.P., Lee, D., DeVine, F., Jung, J., Geva, E., Kim, J. and Dunietz, B.D., "Phosphorescence in Bromobenzaldehyde can be Enhanced through Intramolecular Heavy Atom Effect." *J. Phys. Chem. C* **2017**, 121, 3771-3777.

10. Kamkaew, A., Lim, S.H., Lee, H.B., Kiew, L.V., Chung, L.Y. and Burgess, K., "BODIPY Dyes in Photodynamic Therapy." *Chem. Soc. Rev.* **2013**, 42, 77-88.

11. Wu, W., Guo, H., Wu, W., Ji, S. and Zhao, J., "Organic Triplet Sensitizer Library Derived from a Single Chromophore (BODIPY) with a Long-lived Triplet Excited State for Triplet–Triplet Annihilation based Upconversion." *J. Org. Chem.* **2011**, 76, 7056-7064

12. a) Zhang, X.F., Yang, X., Niu, K. and Geng, H., "Phosphorescence of BODIPY dyes." *J. Photochem. Photobiol. A: Chem.* **2014**, 285, 16-20; b) Xu, J., Takai, A., Kobayashi, Y. and Takeuchi, M., "Phosphorescence from a Pure Organic Fluorene Derivative in Solution at Room Temperature.", *Chem. Commun.* **2013**, 49, 8447-8449; c) Miller, J.C., Meek, J.S. and Strickler, S.J., "Heavy Atom Effects on the Triplet Lifetimes of Naphthalene and Phenanthrene." *J. Am. Chem. Soc.* **1977**, 99, *25, 8175-8179,*

13. a) Yuan, W.Z., Shen, X.Y., Zhao, H., Lam, J.W., Tang, L., Lu, P., Wang, C., Liu, Y., Wang, Z., Zheng, Q. and Sun, J.Z., "Crystallization-induced Phosphorescence of Pure Organic Luminogens at Room Temperature." *J. Phys. Chem. C* **2010**, 114, 6090-6099; b) Bolton,

O., Lee, K., Kim, H.J., Lin, K.Y. and Kim, J., "Activating Efficient Phosphorescence from Purely Organic Materials by Crystal Design." *Nat. Chem.* **2011**, 3, 205-210 l c) Gao, H.Y., Shen, Q.J., Zhao, X.R., Yan, X.Q., Pang, X. and Jin, W.J., "Phosphorescent Co-crystal Assembled by 1, 4-diiodotetrafluorobenzene with Carbazole based on C–I··· π Halogen Bonding." *J. Mater. Chem.* **2012**, 22, 5336-5343 (2012)

14. Bolton, O., Lee, D., Jung, J. and Kim, J., "Tuning the Photophysical Properties of Metal-Free Room Temperature Organic Phosphors via Compositional Variations in Bromobenzaldehyde/Dibromobenzene Mixed Crystals." *Chem. Mater*. **2014**, 26, 6644-6649
15. a) Lee, D., Bolton, O., Kim, B.C., Youk, J.H., Takayama, S. and Kim, J., "Room-Temperature Phosphorescence of Metal-free Organic Materials in Amorphous Polymer Matrices." *J. Am. Chem. Soc*. **2013**, 135, 6325-6329; b) Kwon, M.S., Lee, D., Seo, S., Jung, J. and Kim, J., "Tailoring Intermolecular Interactions for Efficient Room-Temperature Phosphorescence from Purely Organic Materials in Amorphous Polymer Matrices." *Angew. Chem. Int. Ed*. **2014**, 53, 11177-11181.
16. Hirata, S., "Recent Advances in Materials with Room Temperature Phosphorescence: Photophysics for Triplet Exciton Stabilization." *Adv. Opt. Mater.* **2017**, 5, 1700116
17. An, Z., Zheng, C., Tao, Y., Chen, R., Shi, H., Chen, T., Wang, Z., Li, H., Deng, R., Liu, X. and Huang, W., "Stabilizing triplet excited states for ultralong organic phosphorescence." *Nat. Mater*. **2015**, 14, 685-690
18. a) Luo, J., Xie, Z., Lam, J.W., Cheng, L., Chen, H., Qiu, C., Kwok, H.S., Zhan, X., Liu, Y., Zhu, D. and Tang, B.Z., "Aggregation-induced Emission of 1-methyl-1, 2, 3, 4, 5-Pentaphenylsilole." *Chem. Commun.* **2001**, 18, 1740-1741; b) An, B.K., Kwon, S.K., Jung, S.D. and Park, S.Y., "Enhanced Emission and its Switching in Fluorescent Organic Nanoparticles." *J. Am. Chem. Soc*. **2002**, 124, 14410-14415; c) Mei, J., Leung, N.L., Kwok, R.T., Lam, J.W. and Tang, B.Z., "Aggregation-induced Emission: Together We Shine, United We Soar!" *Chem. Rev.* **2015**, 115, 11718-11940
19. Pownall, H.J. and Granoth, I., "Internal Heavy Atom Studies on the Triplet State of Dimethyl- and Dihaloxanthones." *J. Phys. Chem.* **1976**, 80, 508-511
20. Kwon, M.S., Jordahl, J.H., Phillips, A.W., Chung, K., Lee, S., Gierschner, J., Lahann, J. and Kim, J.,"Multi-Luminescent Switching of Metal-free Organic Phosphors for

Luminometric Detection of Organic Solvents." *Chem. Sci*. **2016**, 7, 2359-2363

21. QY at 77 K was measured by Hamamatsu Photonics K.K.
22. Baldo, M.A., O'brien, D.F., You, Y., Shoustikov, A., Sibley, S., Thompson, M.E. and Forrest, S.R., "Highly Efficient Phosphorescent Emission from Organic Electroluminescent Devices." *Nature* **1998**, 395, 151-154
23. Horie, K., Morishita, K. and Mita, I., "Photochemistry in Polymer Solids. 3. Kinetics for Nonexponential Decay of Benzophenone Phosphorescence in Acrylic and Methacrylic Polymers." *Macromolecules* **1984**, 17, 1746-1750
24. Mieno, H., Kabe, R., Notsuka, N., Allendorf, M.D. and Adachi, C.,"Long-Lived Room-Temperature Phosphorescence of Coronene in Zeolitic Imidazolate Framework ZIF-8." *Adv. Opt. Mater.* **2016**, 4, 1015-1021.
25. We observed fluorescence of BrFL5 and 2-aminoterephthalic acid from BrFL6 in solution. Due to the overlap the between fluorescence from 2-aminoterephthalic acid as a chromophore and the phosphorescence of BrFL5, we cannot obtain the exact phosphorescence QY.

Chapter 3

Optimization of coupled plasmonic effects for viable phosphorescence of metal-free phosphor

Parts of this chapter appear in: Huan Wang[(+)], Jaehun Jung[(+)], Kyungwha Chung, Ju Won Lim, Youngmin You, Jinsang Kim[*], and Dong Ha Kim[*], *J. Appl. Phys*, **2017**, 122, 153103.

The main focus of this work is to improve brightness or efficiency of room temperature phosphorescence by using external agent, plasmonic nanometals. In the previous chapter, bright room temperature phosphorescence was achieved by suppressing vibration and was improved by the modification of molecular functionality. Although the intensity of room temperature phosphorescence is higher than (or equal to) that at 77K, the quantum yield is still around 50%. In order to further improve the brightness, a novel strategy to enhance the radiative decay process must be developed. Here, we proved the concept of plasmon-induced phosphorescence enhancement effect and explained how to optimize the condition to achieve enhanced phosphorescence.

3.1 Introduction

Phosphorescent materials have attracted much attention due to their potential applications in display devices, as well as chemical and biological detection.[1,2,3] However, most of the efficient phosphors reported to date are essentially inorganic or organometallic complexes.[4,5] It is difficult to achieve efficient phosphorescence from organic molecules at room temperature and ambient conditions. This is mainly because i) phosphorescence from metal-free phosphors is very sensitive to intermolecular vibration ii) their spin-orbit coupling is weak. Recent studies demonstrated that non radiative decay by intermolecular vibration can be deactivated via crystallization or a rigid polymer matrix.[6,7] In Chapter 2, activation of efficient phosphorescence from BrFL1 has been successfully demonstrated by means of doping BrFL1 in a PMMA film which has a higher activation temperature of intermolecular vibration than room temperature. In addition, it was shown that spin-orbit coupling of the fluorene derivatives can be controlled by modification of functional substitutes on the fluorene molecules. However, radiative decay constants are not much different, indicating that functional group modification cannot enhance spin-orbit coupling so much as if halides or heavy atom units are the same. To improve the brightness of phosphorescence from metal-free phosphors, a new strategy to enhance spin-orbit coupling or radiative decay process of phosphorescence is required.

Plasmon-mediated luminescence enhancement (fluorescence or phosphorescence) is a promising optical process that has attracted increasing attention over the past decade. This phenomenon is induced by the interaction between chromophores and localized surface plasmon resonance (LSPR) from adjacent metallic nanoparticles (NPs) via plasmon resonance energy transfer (PRET).[8-10] It was well studied that the plasmon resonance can increase the excitation rate due to a near-field enhancement of excitation and an increased fluorescence radiation rate of surface plasmon-coupled emission. When the plasmon frequency is matched to the excitation or the emission wavelength of emitters, both the photoluminescence (PL) intensity and quantum yield can be enhanced.[11-13] The enhanced luminescence reported to date were mainly focused on organic fluorophores, inorganic quantum dots, and low-dimensional nanomaterials.[14-20] Plasmon-induced phosphorescence enhancement (PPE) effect was also demonstrated in some organometallics and organic phosphors such as benzophenone in close proximity to suitable metallic NPs under cryogenic (e.g., 77 K) and inert conditions.[21-28] However, PPE with ambient-stability at room-

temperature has been rarely reported for metal-free phosphors.[29]

Here, we investigate whether PPE is also valid for employed Br6A/Br6 mixed crystals as metal-free phosphors with silver and gold NPs as a plasmonic nanoantenna at ambient conditions. We systematically investigated the PPE conditions; i) the distance between the plasmonic nanostructures and the phosphors was precisely controlled by using polyelectrolyte multilayers as a dielectric spacer ii) the plasmon frequency was tuned via controlling the size of and type of metallic NPs. The PPE mechanism was corroborated by dynamic PL study. This work represents a generally applicable strategy to enhance room temperature phosphorescence from metal-free organic phosphors.

3.2 Background knowledge

3.2.1 Surface plasmons

Surface plasomns (SPs) are coherent delocalized free electron oscillations that exist at the interface between any two materials. The key component of plasmonic is a metal, because it supports surface plasmon polariton modes. When the nanostructure of metals is smaller than or comparable to the wavelength of light, the free surface electrons can oscillate in resonance with the light at a certain excitation frequency. This is known as a localized surface plasmon resonance (LSPR) which is the result of the confinement of surface plasmons.

The localized surface Plasmon (LSP) has two important effects. First, the electric fields from oscillation of free electrons near the partcle's surface are greatly enhanced (Fig 3.1). The field is highly localized at the nanoparticle and falls off quickly away from the nanoparicle into the dielectric background. Because of the enhanced field amplitude, amplification of a magneto-optical effect such as plasmons enhanced fluorescence is also feasible by LSPRs. Second, the particle's optical absorption has a maximum at the plasmon resonant frequency. The density of free electrons on a metal particle surface changs depending on the size of the metal particle. When the oscillation frequency of free electrons is matched to the wavelength of light, the free electrons can oscillate in resonance with the light. As the size of metal the nanoparticle increases, the density of free electrons on the metal nanoparticle surface also changes and the charge separation increases, which leads to a lower frequency of the oscillation of free electrons and a red-shift for the absorption maximum of nanoparticles. As seen in Figure 3.2, with the increasing size of au nanopaticles, the absorption spectra are red-shifted. Therefore, the plasmon resonance frequency can be

controlled by the size of nanopaticles.

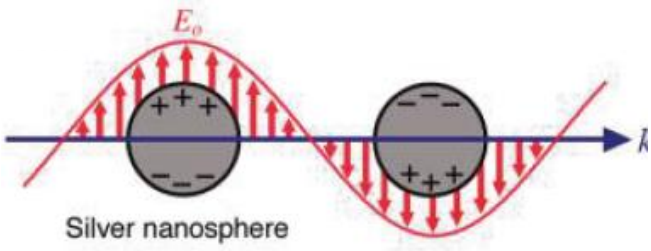

Figure 3.1 Schematic illustration of localized surface plasmons resonance as excited the electric field of incident light with wavevector. Image from Chem. Rev. 2011, 111, 3669–3712.

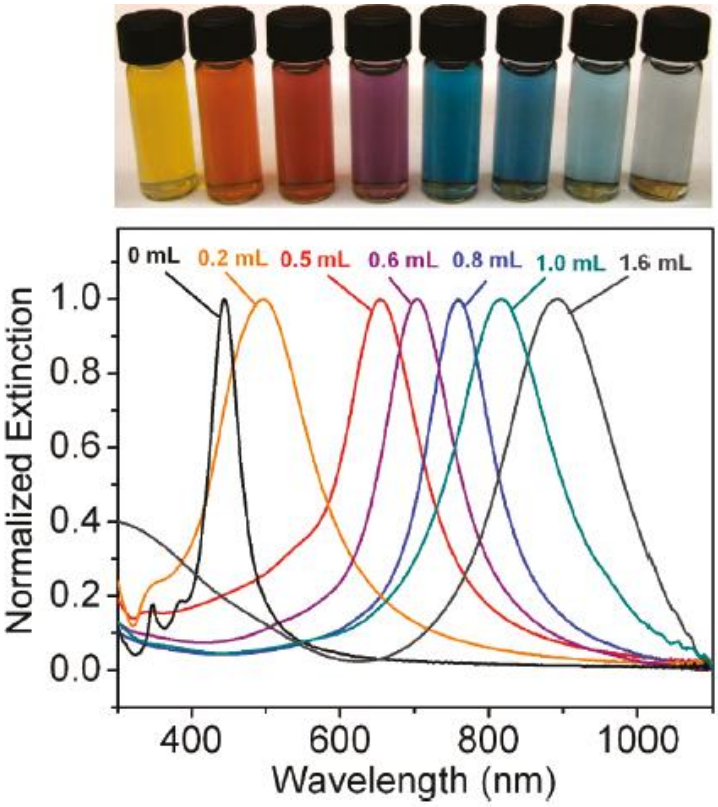

Figure 3.2 Image of Nanoparticles and their UV-vis spectra. Vials-containing Au nanoboxes and nanocages (top) and corresponding UV-vis spectra of Ag nanocubes/nanocages (bottom). Image from Nat. Protoc. 2007, 2, 2182.

3.2.2 Interaction of fluorophores with surface plasmons

The enhanced field amplitude by the coupling of light with LSP can interact with fluorophores at their absorption maximum, λ_{ab}, and emission maximum, λ_{em}, wavelength. One way to explain the arisen enhancement is the Purcell effects. The Purcell effect is the enhancement of fluorescent molecules' spontaneous excitation and emission which is followed by Femi's golden rule.[30] The density of final state is associated with the plasmon-enhanced field intensity. Within a smaller distance between fluorphores and plasmonic particles, the density of the final state increases and then the intensity of absorption or emission of fluophores is further enhanced because of a strongly enhanced electric field by LSP. However, within a very short distance from the metal surface (<3nm), strong quenching of radiative transitions occurs due to the electron transfer from a fluorophore to a metal, leading to an enhanced non-radiative decay rate of fluorophores. This quenching is dominant against the enhancement of the absorption or emission for a very short distance. Therefore, the quantum yield of fluorophores decreases for this very short spacing. For a little longer distance, the emission enhancement becomes dominant and consequently the quantum yield increases. For a too long distance, the enhanced field cannot reach the fluorophore and the direct electron transfer cannot occur either. As Figure 3.3b illustrates, at a certain distance between a fluorophores and a metal, the quantum yield of the fluorophore becomes maximum because the offset of the electron transfer quenching and the enhancement by LSP is optimized.

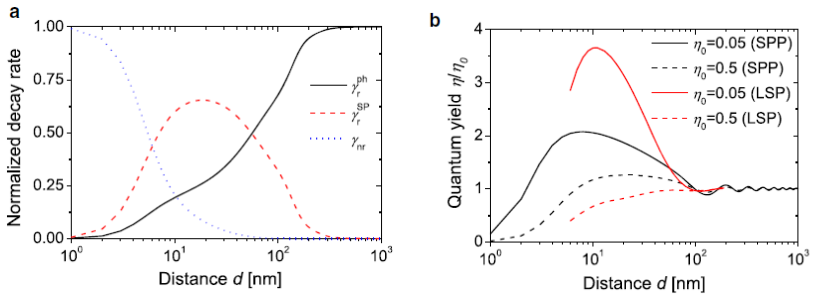

Figure 3.3 (a) Simulated radiative rate γ_r(associated with emission to far field γ_r^{ph} and via surface plasmons γ_r^{sp}) and nonradiative rate γ_r^{nr}. (b) Respective changes in a quantum yield n for a fluorophore with low n_0=0.05 and high n_0=0.5 intrincsic quantum yield. The rate were normalized by the total decay rate $\gamma_r + \gamma_r^{nr} + \gamma_r^{sp}$. A flat gold surface supporting surface propagating plasmons (SPPs) and gold disk nanoparticle with a diameter of 100nm and height of 50nm supporting LSP were assumed. Image from Plasmonic 2014, 9, 781.

3.3 Experiments

3.3.1 Synthesis of AuNP (~55 nm) and AgNP (~7 and ~70 nm)

The nanoparticle synthesis was conducted by our collaborator, Dr. Huan Wang at Ewha Womans University. For the synthesis of AuNPs, a solution of 198 mL of deionized water and 2 mL of 1 wt% Gold(III) chloride hydrate ($HAuCl_4 \cdot 3H_2O$, Aldrich, 99.999%) was heated at 130 ℃ under vigorous stirring. An 1.4 mL of 1 wt% sodium citrate (Aldrich, 99%) aqueous solution (~10 mg/mL) was then rapidly added, and the solution was boiled for additional 30 min under continuous stirring. The AuNPs displayed a hot pink coloration with an around 55 nm diameter. For the synthesis of smaller AgNPs (~7 nm), both sodium borohydride ($NaBH_4$, Aldrich, 99%) and sodium citrate as the reductants were employed. 3 mg $NaBH_4$ and 12 mg sodium citrate were dissolved in 148 mL of deionized water. The mixture was heated at 60 ℃ for 30 min in the dark with vigorous stirring. 2 mL of 23.5 mM silver nitrate ($AgNO_3$, Aldrich, >99.8%) solution was then added drop-wise to the mixture and the temperature was raised to 90 ℃. The pH of the solution was adjusted to 10.5 using 0.1 M NaOH while heating was continued for 20 min, until the color of the solution was changed to yellow. The diameter of AgNPs was ~7 nm. For the synthesis of larger AgNPs (~70 nm), sodium citrate as the only reductant was employed. 7 mg $AgNO_3$ was dissolved in 150 mL of deionized water and the mixture was heated to its boiling temperature. Then, a 3 mL of 1 wt% sodium citrate aqueous solution was added to the boiling solution, and boiling was maintained for 1 h, yielding ~70 nm diameter AgNPs. Figures 3.4 (a)-(c) show higher resolution SEM images of the synthesized metallic NPs, and the average diameter and the size distribution of the NPs are shown in (d).

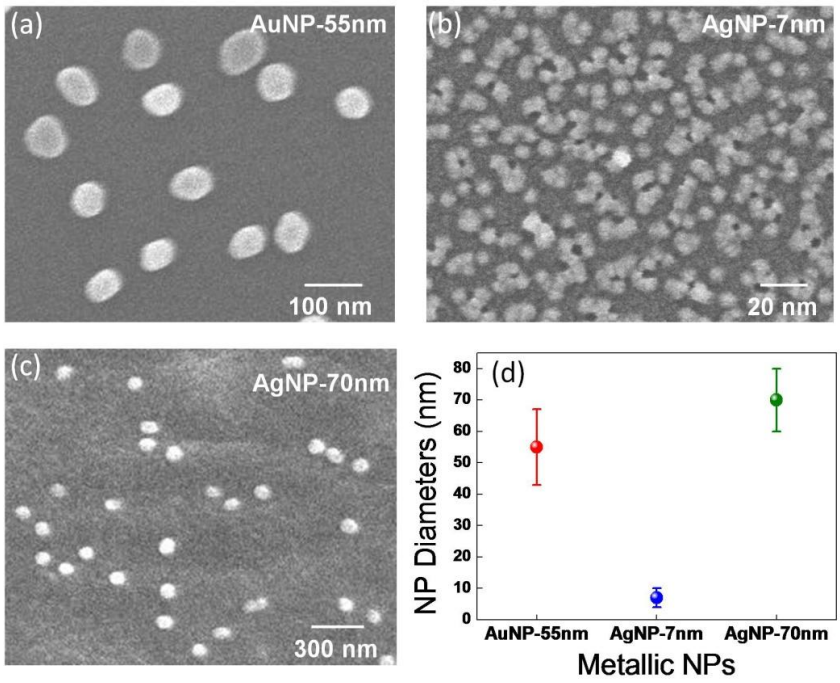

Figure 3.4 SEM images of the synthesized (a) ~55 nm AuNPs , (b) ~7 nm AgNPs ,(c) ~70 nm AgNPs. (d) The average diameter and size distribution of the NPs.

3.3.2 Fabrication of plasmon-mediated Br6A/Br6 crystals

Br6A and Br6 were synthesized referring to the previous report.[6] 1 wt% mixture of Br6A to Br6 in hexane solution at the concentration of 5 mg/mL was spin-coated (2000 rpm) on a clean glass substrate for the pristine crystal preparation. PAH with average Mw of ~17,500 g/mol and PSS with average Mw of ~70,000 g/mol were purchased from Sigma-Aldrich, and were dissolved in a 3.3 mM sodium chloride (NaCl) solution, repectively, to the concentration of 0.5 mg/mL before use. Polyelectrolyte multilayers of positively charged PAH and negatively charged PSS were assembled alternatively for 5 min through the immersion-based layer-by-layer self-assembly procedure. After each step (PAH or PSS), the sample was rinsed with ultrapure deionized water. The process was repeated to obtain desired numbers of polyelectrolyte multilayers. A PAH layer was coated at the outermost surface to promote the adhesion of the negatively charged citrate-passivated AuNPs or AgNPs.

3.3.3 Characterization techniques

The wide-angle XRD data were obtained with a Rigaku X-ray diffractometer (D/Max-rA, using Cu-Kα radiation of wavelength 1.542 Å). Absorbance was measured using an Agilent

Cary 5000 UV-Vis-NIR spectrometer. Surface morphologies were analyzed using AFM in tapping mode (Digital Instrument Dimension 3100 scanning force microscope) and scanning electron microscopy (SEM; JEOL JSM6700-F). SPR spectroscopy measurements (Resonant Technologies GmbH/RT2005 SPR spectrometer) were carried out using *p*-polarized laser light (He−Ne, 632.8 nm, 10 mW) illuminating the Au film through the LaSFN9 prism. Calculation of PSS/PAH thickness was carried out using Winspall software (RES-TEC, Germany) with the complex refractive index and dielectric constant values of 1.45 and 2.0125, respectively. It was assumed that PAH and PSS have the same values of optical constants. FDTD simulation was carried out using Lumerical Solution software. The mesh size was set at 0.5 nm for the elaborate design. The plane wave source was used as incident light. *z* and *x* were considered to be the light incident direction and the polarization direction, respectively. PL spectra were obtained using a Photon Technologies International (PTI), QuantaMaster 400 scanning spectrofluorimeter at 298 K. Phosphorescent lifetime data were collected using a PTI LaserStrobe and the calculations were carried out on the FeliX32 software partnered with the PTI equipment.

3.4 Results and discussion

Br6A and Br6 are room temperature phosphorescent molecules referring to the previous report.[6] Fast grown or noncrystsalline power of BrA can exhibit relatively stronger fluorecent emission because the power has less tight halogen bonding, leading to vibrational loss of triplet excitons and consequent inefficient phosphorescent emission. Strong halogen bond formation between the aldehyde and the bromine of Br6A in the crysalline state suppresses vibration as well as turns on the halogen-associated heavy atom effect. The unprecedented synergy makes the triplet generration more efficient, which suppresses fluorescence, and consequently phosphorescence is largely enhanced by strong spin-orbit coupling and vibration suppression due to the halogen bonding.[6] It has been demonstrated that Br6A doped into the host Br6 crystal can emit much more efficient phosphorescence by preventing the aggregation-induced quenching among Br6A molecules. We prepared 1 wt% Br6A doped Br6 crystal as chromophore and combined it to different plasmonic nanometals in order to invesitgate the PPE system. The excitation and phosphorescence spectra of Br6A/Br6 doped crystal and the fluorescence spectrum of Br6A in a chloroform solution are shown in Figure 3.5(b), corresondping to the wavelength of 385, 520 and 420nm, respectively. Figure 3.5(c)

illustrates the schematic models of LSPR field enhancement effects on the luminescence enhancement in term of the spectral proximity. Size controlled metal nanoparticles (AgNPs ~7nm, AgNPs ~70nm and AuNPs ~55nm) have been prepared, in which their LSPR bands have a substantial overlap with the excitation, fluorescence and phosphorescence wavelengths of Br6A, respectively, to investigate the amplification of phosphorescence via LSPR.

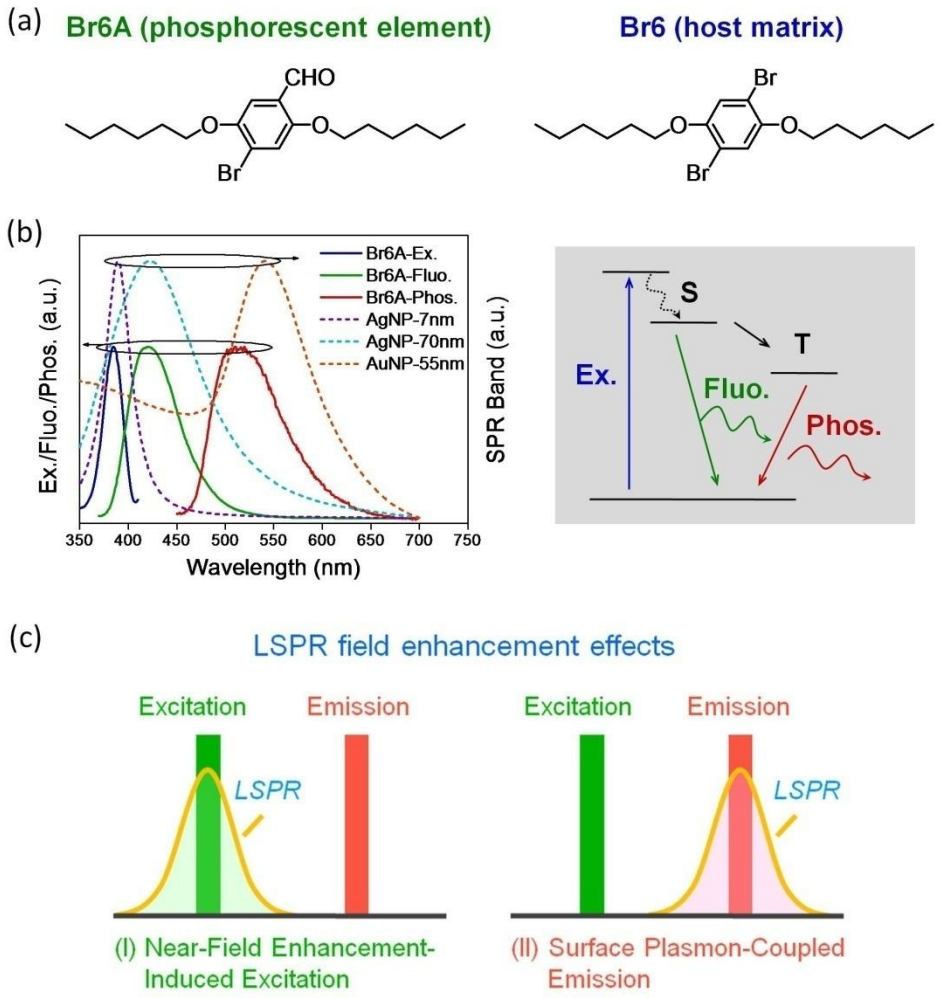

Figure 3.5 (a) Molecular structures of Br6A and Br6. (b) LSPR bands of AgNP with ~7 and ~70 nm diameter, and AuNP with ~55 nm diameter; excitation, fluorescence and phosphorescence wavelengths of the chromophore.[8] (c) Schematic models representing LSPR field enhancement effects on the luminescence enhancement. Near-field enhancement-induced excitation (I) and surface plasmon-coupled emission (II) can be realized by matching the LSPR band with the excitation and emission wavelength of the organic crystals, respectively.

The samples consist of three layers; Br6A/Br6 doped crystals as chromophore, thickness-controlled polyeletrolte multilayers as the spacer, and metal nanoparticles as plasmonics. (Fig. 3.6). The initially formed doped crystal layer was prepared by spin-coating the Br6A/Br6 misture in a solution on the glass substrate (Step 1 in Figure 3.6a). The crystal domain size was around ~3μm and the film thickness was ~600nm that is much thicker than the thickness of the spacer layer. To reduce the thickness of the crystal layer and spread the crystals on the substrate more uniformly so as to achieve more consistent and sensitive plasmonic effect, the pristine doped crystal film was melt by heating at 70^{o}C and recrystallized by slow cooling, which gave a thin Br6A/Br6 doped crystal layer having a larger domain size at around 20μm and the thickness of ~90nm (Step II). In the next step III, polyelectrolyte multilayers of positively charged PAH and negatively charged PSS were alternatingly deposited on the crystal. Finally, metallic NPs were dip-coated on top of the polyelectrolyte layers (Step IV). By using this well-defined organic phosphors/dielectric spacer/metallic nanoparticle tri-layer platform, the effects of the distance between phosphors and plasmonic nanometals and the spectral overlap on PPE efficiency were systematically investigated. The dark field images of the pristine crystal and ~55 nm AuNPs-decorated crystals with a spacer thickness of ~1.6 and ~9.6 nm, respectively, clearly show the distance-dependent emission amplification (Step V).

The thickness of the alternating polyelectrolyte multilayers of PAH and PSS was measured by surface plasmon resonance (SPR) spectroscopy. SPR is a unique optical phenomenon observed when polarized light strikes at the metal-dielectric interface in a nanoscale dimension. The resonance band position depends on various parameters including the type of metal, thickness and refractive index of the dielectric medium in contact with the metal, etc. The thickness of the polyelectrolyte multilayers was evaluated by means of the same strategy reported in the literature.[31,32] As seen in Figure 3.6(b), the SPR angle shifted progressively to a higher incident angle with the increasing number of alternating polyelectrolyte layers from a single layer to 16 multilayers. The increased surface roughness by increasing the number of polyelectrolyte layers induces light scattering, leading to the curve broadening and increase in the reflectiveness. To obtain the thickness value from the SPR data, we conducted a simulation by using Winspall software and evaluated the linear correlation between the number of the layers and thickness of the film as shown in Figure 3.6(c). The average thickness of each layer is estimated to be about 1.6nm. We also measure the thickness of the intentionally scratched film by using a cross-sectional AFM image. The

AFM height profile shows that the thickness of 8-multilayer is around 12.2nm (Fig 3.7), which is in good agreement with the calculated thickness of 8-multilayer (12.8nm) from the SPR method.

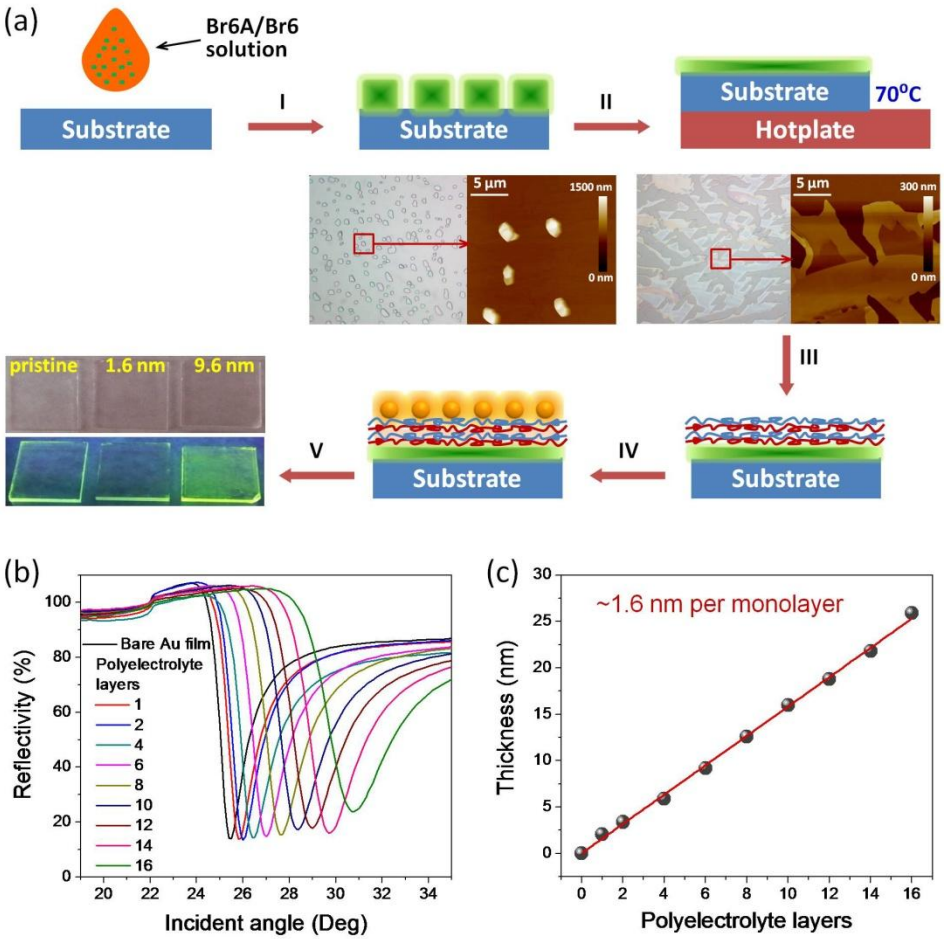

Figure 3.6 (a) Schematic illustration of the entire procedure to fabricate plasmon-mediated Br6A/Br6 crystal samples: I. Thicker and smaller crystals prepared by spin-coating (The crystal size is ~3 µm with ~600 nm thickness); II. Thinner and larger crystal formed by heating (The crystal size is larger than 20 µm with ~90 nm thickness); III. Alternate layer-by-layer self-assembly of polyelectrolyte multilayers; IV. Deposition of metallic NPs by electrostatic interaction; V. Photographs of pristine crystal and ~55 nm AuNPs-decorated crystals with two different thickness of polyelectrolyte layers (~1.6 and ~9.6 nm) under normal room light and 365 nm ultraviolet light, respectively. (b) Static scan-mode SPR spectroscopy profile monitoring the stepwise deposition of PSS and PAH polyelectrolyte multilayers on a bare Au film coated on the glass substrate. (c) The calculated film thickness as a function of the number of polyelectrolyte layers. The average thickness of each layer was estimated to be ~1.6 nm.

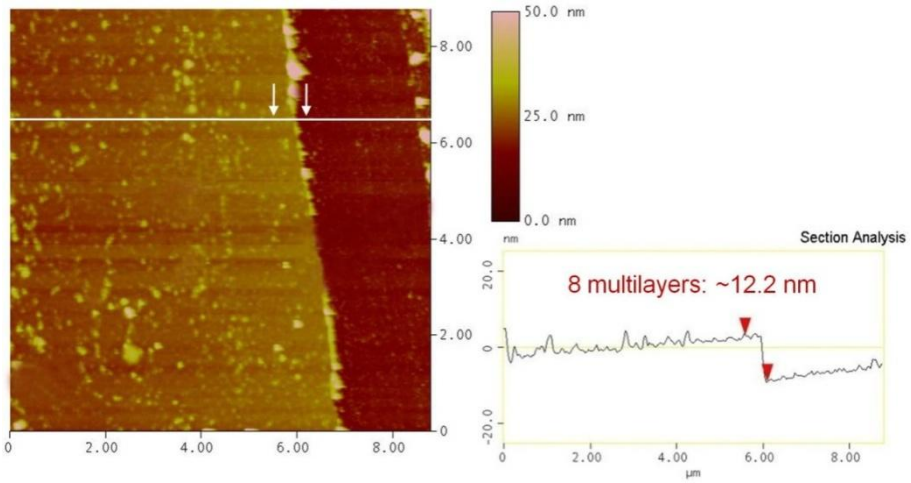

Figure 3.7 Height-contrast AFM image for the 8 multilayers of alternating PSS and PAH with ~12.2 nm thickness.

We controlled the dipping time of the substrate in the prepared plasmonic nanometal suspensions in order to find out the optimization amount of metallic NPs deposited on the surface of the polyelectrolyte multilayer. AuNPs and AgNPs adhere to the PAH layers at the surface of the polyelectrolyte multilayer because of the Coulombic interaction between negative surface charges of the NPs and positively charged PAH layer. The surface density of AuNPs on the film increased as the dipping time became longer. The Figure 3.8(i) is SEM images showing the distribution of ~55nm AuNPs with various dipping times. The absorption intensity of AuNPs (or LSPR band) at 540nm increases proportionally with the AuNPs density. The distribution and corresponding absorbance of the ~7 and ~70nm AgNPs are also shown in Figure 3.8(ii) and (iii).

LSPR effects on phosphorescence was first studied with various thicknesses of polyelectrolyte multilayers on the premise of optimal density for each metallic NPs. Fig 3.9(b) shows PL spectra of Br6A/Br6 doped crystal with AuNPs, which have substantial overlap of their LSPR bands with the phosphorescence wavelengths, separated by ~1.6, 3.2, 6.4, 9.6, 12.8, 16.0 and 19.2nm spacing (corresponding to 1, 2, 4, 6, 8, 10, and 12 polyelectrolyte multilayers), respectively. At a short distance, the phosphorescence of the plasmon-mediated Br6A/Br6 crystals was quenched. The phosphorescence intensity gradually increased with the increasing thickness of the polyelectroyte layer and the maximum phosphorescence intensity was observed from the sample with a ~9.6 nm spacing. The phosphorescence intensity decreases as the polyelectrolyte thickness further increases. When the polyelectrolyte

thickness was close to ~20nm, the PL intensity is almost identical to that of the pristine Br6A/Br6 crystals on a bare glass substrate as a reference (Figure 3.9(b)), implying that LSPR could not significantly influence on phosphors because the distance between phosphors and plasmonics are too far. The maximum enhancement of the phosphorescence emission by the AuNPs was up to 2.8 times (Table 3.2). The PL spectrum from Br6A/Br6 doped crystal with ~7nm and ~70 nm AgNPs that have substantial overlap of their LSPR bands with the excitation and fluorescence wavelength of the doped crystal, respectively, show the same trend of the PL intensity with ~55nm AuNPs. The maximum enhancement for the ~7nm and ~70nm AgNPs were up to 2.5 and 1.8 times, respectively. It is notable that quenching of PL intensity was observed at a very short distance (<3nm) between phosphors and plasmonic nanometals because of direct energy transfer (DET) and the existence of electron traps at the metallic surfaces.[15, 33] Metal-induced quenching is much dominant to the LSPR field enhancement at the very short distance and the maximum PL enhancement was observed when LSPR field enhancement overwhelms at a certain distance. Therefore, the competition between LSPR field enhancement and the metal-induced quenching is the crucial factor in the distance-dependent PPE phenomenon. More detailed PPE mechanism is discussed in the following section.

To find out the optimized density of NPs, different surface densities of ~55nm AuNPs were fabricated with a fixed thickness of ~9.6nm polyelectrolyte multilayers. Compared to the pristine sample without AuNPs, all plasmon-meditated samples exhibit phosphorescence enhancement (Figure 3.9(f)). The enhancement of PL intensity gradually increased with the surface density of AuNPs initially but slightly decreased after reaching the maximum point (Figure 3.9(e)). It was not clear that the phosphorescence enhancement is not fully linear with through the entire range of AuNPs amount but the reason might be related to a slight degradation of the sample when the sample immersed into the nano-suspension for a longer time or increased non-radiative decay via energy transfer from phosphors to AuNPs competing with LSPR field enhancement effect.[10,34,35] The trend in the phosphorescence enhancement of the ~7nm and ~70nm AgNPs samples with different surface densities was similar to that of AuNPs samples. It was found that the optimal density for the maximum PPE is ~45/μm^2 for AuNPs, 1,100/μm^2 for ~7nm AgNPs, and 39/μm^2 for ~70nm AgNPs, respectively.

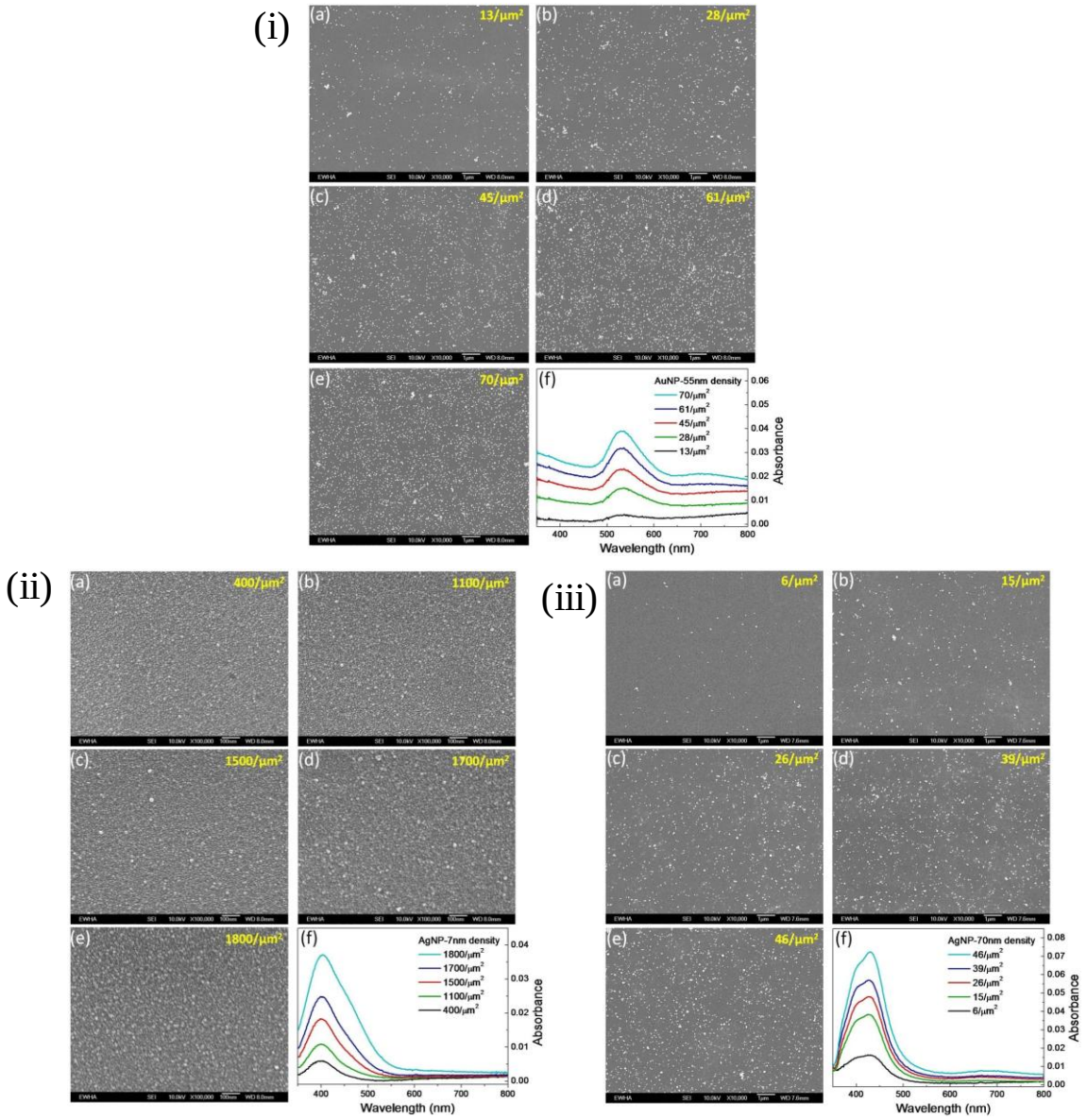

Figure 3.8 SEM images(a-e) of the dispersed (i) AuNPs of ~55 nm size,(ii) AgNPs of ~7nm size,(iii) AgNPs of ~70nm size and the corresponding absorbance profiles (f) adhered on the substrate with different density by controlling the dipping time of 15, 45, 60, 90 and 120 min, respectively.

The phosphorescence lifetimes were measured for Br6A/Br6 doped crystal deposited with ~55nm AuNPs, ~7nm and 70nm AgNPs separated by the differing thickness of polyelectrolyte layers, respectively (Figure 3.10(a)-(c)). The lifetime obtained by fitting the decay curves is summarized in Figure 3.10(d). The lifetimes were measured to be ~7.49 (±0.39), 7.65 (±0.44), and 7.24 (±0.45) ms for the samples decorated with ~55nm AuNPs,

~7nm AgNPs, or ~70nm AgNPs, respectively, at the short distance (~1.6nm) between the phosphorescent crystal and plasmonic nanaparticles. The lifetimes were shorter than that of the pristine crystal which showed the longest lifetime up to ~8.08 (±0.41) ms. The phosphorescent quenching and the shorter lifetime imply that non-radiative process are activated by electron transfers. When the phosphorescence enhancement was maximum at the spacing of ~9.6nm, the lifetime of the same sample was measured to ~7.36 (±0.47), 7.99 (±0.38), and 7.37 (±0.31) ms, respectively. The enhanced phosphorescence intensity combined with the shorter lifetime than those of the pristine crystal can be contributed to LSPR field enhancement effects amplifying excitation or accelerating radiation rate.[20,36] It is noted that the crystal samples with ~7nm AgNPs should show enhanced phosphorescence due to the amplification of excitation without accelerating the phosphorescence radiation rate because the LSPR band of ~7nm AgNPs overlaps with the excitation spectrum of the phosphors. As expected, the crystal samples with ~7nm AgNPs exhibited an enhanced phosphorescence intensity with a similar phosphorescent lifetime compared to that of the pristine crystal. Because the broad LSPR band of ~70nm AgNPs only partially overlaps with the phosphorescence spectrum, the phosphorescence enhancement with a shorter lifetime was also observed from the crystal sample with ~70nm AgNPs. At the polyelectrolyte spacer thickness of ~19.2 nm, the phosphorescence lifetime was ~8.01 (±0.38), 8.06 (±0.33), and 8.05 (±0.32) ms that are closed to the lifetime of the pristine crystal, reflecting the dimished plasmonic effect. The PL lifetime of the above samples are summarized in Table 3.1.

The previous studies for other molecular systems[15,26,32] reported that the direct electron transfer (DET) from the crystal to the NPs causes to drastic PL quenching when chromophore are very close to plasmonic nanometals (<3nm). Besides the DET, electron from exciton in the crystal can tunnel to and be trapped in the NPs, leading to nonradiative recombination with remaining holes at the semiconductor-metal interface due to the existence of trap states at the metallic surfaces. Therefore, these factors can cause metal-induced luminescence quenching at the short distance between phosphors crystals and plasmonic nanometals (Figure 3.10(e)). With an increasing thickness of polyelctrolyte layers, metal-induced quenching becomes drastically diminished and LSPR field enhancement effect on PPE becomes dominant (Figure 3.10(f)). For examples, LSPR accelerates the phosphorescence radiation rate of the sample with ~55nm AuNPs, leading to the enhancement of phosphorescence intensity because the LSPR bands overlap with the phosphorescence

spectrum. When it comes to the ~7nm AgNPs whose LSPR band overlaps with the excitation spectrum of the phosphors crystal, the near-field enhancement-induced excitation amplified the excitation, resulting in an increase in the absorption and emission intensity. Figure 3.10(g) describes the light-emitting profile dictated by the two competing processes depending on the plasmon-crystal distance. At a certain distance between nanometals and phosphor crystals (~9.6nm), the maximum phosphorescence enhancement was observed. If the crystal is too far from NPs, PPE is either diminished because the weak electromagnetic field from the metal surface cannot reach the chromophore.

Table 3.1 Summary of different plasmon-mediated phosphorescent Br6A/Br6 crystals (from Figure 3). The average value of PL intensity of pristine crystal is 0.62×10^5, and the maximum enhancement of the PL intensity for each plasmon-mediated sample occurred when the polyelectrolyte thickness was around 9.6 nm

	~55 nm AuNP	~7 nm AgNP	~70 nm AgNP
Max. PL intensity ($\times 10^5$)	1.71	1.55	1.10
Max. enhancement	2.8 times	2.5 times	1.8 times

The previous studies for other molecular systems[15,26,32] reported that the direct electron transfer (DET) from the crystal to the NPs causes to drastic PL quenching when chromophore are very close to plasmonic nanometals (<3nm). Besides the DET, electron from exciton in the crystal can tunnel to and be trapped in the NPs, leading to nonradiative recombination with remaining holes at the semiconductor-metal interface due to the existence of trap states at the metallic surfaces. Therefore, these factors can cause metal-induced luminescence quenching at the short distance between phosphors crystals and plasmonic nanometals (Figure 3.10(e)). With an increasing thickness of polyelctrolyte layers, metal-induced quenching becomes drastically diminished and LSPR field enhancement effect on PPE becomes dominant (Figure 3.10(f)). For examples, LSPR accelerates the phosphorescence radiation rate of the sample with ~55nm AuNPs, leading to the enhancement of phosphorescence intensity because the LSPR bands overlap with the phosphorescence spectrum. When it comes to the ~7nm AgNPs whose LSPR band overlaps with the excitation

spectrum of the phosphors crystal, the near-field enhancement-induced excitation amplified the excitation, resulting in an increase in the absorption and emission intensity. Figure 3.10(g) describes the light-emitting profile dictated by the two competing processes depending on the plasmon-crystal distance. At a certain distance between nanometals and phosphor crystals (~9.6nm), the maximum phosphorescence enhancement was observed. If the crystal is too far from NPs, PPE is either diminished because the weak electromagnetic field from the metal surface cannot reach the chromophore.

The previous studies for other molecular systems[15,26,32] reported that the direct electron transfer (DET) from the crystal to the NPs causes to drastic PL quenching when chromophore are very close to plasmonic nanometals (<3nm). Besides the DET, electron from exciton in the crystal can tunnel to and be trapped in the NPs, leading to nonradiative recombination with remaining holes at the semiconductor-metal interface due to the existence of trap states at the metallic surfaces. Therefore, these factors can cause metal-induced luminescence quenching at the short distance between phosphors crystals and plasmonic nanometals (Figure 3.10(e)). With an increasing thickness of polyelctrolyte layers, metal-induced quenching becomes drastically diminished and LSPR field enhancement effect on PPE becomes dominant (Figure 3.10(f)). For examples, LSPR accelerates the phosphorescence radiation rate of the sample with ~55nm AuNPs, leading to the enhancement of phosphorescence intensity because the LSPR bands overlap with the phosphorescence spectrum. When it comes to the ~7nm AgNPs whose LSPR band overlaps with the excitation spectrum of the phosphors crystal, the near-field enhancement-induced excitation amplified the excitation, resulting in an increase in the absorption and emission intensity. Figure 3.10(g) describes the light-emitting profile dictated by the two competing processes depending on the plasmon-crystal distance. At a certain distance between nanometals and phosphor crystals (~9.6nm), the maximum phosphorescence enhancement was observed. If the crystal is too far from NPs, PPE is either diminished because the weak electromagnetic field from the metal surface cannot reach the chromophore.

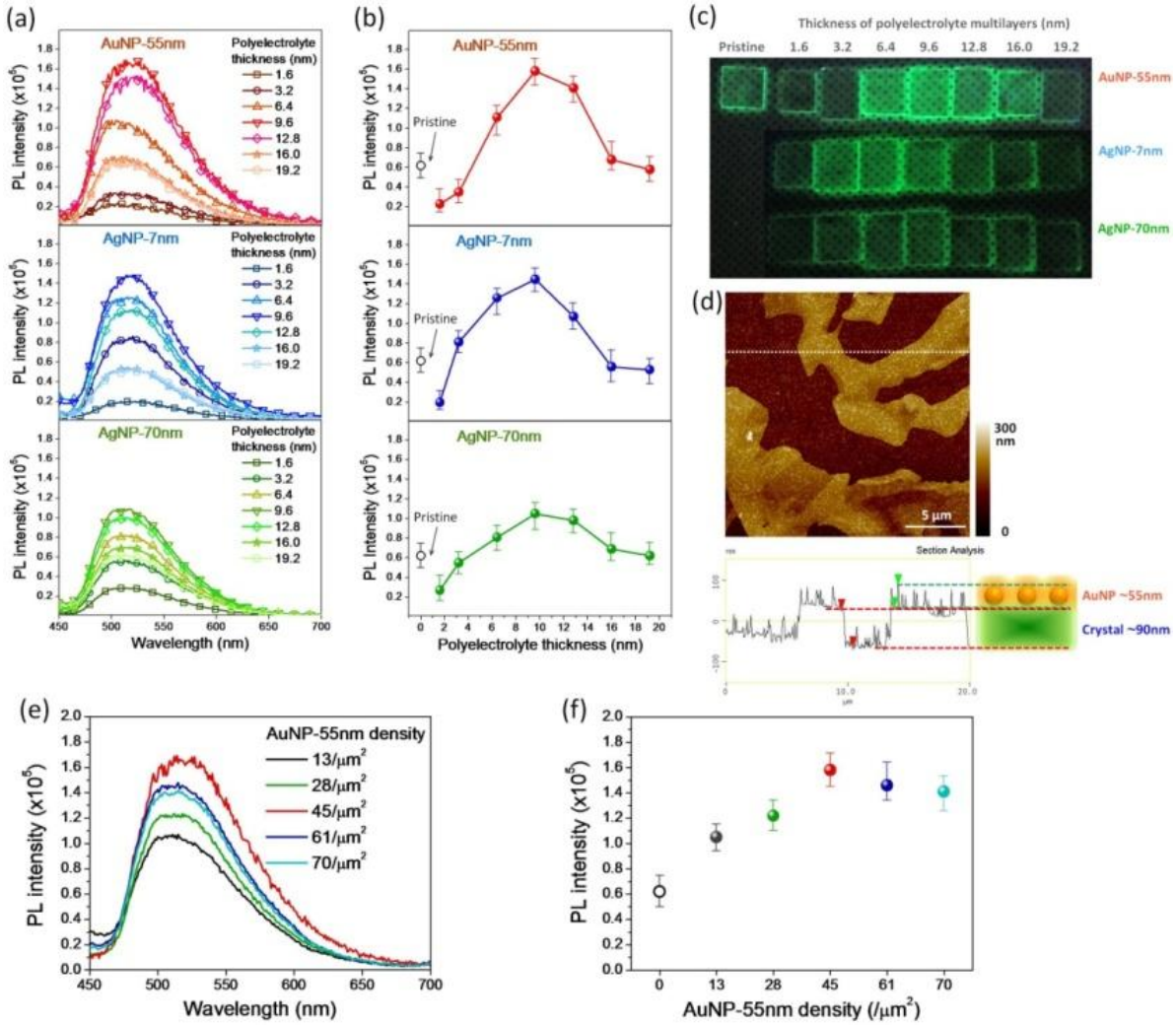

Figure 3.9 (a) PL spectra of different plasmon-mediated phosphorescent Br6A/Br6 crystals with different thickness of polyelectrolyte multilayer spacers (from 1.6 to 19.2 nm). (b) Statistical comparison (over 10 samples for each case) of PL intensity described in (a). (c) Photographs of pristine crystal, and the ones decorated with ~55 nm AuNPs, ~7 nm AgNPs and ~70 nm AgNPs with different thickness of polyelectrolyte multilayers under 365 nm ultraviolet light. (d) AFM morphology of ~55 nm AuNPs-decorated crystal film. From the section analysis, the height of AuNPs nanostructure constructed on the crystals was measured to be around 55 nm and the crystal thickness is around 90 nm. (e) PL spectra of plasmon-mediated phosphorescent Br6A/Br6 crystals with different density of ~55 nm AuNPs by controlling the dipping time. (f) Statistical comparison (over 10 samples for each case) of PL intensity described in (e). For all samples, the polyelectrolyte thickness was adjusted to ~9.6 nm (6 multilayers).

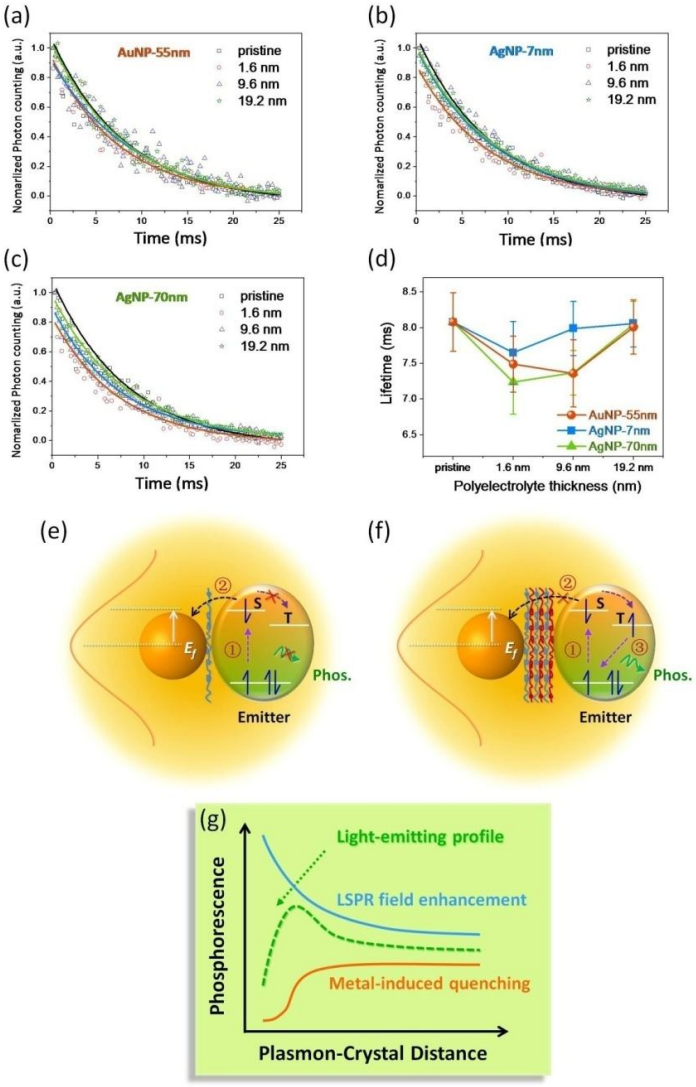

Figure 3.10 PL decay curves of different plasmon-mediated phosphorescent Br6A/Br6 crystals (pristine crystal as the reference) monitoring the 520 nm emission under 380 nm excitation for various thicknesses of polyelectrolyte multilayer spacers: (a) ~55 nm AuNPs; (b) ~7 nm AgNPs; (c) ~70 nm AgNPs. (d) Fitted lifetime comparison of above samples. The schematic mechanism of quenched and enhanced phosphorescence: (e) Metal-induced quenching is dominant when the distance between plasmonic nanometal and emitter is short, causing a quenching of PL; (f) LSPR field enhancement is dominant when the distance between plasmonic nanometal and emitter is optimized, leading to an enhancement of PL. (g) Schematic diagram of the emission distribution varying with the distance between plasmonic nanometals and phosphor crystals by the combined influence of metal-induced quenching and LSPR field enhancement. Process ①, ② and ③ represent the excitation, metal-induced quenching and radiation, respectively.

Table 3.2 Summary of PL lifetime of different plasmon-mediated Br6A/Br6 crystals with different thickness of polyelectrolyte layers

Thickness of polyelectrolyte layers (nm)	~55 nm AuNP		~7 nm AgNP		~70 nm AgNP	
	Lifetime (ms)	Error (ms)	Lifetime (ms)	Error (ms)	Lifetime (ms)	Error (ms)
Pristine (Ref.)	8.08	0.41	8.08	0.41	8.08	0.41
1.6	7.49	0.39	7.65	0.44	7.24	0.45
9.6	7.36	0.47	7.99	0.38	7.37	0.31
19.2	8.01	0.38	8.06	0.33	8.05	0.32

The localized surface plasmons can give the enhanced near-field amplitude at the resonance wavelength which matches with the coherent oscillations of electron confined to a small region. The electromagnetic field generated by the oscillation is highly localized around the plasmonic nanometal and decays rapidly away from the interface of NPs into the dielectric background. Finite-difference time-domain (FDTD) simulations were employed to estimate the LSPR field enhancement at the surface of plasmonic nanometals used in this study. The electric field intensity around AgNP is higher than that of AuNP for 380nm excitation, indicating more effective near field enhancement-induced excitation because the AgNPs LSPR band overlaps much with the excitation maximum (around 380nm) of Br6A/Br6 crystal (Figure 3.11). Upon excitation at 520nm, the electric field intensity is much higher for the AuNPs which favors surface plasmon-coupled emission because of the spectral overlap between the AuNPs LSPR band and the phosphorescence emission.

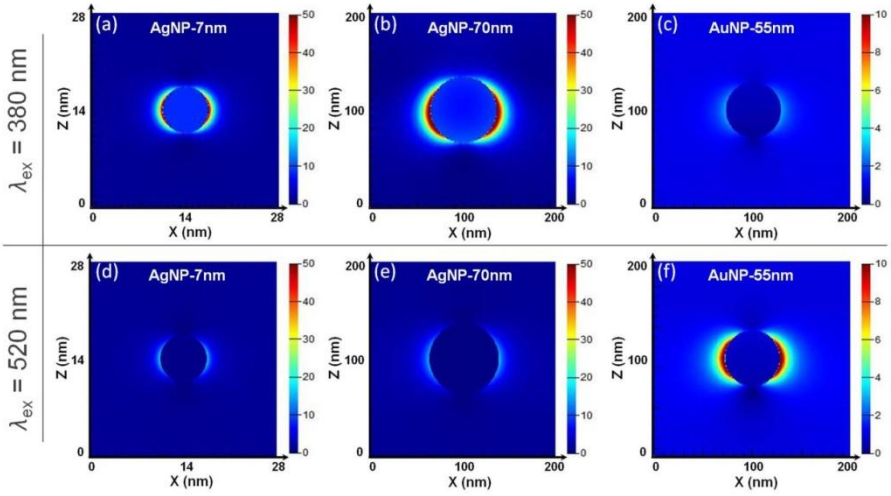

Figure 3.11 Electric field distributions around AgNP (7 & 70 nm) and AuNP (55 nm) at λ_{ex} = 380 nm (a-c) and λ_{ex} = 520 nm (d-f), respectively, obtained from FDTD simulations.

3.5 Conclusion

In summary, we studies distance-dependent enhancement of phosphorescence from metal-free phosphor Br6A/Br6 doped crystal combined with plasmonic nanometals. The distance was controlled by using layer-by-layer assembled polyelectrolyte multilayers as a dielectric spacer. Up to 2.8 times enhancement in phosphorescence intensity was obtained from the crystal samples with ~9.6nm spacer and deposited NPs. This is attributed to the substantial spectral overlap of the excitation or phosphorescence of Br6A/Br6 crystal with the LSPR bands of NPs, which can accelerate the phosphorescence radiation rate or amplify the absorption as evidenced by the time-resolved PL measurements. The drastic decrease in the phosphorescence intensity was also observed at a very short distance between phosphor crystals and plasmonic nanometals due to the metal-induced quenching by direct electron injection. Hence, the distance-dependent plasmon-induced phosphorescence enhancement arises from the competitive interplay between the LSPR field enhancement and the metal-induced quenching. In this study, we revealed the phosphorescence enhancement mechanism of metal-free purley organic phosphors by the plasmonic effect under ambient conditions. Our findings also prove that a proper spectral overlap between LSPR bands and excitation/target emission of the metal-free phosphors can lead to a largely enhanced phosphorescence emission intensity. The presented PPE strategy or the optimal conditions can be generally applicable to the potential application of metal-free phosphors.

3.6 References

1. Baldo, M.A., O'brien, D.F., You, Y., Shoustikov, A., Sibley, S., Thompson, M.E. and Forrest, S.R., "Highly Efficient Phosphorescent Emission from Organic Electroluminescent Devices." *Nature* **1998**, 395, 151-154.
2. You, Y., Han, Y., Lee, Y.M., Park, S.Y., Nam, W. and Lippard, S.J.,"Phosphorescent Sensor for Robust Quantification of Copper (II) Ion." *J. Am. Chem. Soc.* **2011**, 133, 11488-11491.
3. Zhao, Q., Huang, C. and Li, F., "Phosphorescent Heavy-metal Complexes for Bioimaging." *Chem. Soc. Rev.* **2011**, 40, 2508-2524.
4. Wang, B., Lin, H., Xu, J., Chen, H., Lin, Z., Huang, F. and Wang, Y., "Design, Preparation, and Characterization of a Novel Red Long-persistent Perovskite Phosphor: Ca3Ti2O7: Pr3+." *Inorg. Chem.* **2015**, 54, 11299-11306.
5. Yam, V.W.W., Au, V.K.M. and Leung, S.Y.L., "Light-emitting Self-assembled Materials based on d8 and d10 transition Metal Complexes." *Chem. Rev.* **2015**, 115, 7589
6. Bolton, O., Lee, K., Kim, H.J., Lin, K.Y. and Kim, J., "Activating Efficient Phosphorescence from Purely Organic Materials by Crystal Design." *Nat. Chem.* **2011**, 3, 205-210.
7. Kwon, M.S., Lee, D., Seo, S., Jung, J. and Kim, J., "Tailoring Intermolecular Interactions for Efficient Room-temperature Phosphorescence from Purely Organic Materials in Amorphous Polymer Matrices." *Angew. Chem. Int. Ed*. **2014**, 53, 11177-11181.
8. Pompa, P.P., Martiradonna, L., Della Torre, A., Della Sala, F., Manna, L., De Vittorio, M., Calabi, F., Cingolani, R. and Rinaldi, R., "Metal-enhanced Fluorescence of Colloidal Nanocrystals with Nanoscale Control." *Nat. Nanotechnol.* **2006**, 1, 126-130,
9. Khatua, S., Paulo, P.M., Yuan, H., Gupta, A., Zijlstra, P. and Orrit, M., "Resonant Plasmonic Enhancement of Single-molecule Fluorescence by Individual Gold Nanorods." *ACS nano* **2014**, 8, 4440-4449.
10. Kochuveedu, S.T. and Kim, D.H., "Surface Plasmon Resonance Mediated Photoluminescence Properties of Nanostructured Multicomponent Fluorophore Systems." *Nanoscale* **2014**, 6, 4966-4984.
11. Gandra, N., Portz, C., Tian, L., Tang, R., Xu, B., Achilefu, S. and Singamaneni, S., "Probing Distance-dependent Plasmon-Enhanced Near-infrared Fluorescence using Polyelectrolyte Multilayers as Dielectric Spacers." *Angew. Chem. Int. Ed.* **2014**, 53, 885-

889.

12. Cao, S.H., Cai, W.P., Liu, Q. and Li, Y.Q., "Surface Plasmon–coupled Emission: What can Directional Fluorescence bring to the Analytical Sciences?" *Annu. Rev. Anal. Chem* **2012**, 5, 317-336.
13. Saboktakin, M., Ye, X., Oh, S.J., Hong, S.H., Fafarman, A.T., Chettiar, U.K., Engheta, N., Murray, C.B. and Kagan, C.R., "Metal-enhanced Upconversion Luminescence Tunable through Metal Nanoparticle–Nanophosphor Separation." *ACS nano* **2012**, 6, 8758-8766.
14. Camposeo, A., Persano, L., Manco, R., Wang, Y., Del Carro, P., Zhang, C., Li, Z.Y., Pisignano, D. and Xia, Y., "Metal-Enhanced Near-infrared Fluorescence by Micropatterned Gold Nanocages." *ACS nano* **2015**, 9,10047-10054.
15. Kulakovich, O., Strekal, N., Yaroshevich, A., Maskevich, S., Gaponenko, S., Nabiev, I., Woggon, U. and Artemyev, M., "Enhanced Luminescence of CdSe Quantum Dots on Gold Colloids." *Nano Letters* **2002**, 2, 1449-1452.
16. Li, Z.Q., Chen, S., Li, J.J., Liu, Q.Q., Sun, Z., Wang, Z.B. and Huang, S.M., "Plasmon-Enhanced Upconversion Fluorescence in Nayf4: Yb/Er/Gd Nanorods Coated with Au Nanoparticles or Nanoshells." *J. Appl. Phys.* **2012**, 111, 014310.
17. Butun, S., Tongay, S. and Aydin, K., "Enhanced Light Emission from Large-Area Monolayer Mos2 using Plasmonic Nanodisc Arrays." *Nano letters* **2015**, 15, 2700-2704.
18. Miao, J., Hu, W., Jing, Y., Luo, W., Liao, L., Pan, A., Wu, S., Cheng, J., Chen, X. and Lu, W., "Surface Plasmon-enhanced Photodetection in few Layer Mos2 Phototransistors with Au Nanostructure Arrays." *Small* **2015**, 11, 2392-2398.
19. Liu, W., Lee, B., Naylor, C.H., Ee, H.S., Park, J., Johnson, A.C. and Agarwal, R., "Strong Exciton–plasmon Coupling in Mos2 Coupled with Plasmonic Lattice." *Nano letters* **2016**, 16, 1262-1269.
20. Kochuveedu, S.T., Son, T., Lee, Y., Lee, M., Kim, D. and Kim, D.H., "Revolutionizing the FRET-based Light Emission in Core-Shell Nanostructures via Comprehensive Activity of Surface Plasmons." *Sci. Rep.* **2014**, 4 ,4735
21. Previte, M.J., Aslan, K., Zhang, Y. and Geddes, C.D., "Metal-enhanced Surface Plasmon-Coupled Phosphorescence." *J. Phys. Chem. C* **2017**, 6051-6059.
22. Chaudhuri, D., Li, D., Sigmund, E., Wettach, H., Höger, S. and Lupton, J.M., "Plasmonic

Surface Enhancement of Dual Fluorescence and Phosphorescence Emission from Organic Semiconductors: Effect of Exchange Gap and Spin–Orbit Coupling." *Chem. Commun.* **2012**, 48, 6675-6677.

23. Kim, M., Lee, S.M. and Choi, K.C., "Optical Tuning of Phosphors by Plasmonic Gold Nanoparticles for Phosphor-Converted White Light Emitting Diodes." *App. Phys. Lett.* **2014**, 105, 141119.
24. Zhang, Y., Aslan, K., Malyn, S.N. and Geddes, C.D., "Metal-enhanced Phosphorescence (MEP)." *Chem. Phys. Lett.* **2006**, 427, 432-437.
25. Zhang, Y., Aslan, K., Previte, M.J., Malyn, S.N. and Geddes, C.D.,"Metal-enhanced Phosphorescence: Interpretation in Terms of Triplet-coupled Radiating Plasmons." *The J. Phys. Chem. B* **2006**, 110, 25108-25114.
26. Toftegaard, R., Arnbjerg, J., Daasbjerg, K., Ogilby, P.R., Dmitriev, A., Sutherland, D.S. and Poulsen, L., "Metal-Enhanced 1270 nm Singlet Oxygen Phosphorescence." *Angew. Chem. Int. Ed.* **2008**, 47, 6025-6027.
27. Planas, O., Macia, N., Agut, M., Nonell, S. and Heyne, B., "Distance-dependent Plasmon-enhanced Singlet Oxygen Production and Emission for Bacterial Inactivation." *J. Am. Chem. Soc* **2016**, 138, 2762-2768.
28. Seo, C., Lee, J., Kim, M.S., Lee, Y., Jung, J., Shin, H.W., Ahn, T.K., Sun, G., Kim, J. and Kim, J., "Plasmon-Enhanced Phosphorescence of Hybrid Thin Films of Metal-free Purely Organic Phosphor and Silver Nanoparticles." *Chem. Phys. Lett.* **2017**, 676, 134-139.
29. Chung, K., Rani, A., Lee, J.E., Kim, J.E., Kim, Y., Yang, H., Kim, S.O., Kim, D. and Kim, D.H., "Systematic Study on the Sensitivity Enhancement in Graphene Plasmonic Sensors based on Layer-by-layer Self-assembled Graphene Oxide Multilayers and their Reduced Analogues." *ACS Appl. Mater. Interfaces* **2015**, 7, 144-151.
30. Rycenga, M., Cobley, C.M., Zeng, J., Li, W., Moran, C.H., Zhang, Q., Qin, D. and Xia, Y., "Controlling the Synthesis and Assembly O\of Silver Nanostructures for Plasmonic Applications." *Chem. Rev.* **2011**, 111, 3669–3712.
31. Rani, A., Chung, K., Kwon, J., Kim, S.J., Jang, Y.H., Jang, Y.J., Quan, L.N., Yoon, M., Park, J.H. and Kim, D.H., "Layer-by-layer Self-assembled Graphene Multilayers as Pt-Free Alternative Counter Electrodes in Dye-Sensitized Solar Cells." *ACS Appl. Mater. Interfaces* **2016**, 8, 11488-11498.

32. Reineck, P., Gómez, D., Ng, S.H., Karg, M., Bell, T., Mulvaney, P. and Bach, U., "Distance and Wavelength Dependent Quenching of Molecular Fluorescence by Au@ Sio2 Core–Shell Nanoparticles." *ACS nano* **2013**, 7, 6636-6648.
33. Rohner, C., Tavernaro, I., Chen, L., Klar, P.J. and Schlecht, S., "Metal-enhanced Luminescence in Colloidal Solutions of Cdse And Metal Nanoparticles: Investigation of Density Dependence and Optical Band Overlap." *Phys. Chem. Chem. Phys*. **2015**, 17, 5932-5941.
34. Harun, N.A., Benning, M.J., Horrocks, B.R. and Fulton, D.A., "Gold Nanoparticle-Enhanced Luminescence of Silicon Quantum Dots Co-Encapsulated in Polymer Nanoparticles." *Nanoscale* **2013**, 5, 3817-3827.
35. Wu, X., Liu, L., Choy, W.C., Yu, T., Cai, P., Gu, Y., Xie, Z., Zhang, Y., Du, L., Mo, Y. and Xu, S., "Substantial Performance Improvement in Inverted Polymer Light-emitting Diodes via Surface Plasmon Resonance Induced Electrode Quenching Control." *Appl. Mater. Interface* **2014**, 6, 11001-11006.
36. Gryczynski, I., Malicka, J., Shen, Y., Gryczynski, Z. and Lakowicz, J.R., "Multiphoton Excitation of Fluorescence Near Metallic Particles: Enhanced and Localized Excitation." *J. Phys. Chem. B* **2002**, 106, 2191-2195.

Chapter 4

Metal–organic phosphor frameworks

In this chapter, metal-free phosphors incorporated into metal–organic frameworks (MOFs) are designed and synthesized to achieve enhanced phosphorescence compared to that of the pristine phosphor. This demonstrates the design principle of metal–organic phosphors frameworks and their potential application. First, we demonstrate how to design a ligand for metal–organic frameworks from metal-free phosphors. In the next section, we explain how to achieve RTP from metal–organic frameworks, and we describe a failed attempt in detail. Finally, we develop a bright phosphorescent metal–organic framework−PS composite system with metal-free phosphors, which shows a versatile design principle to make metal–organic frameworks with metal-free phosphors. The new system implies the feasibility to enhance phosphorescence in the presence of a metal in MOF.

4.1 Introduction

One of the most important factors for achieving bright RTP from organic molecule is efficiently suppressing vibration. Previous studies [1, 2] have revealed that dominant nonradiative decay process at r.t. is collision-based vibration quenching by triplet–triplet energy transfer (or Dexter-type triplet–triplet energy transfer). Therefore, the host polymer matrix must be carefully selected to avoid the activation of collision quenching between the polymer host and the phosphor guest to effectively prevent nonradiative decay, thus enabling bright RTP, as bright as phosphorescence at 77 K. For example, a few host matrices that can suppress nonradiative decay processes have been reported, such as hydroxyl-steroids[3] and the PMMA doped with BrFL1 described in Chapter 2. If collision between the host matrix and phosphor is prevented, we can achieve bright phosphorescence at room temperature.

Metal–organic frameworks (MOFs) are metal–organic ligand hybrids materials, which having a three-dimensional (3-D) periodic structure and large internal pores. MOF research has focused on controlling the pore size or shape so that MOFs can be rationally designed for use in gas storage or gas separation.[4-6] In this study, we attempt to explore their large pores to avoid collisions between phosphors and their environment, thus suppressing the nonradiative decay process and enhancing phosphorescence[7]. In addition, we study the effect of metal on SOC and phosphorescence intensity.

The biggest challenge to designing MOFs with metal-free phosphors is not knowing whether the resulting MOFs exhibit the same or similar photophysical properties of the constituent metal-free phosphors. Moreover, we do not know whether collision quenching can be avoided by incorporating organic phosphor units into MOFs. Thus, we began our exploration of a new system to improve RTP by trial and error when designing new ligands and MOFs. All MOFs studied in this chapter were prepared through collaboration with Jialiu Ma in the Matzger group. This work suggests a dew useful design rules to utilize MOF to host organic phosphor ligands toward novel bright RTP.

4.2 Experiments

4.2.1 General Methods

All chemicals were purchased from Sigma Aldrich and used without further purification. UV absorption measurements were collected using a Varian Cary 50 Biospectrometer with solution samples held in quartz cuvettes. PL emission, excitation, and QY data were collected

using a PTI QuantaMaster system equipped with an integrating sphere. Quantum lifetime data were collected using a PTI LaserStrobe. Quantum lifetimes were calculated using Origin 8.0 Pro. Low-temperature measurements were recorded on a Janis VPF-1000 cryostat.

4.2.2 Synthesis of molecules and fabrication of MOFs and MOF–PS composite

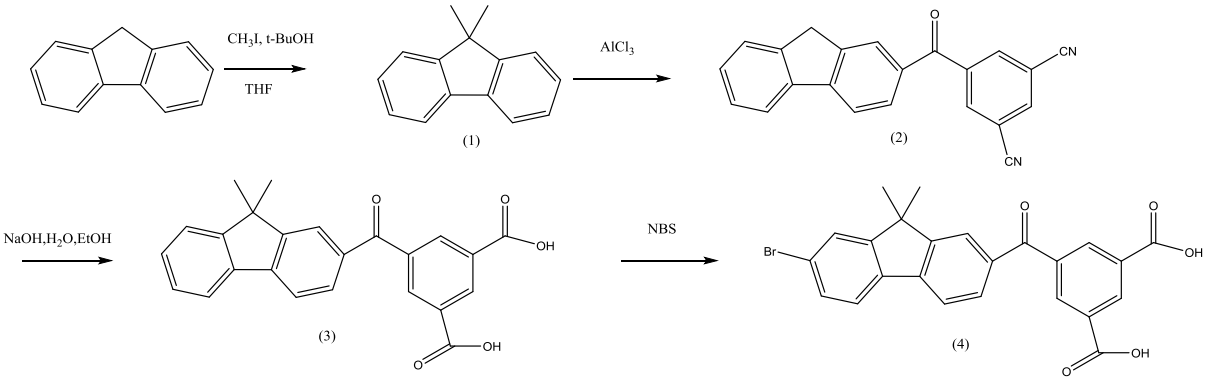

Scheme 4.1 Synthetic route to phosphor ligand (4).

Synthesis of 9,9-dimethyl-9H-fluorene (1). t-BuOH powder (3 equiv.) was added to a 9-H solution of fluorene (1 equiv.) in THF at 0℃. The resulting solution was stirred for 30 min, and iodomethane (3 equiv.) was then added. The reaction was stirred at r.t. overnight. The reaction was quenched by adding water and extracted with hexanes. The organic layer was collected and dried over $MgSO_4$ before being filtered and evaporated under reduced pressure. Purification was performed by column chromatography with hexane. White powder was collected in a yield of 61%. ^{1}H NMR (300 MHz, $CDCl_3$): δ 7.76-7.73 (d, 2H), 7.47-7.44 (d, 2H), 7.38-7.31 (m, 4H), 1.51 (s, 6H).

Synthesis of (3,5-dibromophenyl)(9,9-dimethyl-9H-fluoren-2-yl)methanone (2). 3,5-dibromobenzoic acid (1 equiv.) was dissolved in $SOCl_2$ and refluxed overnight. The resulting solution was evaporated and dissolved in anhydrous dichloromethane under an argon atmosphere. $AlCl_3$ (1.2 equiv.) was slowly loaded into the solution at 0℃. (1) (1 equiv.) was carefully added to the red-brown suspension, and the reaction was stirred overnight. The mixture was poured into ice water, and saturated HCl was added until all precipitates disappeared. The organic layer extracted by dichloromethane was collected and dried over $MgSO_4$ before being filtered and evaporated under reduced pressure. Purification was performed by column chromatography with hexane/dichloromethane. Powder was collected

in a yield of 21%. ^{1}H NMR (300 MHz, $CDCl_3$): δ 7.93 (s, 1H), 7.90-7.85 (d, 3H), 7.84-7.77 (d, 2H), 7.70-7.75 (d, 2H), 7.5-7.45 (d, 1H), 7.42-7.37 (m, 2H),1.56 (s, 6H).

Synthesis of 5-(9,9-dimethyl-9H-fluorene-2-carbonyl)isophthalonitrile (3). CuCN (5 equiv.) powder was added to the solution of (2) (1 equiv.) in DMF. After refluxing for 10 hours, the reaction was quenched by adding water. The organic layer extracted by ethyl acetate was collected and dried over $MgSO_4$ before being filtered and evaporated under reduced pressure. Purification was performed by column chromatography with hexane/dichloromethane. White powder was collected in a yield of 61%.^{1}H NMR (300 MHz, $CDCl_3$): δ 8.31 (s, 2H), 8.2-8.13 (m, 1H), 7.96-7.94 (m, 1H), 7.89-7.82 (m, 3H), 7.69-7.65 (m,1H), 7.55-7.47 (m,1H), 7.45-7.4 (m, 2H), 1.56 (s, 6H).

Synthesis of 5-(7-bromo-9,9-dimethyl-9H-fluorene-2-carbonyl)isophthalic acid (4). (3) was added to 2 N NaOH aqueous solution/ethanol (5:1) and the precipitated solution was refluxed overnight. After cooling to r.t. and precipitating, the solution was extracted by ethyl acetate. The organic layer was collected and dried over $MgSO_4$ before being filtered and evaporated under reduced pressure. Isolated (4) was used for the next reaction without further purification. (4) (1 equiv.) was dissolved in chloroform, and acetic acid and bromide (1.2 equiv.) were added to the solution. After the reaction was completed, the reaction was quenched by adding a NaS_2CO_3 aqueous solution. The organic layer extracted by chloroform was collected and dried over $MgSO_4$ before being filtered and evaporated under reduced pressure. Purification was performed by column chromatography with methanol/chloroform. White powder was collected in a yield of 40%. ^{1}H NMR (300 MHz, DMSO-d6): δ 9.29 (s, 2H), 8.2-8.1 (m, 2H), 8.1-8.0 (m, 1H), .7.99-7.88 (m, 3H), 7.79-7.70 (m,1H), 7.65-7.57 (m,1H), 1.50 (s, 6H).

MOF-5. MOF-5 was synthesized based on the published procedure[8]. All MOFs studied in this chapter were prepared through collaboration with Jialiu Ma in the Matzger group. Terephthalic acid (0.602 mmol), $Zn(NO_3)_2$-$4H_2O$(1.91), and 15 mL of diethylformamide were added to a 20 mL vial. The mixture was sonicated for 15 min until the compounds were dissolved completely, and the solution was heated to 100℃ for 18-24 hours to obtain colorless cubic crystals of MOF-5. The MOF-5 crystals were washed with diethylformamide

and dried under vacuum. The compound was stored in a glovebox under a nitrogen atmosphere.

MOF-5-encapsulated BrFL1. MOF-5 was soaked in a solution of BrFL1 in chloroform for 24 hours. The solution was decanted, and MOF-5 crystals were washed with chloroform and dried under vacuum. The compound was stored in a glovebox under a nitrogen atmosphere.

BrFL6@MOF-5. MOF-5 was synthesized based on a slightly modified version of a previously published procedure**.** The fabrication method was the same except the starting reagent. Specifically, instead of using only terephthalic acid, BrFL6 was mixed with terephthalic acid.

Amine-modified surface treatment and attachment of BrFL5 on the surface[9]**.** A glass slide (2.54×7.62 cm) was incubated in ammonium hydroxide/water/35%hydrogen peroxide (1:4:1 v/v/v) solution at 80℃ for 1 hour. The slide was rinsed with a sufficient amount of deionized water and dried with blowing air. The amine-functionalized glass was incubated in a solution of acid chloride of compound (7) from chapter 2 in dichloromethane for 48 hours. The glass was rinsed with dichloromethane and stored in glovebox under a nitrogen atmosphere.

BrFL6@MOF-5–PS (Polystyrene). MOF-5-BrFL5 crystals (0.1 g) and purified styrene (10 mL) were added to 20 mL vial, and the mixture was heated at 65℃ for 24 hours to obtain colorless MOF-5–PS–BrFL5 composite crystal. Next, the styrene was decanted, and MOF-5–PS–BrFL5 crystals were washed with THF and dried under vacuum. The compound was stored in a glovebox under a nitrogen atmosphere.

4.3 Results and Discussion

4.3.1 Design of a ligand for phosphorescent MOFs

Effective immobilization using secondary or covalent bonding between phosphors and the polymer matrix can significantly reduce vibration frequency and enhance RTP[1,10](Fig. 4.1(a)). However, the activation temperature of vibrational quenching the resulting phosphor-immobilized polymer film experiences could be even lower than that of polymer films having simply embedded phosphors, implying that immobilization can reduce the collision

frequency but cannot prevent collision quenching. Metal–ligand bonding of MOFs was reported to hinder the rotation and vibration of AIE molecules and enhance their fluorescence[11] (Fig. 4.1(b)). We hypothesized that if phosphors are rationally deisgned and used as the ligand for MOFs, enhanced RTP can be achieved. Unlike the reported immobilized phosphors, the phosphors will be caged within the empty space of MOFs, which may suppress collision quenching and phosphorescence is consequently further enhanced.

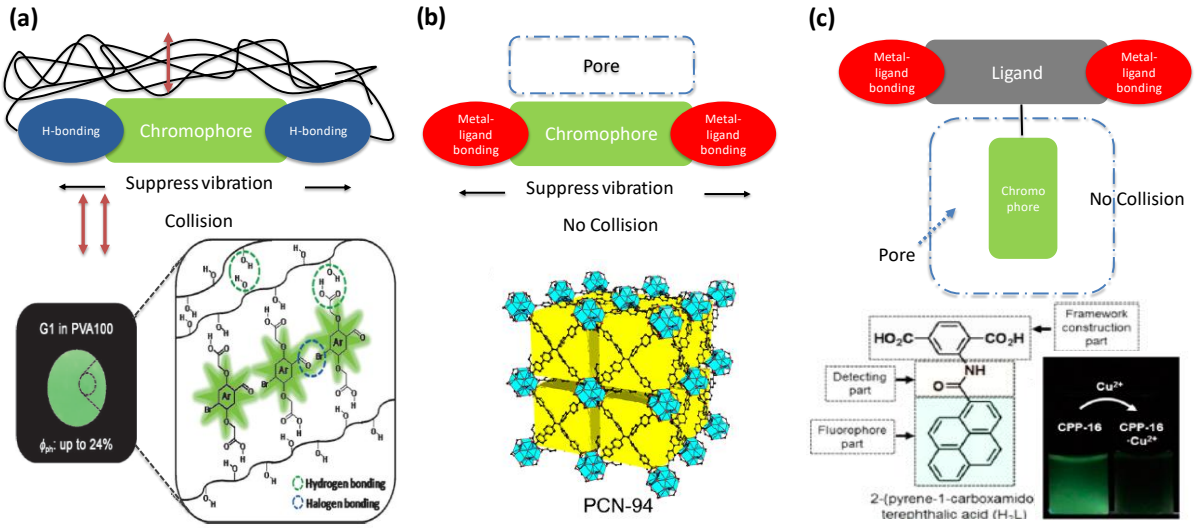

Figure 4.1 Schematic illustration of the method to suppress the vibration of chromophores in a polymer or MOF host. (a) Immobilization via secondary interactions between phosphors and polymer matrix. Image from *Angew. Chem. Int. Ed*. **2014**, 53, 11177. (b) The rigid frameworks prevent the chromophore from rotating or vibrating. Image from *J. Am. Chem. Soc.*, **2014**, *136* (23), 8269-8276 (c) The chromophore is located in the pore of the MOF, which may enable preventing the collision between the chromophore and environment. Image from J. *Am. Chem. Soc.*, **2014**, *136*, 12201.

We designed and synthesized a new hybrid ligand having an organic phosphor as a side chain to build phosphorescent MOFs (Fig. 4.2(a)). The hybrid ligand consists of a phosphor unit and terephthalic acid as a MOF construction component. The phosphor unit is structurally similar to BrFL2 described in Chapter 2. When the phosphor unit is connected to the isophthalic acid moiety through ketone linkage as shown in Figure 4.2 (a), RTP was not observed from the PMMA blend films with the resulting ligand even after the epoxy seal to prevent oxygen permeation. However at 77 K, afterglow or persistent phosphorescence was

observed. Because BrFL2 studied in Chapter 2 having a very similar structure exhibits millisecond phosphorescence at 77 K and room temperature, the afterglow implies that the intrinsic photophysical properties of BrFL2 changed after the conjugation with the isophthalic acid moiety. The formed extended conjugation is believed to change the photophysical properties of the new ligand shown in Figure 4.2 (a). Thus, we could not use the developed new ligand to build phosphorescent MOFs.

We designed and synthesized a phosphorescent molecule as a ligand for MOFs (Fig. 4.2(a)). The molecule consists of a chromophore and MOF construction component, including two carboxylic acid groups. The chromophore is similar in structure to BrFL2 in chapter 2. The chromophore is π-conjugated to the MOF construction component. RTP was not observed from the ligand doped PMMA film with epoxy sealing. At 77 K, afterglow or persistent phosphorescence was observed. Because BrFL2 exhibits millisecond phosphorescence at 77 K and r.t., the afterglow implies that the intrinsic photophysical properties of BrFL2 changed after molecular modification. Thus, we could not use the molecules as a ligand for the phosphorescent MOFs did not exhibit RTP. The functionality of carboxylic acid may influence the photophysical properties of BrFL2 through π-conjugation.

To keep the intrinsic photophysical properties of the phosphor unit in the hybrid ligand, we designed a new molecule, BrFL6, in which the phosphor unit and the terephthalic acid moiety are connected through an amide linkage (Fig. 4.2(b)) so that the two units are not π-conjugated. The molecular structure of the phosphor unit is similar to that of BrFL5 investigated in Chapter 2. To ensure that the intrinsic photophysical properties of the phosphor unit were not altered, the phosphorescence spectrum and lifetime of BrFL6 were measured. The fluorescence and phosphorescence spectra of a BrFL6-doped PMMA film after epoxy sealing were obtained (Figure 4.3). The peak at 370 nm is fluorescence because the Stokes shift is small. The phosphorescence peak was detected by a gated-PL measurement. The peak around 500 nm essentially the same as the phosphorescence spectrum of BrFL5. Although the fluorescence intensity of BrFL6 is much higher than that of BrFL5, indicating that the terephthalic acid moiety influences the photophysical properties such as ISC and radiative decay rate of fluorescence, the intrinsic phosphorescent properties are mostly conserved. The QY of a BrFL6-doped PMMA film was calculated to be 21.4%, and the phosphorescence lifetime was 8.96 ms.

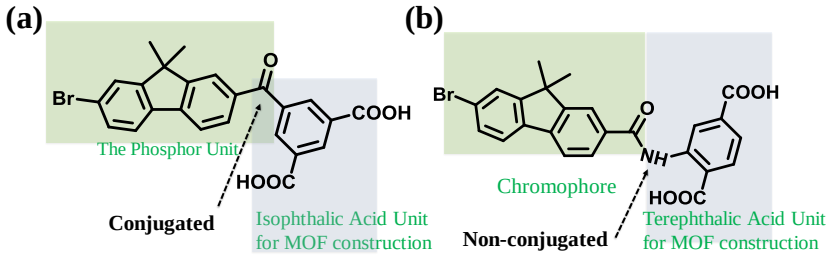

Figure 4.2 Chemical structures of the designed hybrid phosphorescent ligand for MOFs. The hybrid ligands consist of the phosphor unit and the terephthalic acid moiety. (a) The two units are π-conjugated. (b) The two units are not π-conjugated.

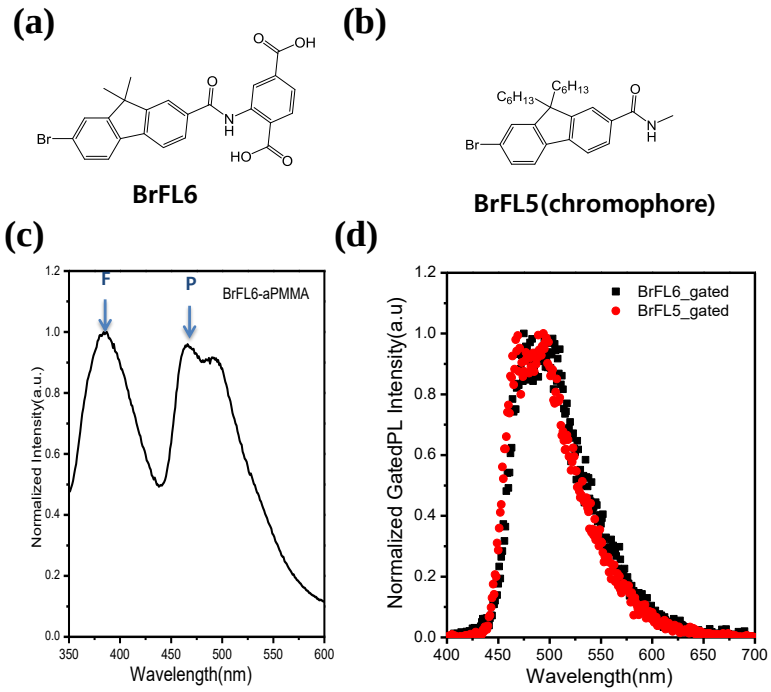

Figure 4.3 Molecular structure of the ligand (a) and chromophore (b). (c) PL spectrum of BrFL6-doped PMMA film with epoxy sealing. "F" and "P" are the fluorescence and phosphorescence peaks, respectively. (d) Gated PL spectrum of BrFL6 and BrFL5 (chromophore component)-doped PMMA film with epoxy sealing.

The newly synthesized hybrid phosphor ligand for MOFs exhibited similar phosphorescence properties to those of the pristine phosphor unit. Even though the carboxylic acid functionality binds to the metal during the fabrication of MOFs, the non-π-conjugated amide linkage discontinue any further influence on the phosphor unit. Therefore, we could use the BrFL6 as a hybrid phosphorescent ligand to build MOF and investigate the

phosphorescence properties of the phosphor unit after fabricating the MOFs.

4.3.2 Fabrication of MOFs and analysis of their photophysical properties

Before fabricating and characterizing the phosphorescent MOFs, the photophysical properties of the MOF-5 sample encapsulating BrFL1 (Fig. 4.4) were obtained. The MOF-5-encapsulated BrFL1 was prepared by soaking MOF-5 in a solution of BrFL1. From ^{1}H-NMR analysis, we obtained a ratio of BrFL1 to terephthalic acid of 1:17. Phosphorescence was not observed even in liquid nitrogen (77 K). In addition, no phosphorescent signal was detected by photospectrometer under high vacuum ($<10^{-4}$ torr), even at 77 K. A recent paper reported RTP from MOF-encapsulated phosphors[12] and and emphasized that the host MOF should be selected carefully to match its pore diameter to the size of the phosphor molecule encapsulated. In the case of BrFL1, the molecule (~1.1 nm) is smaller than the pore of MOF-5 (1.5 nm), which cannot securely hold guest molecules within its cavities. Therefore, BrFL1 in MOF-5 may freely move around and collide with the MOF frame, leading to nonradiative decay.

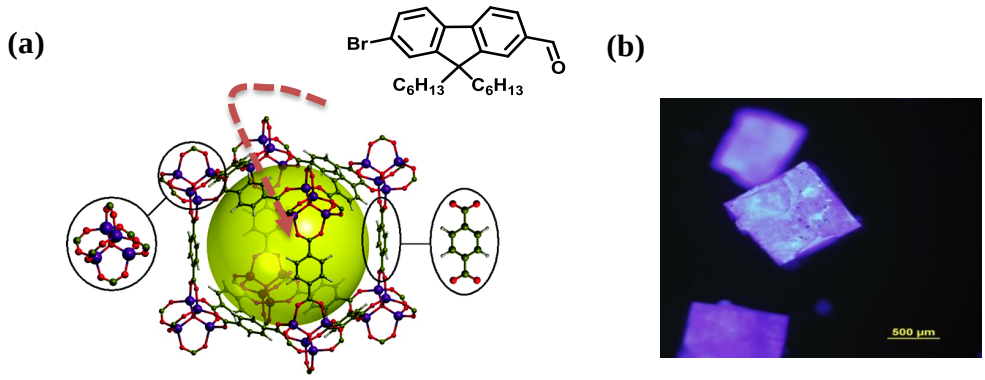

Figure 4.4 (a) Schematic illustration of MOF-5-encapsulated BrFL1 (b) Optical microscope image of MOF-5-encapsulated BrFL1.

We fabricated BrFL6@MOF-5 by using BrFL6 and terephthalic acid as co-lignds. ^{1}H-NMR analysis revealed that the ratio of BrFL6 to terephthalic acid was 1:16. The phosphorescence of BrFL6@MOF-5 was too weak to be visible to the naked eye even at 77 K. As seen in Fig. 4.6, the phosphorescence spectrum of BrFL6@MOF-5 was mostly identical to that of the BrFL6-doped PMMA film, indicating that the obtained phosphorescent signal originated from the BrFL6 ligand. However, their temperature dependent

phosphorescence intensity was completely different from each other. As described in Chapter 2, the phosphorescence intensity of the BrFL6-doped PMMA film remains constant while temperature increases up to the β-relaxation temperature at which collisions between the polymer matrix and phosphors are activated. In contrast, the phosphorescence intensity of BrFL6@MOF-5 reduced continuously with increasing temperature. Because the phosphor unit of BrFL6 is smaller than the pore of MOF-5, we postulated that collisions between the phosphor unit of BrFL6 and the MOF framework are responsible to this phenomenon.

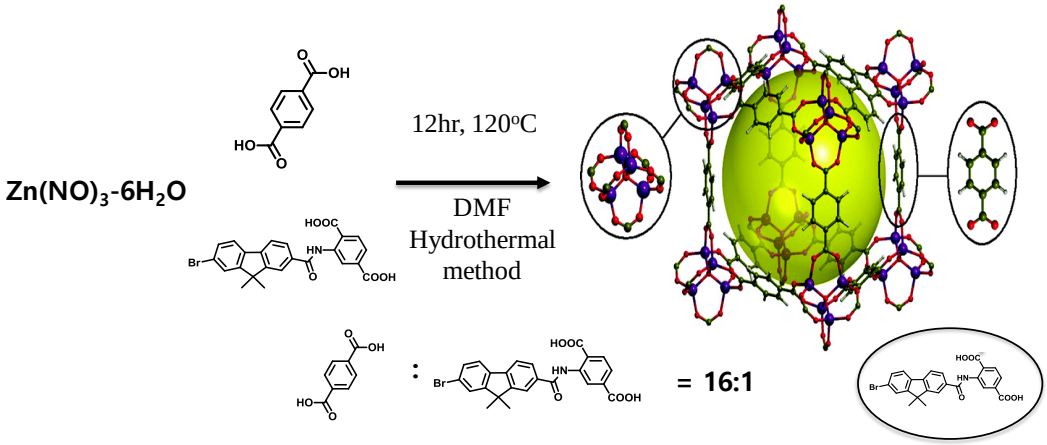

Figure 4.5 Synthesis method of BrFL6@MOF-5 and schematic illustration of MOF-BrFL6@MOF-5.

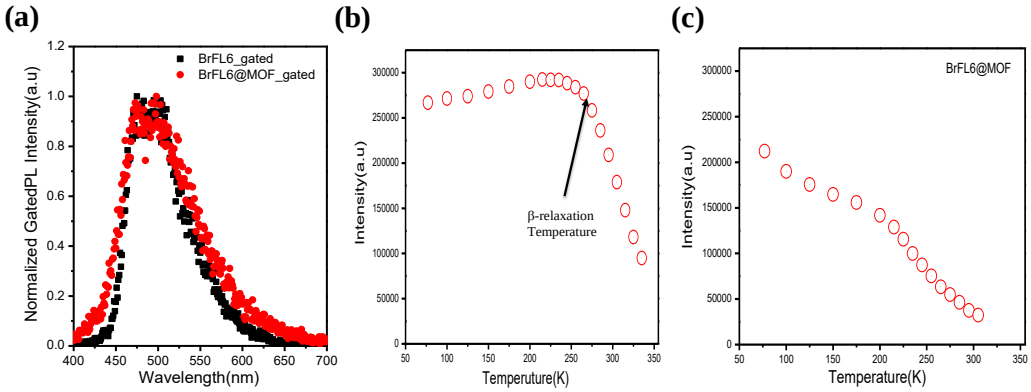

Figure 4.6 (a) Gated PL spectrum of BrFL6-doped PMMA film and BrFL6@MOFs. (b) Temperature-dependent phosphorescence intensity of (b) BrFL6-doped PMMA film and (c) BrFL6@MOFs.

The intramolecular vibration of metal-free phosphors is not significant compared to the intermolecular vibration at room temperature. Therefore, nonradiative decay process would be related to mainly intermolecular vibration. Because the BrFL6 phosphor unit is located in

the larger size pore of the MOF, we hypothesized that collision of BrFL6 with MOF framework is the origin of the intermolecular vibration. To understand why the phosphorescence intensity of BrFL6@MOFs decays with increasing temperature, we tethered BrFL5 on a glass substrate as shown in Fig. 4.7 (a). The attachment of BrFL5 to the glass surface was confirmed by its phosphorescence in liquid nitrogen and its gated PL spectrum. The phosphorescence intensity decreased continuously as temperature increased from 77 K. The profile of the temperature dependence of phosphorescence was identical to that of BrFL6@MOF-5. Therefore, the collision quenching can be attributed to the collisions among the dangling BrFL5.

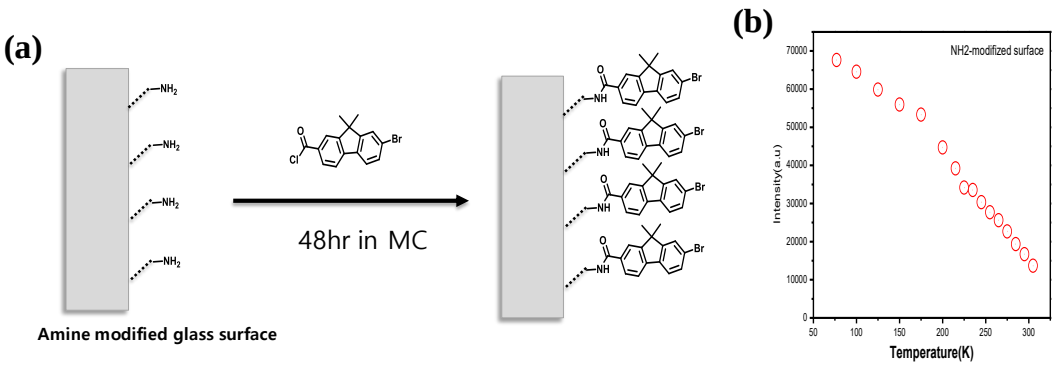

Figure 4.7 (a) Schematic illustration of the tethering of BrFL5-derivative to an amine-modified glass to make a BrFL5-tethered glass surfaces. (b) Temperature-dependent phosphorescence intensity of the BrFL5-tethered glass surface.

4.3.3 Fabrication of BrFL6@MOF–PS composite and analysis of its photophysical properties

In order to prevent the phosphor unit of BrFL6 from moving inside the MOFs, we attempted to fill polymer into the MOFs. The MOF-5–PS composite is formed by heating neat styrene in the presence of MOF-5 at 65℃ for 24 hours. The MOF–PS composites were prepared from BrFL6@MOF-5-PS and MOF-5-encapsulated BrFL6, respectively. Figure 4.8 shows the image of the MOF-PS composites under 365 nm UV irradiation in a glovebox with a nitrogen atmosphere. Cyan-green phosphorescence was observed from BrFL6@MOF-5–PS composite but not from MOF-5–PS-encapsulated BrFL6. We believe that in the case of MOF-5–PS-encapsulated BrFL6 composite BrFL6 cannot be held in the MOF pore because the diameter of the pore is smaller (<1.5 nm) than the size of BrFL6.

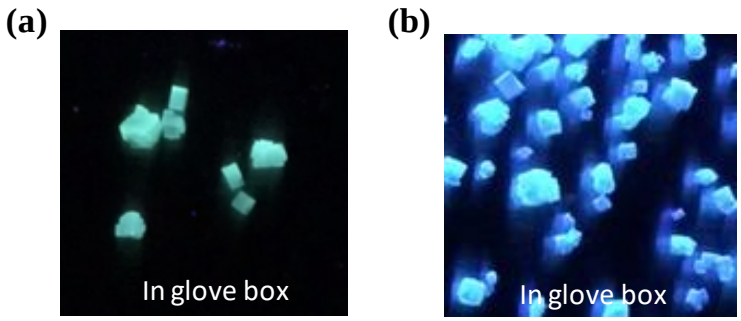

BrFL6@MOF-5-PS MOF-5-PS Encapsulating BrFL6

Figure 4.8 Photo of (a) BrFL6@MOF-5–PS and (b) MOF-5–PS-encapsulated BrFL6 in a nitrogen-filled glovebox under 365 nm UV irradiation.

We characterized the temperature dependence of phosphorescence intensity of BrFL6@MOF-5–PS (Figure 4.9) under high vacuum conditions. Phosphorescence of a benzophenone-doped PS film is known to decay at 150 K, the γ-relaxation temperature of PS. The phosphorescence of BrFL6@MOF-5–PS under vacuum also decayed around 150 K, and consequently the phosphorescence intensity was too low at room temperature. However, RTP was observed under a nitrogen atmosphere. An encapsulated BrFL6@MOF-5–PS sample under a nitrogen atmosphere with epoxy sealing was prepared and characterized. The phosphorescence of the sample decayed at around 355 K, α-relaxation temperature of PS. It seems that under the vacuum condition there are move free volume within the pore of BrFL6@MOF-5–PS, thereby the movement of the phosphor unit within the pore cannot be effectively prevented. We confirmed that the BrFL6-doped drop-casted PS film exhibited phosphorescence decay at the α-relaxation temperature of PS. We concluded that the most important design parameter of phosphorescent MOFs is how to suppress the vibration or the movement of the phosphor unit in the pore of MOFs. Therefore, to effectively prevent the movement of the phosphor unit or the vibration of amide linkage in MOF-5–PS, the phosphor unit must be tightly bound on the framework, and the filled polymer inside MOF-5–PS must be rigid.

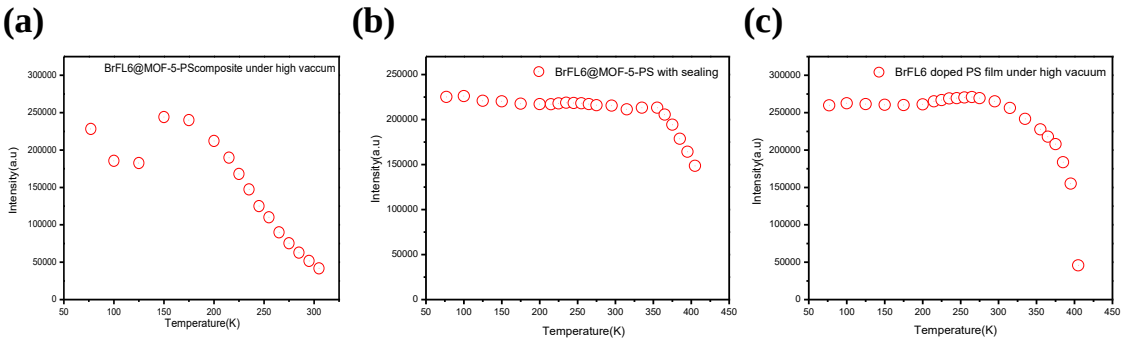

Figure 4.9 Temperature dependence of phosphorescence intensity of (a) BrFL6@MOF-5–PS under high vacuum, (b) BrFL6@MOF-5–PS with epoxy sealing, and (c) BrFL6-doped PS film under high vacuum.

The photophysical properties of BrFL6@MOF-5–PS were measured with epoxy sealing. As shown in Figure 4.10, both fluorescence and phosphorescence, i.e., dual emissions, were detected. Unlike the BrFL6-doped PMMA film, the fluorescence intensity of BrFL6@MOF-5–PS is much higher than the phosphorescence intensity possibly because the fluorescence spectrum of MOF-5 (or the terephthalic acid ligand component of MOF-5) contributed to the overall fluorescence intensity.

In order to accurately determine the phosphorescence QY, we must deconvolute phosphorescence from PL spectrum. The phosphorescence QY of BrFL6@MOF-5–PS was 26.9%. The lifetime was measured to be 13.3 ms. Even though the QY is similar to that of BrFL6-doped PMMA film, the fluorescence QY of BrFL6@MOF-5–PS (57.3%) is much higher than that of BrFL6-doped PMMA film (25.5%), indicating that singlet-to-triplet ISC of BrFL6@MOF-5–PS is less efficient, but the phosphorescence conversion from the triplet exciton is more efficient. Assuming that ISC yield is calculated by subtracting the fluorescence QY from unity, the phosphorescence radiative decay (k_p) of BrFL6@MOF-5–PS is 50.6 s^{-1}, and nonradiative decay (k_{nr}) is 24.7 s^{-1}. The k_p of BrFL6@MOF-5–PS is higher than that of BrFL6-doped PMMA (34.2 s^{-1}), indicating that phosphorescence process is enhanced in MOFs. Moreover, the k_{nr} of BrFL6@MOF-5–PS is lower than that of BrFL6-doped PMMA (34.2 s^{-1}). This might be because the movement of the phosphor unit is suppressed by the polymer matrix as well as the binding to the framework. Therefore, MOF-5–PS can not only enhance phosphorescent processes but also suppress vibration.

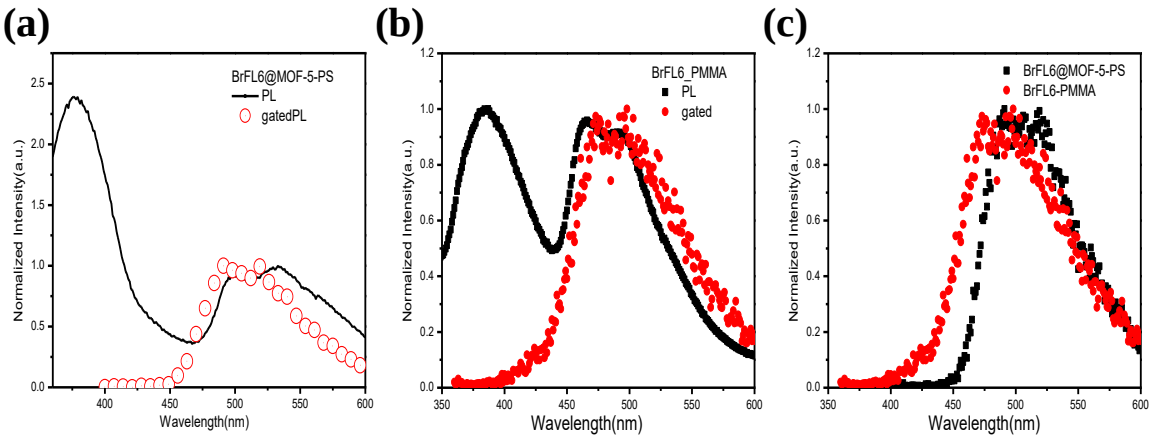

Figure 4.10 PL and gated PL spectra of (a) BrFL6@MOF-5–PS and (b) BrFL6-doped PMMA film. (c) Gated PL spectra of BrFL6@MOF-5–PS and doped PMMA.

4.4 Conclusion

First, the phosphor unit and the terephthalic acid unit for conjugation with metal should not be π-conjugated because the the terephthalic acid unit can alter the intrinsic phosphorescence properties of the phosphor unit if π-conjugated. To suppress the vibration of the phosphor unit in MOFs, the phosphor component must be held by the polymer matrix and linkage on frameworks. The analysis of phosphorescent properties of BrFL6@MOF-5–PS indicated that MOFs can suppress vibration as well as enhance the phosphorescent radiative decay, thereby improving overall phosphorescence efficiency. Thus, this work suggests a design principle for phosphorescent MOFs that applies to the development of potential applications such as hypersensitive oxygen detection by exploring the high porosity of MOFs and the oxygen sensitivity of phosphorescent materials.

4.5 References

1. Kwon, M.S., Yu, Y., Coburn, C., Phillips, A.W., Chung, K., Shanker, A., Jung, J., Kim, G., Pipe, K., Forrest, S.R. Youk, J.H., Gierschner, J., and Kim, J., "Suppressing Molecular Motions for Enhanced Room-temperature Phosphorescence of Metal-Free Organic Materials" *Nat. Commun.* **2015** 6, 1-9.
2. Hirata, S., "Recent Advances in Materials with Room Temperature Phosphorescence: Photophysics for Triplet Exciton Stabilization." *Adv. Opt. Mater.* **2017**, 5, 1700116.
3. Hirata, S., Totani, K., Zhang, J., Yamashita, T., Kaji, H., Marder, S.R., Watanabe, T. and Adachi, C., "Efficient Persistent Room-temperature Phosphorescence in Organic Amorphous Materials under Ambient Conditions." *Adv. Funct. Mater.* **2013**, 23 3386-3397.
4. Morris, R.E. and Wheatley, P.S., "Gas Storage in Nanoporous Materials." *Angew. Chem. Int. Ed*. **2008**, 47, 4966-4981.
5. Li, J.R., Kuppler, R.J. and Zhou, H.C., "Selective Gas Adsorption and Separation in Metal–Organic Frameworks." *Chem. Soc. Review.* **2009**, 38, 1477-1504.
6. McDonald, T.M., Mason, J.A., Kong, X., Bloch, E.D., Gygi, D., Dani, A., Crocella, V., Giordanino, F., Odoh, S.O., Drisdell, W.S. and Vlaisavljevich, B., "Cooperative Insertion of CO2 in Diamine-appended Metal-Organic Frameworks." *Nature* **2015**, 519, 303-308.
7. Cho, W., Lee, H.J., Choi, G., Choi, S. and Oh, M., "Dual Changes in Conformation and Optical Properties of Fluorophores within a Metal–Organic Framework during Framework Construction and Associated Sensing Event." *J. Am. Chem. Soc.* **2014**, 136, 12201-12204.
8. Gamage, N.D.H., McDonald, K.A. and Matzger, A.J., "MOF-5-Polystyrene: Direct Production from Monomer, Improved Hydrolytic Stability, and Unique Guest Adsorption." *Angew. Chem. Int. Ed*. **2016**, 128, 39, 12278-12282.
9. Lee, K., Rouillard, J.M., Kim, B.G., Gulari, E. and Kim, J., "Conjugated Polymers Combined with a Molecular Beacon for Label-free and Self-Signal-amplifying DNA Microarrays." *Adv. Funct. Mater.* **2009**, 19, 3317-3325.
10. Kwon, M.S., Lee, D., Seo, S., Jung, J. and Kim, J., "Tailoring Intermolecular Interactions for Efficient Room-Temperature Phosphorescence from Purely Organic Materials in Amorphous Polymer Matrices." *Angew. Chem. Int. Ed*. **2014**, 53, 11177-11181.

11. Wei, Z., Gu, Z.Y., Arvapally, R.K., Chen, Y.P., McDougald Jr, R.N., Ivy, J.F., Yakovenko, A.A., Feng, D., Omary, M.A. and Zhou, H.C., "Rigidifying Fluorescent Linkers by Metal–Organic Framework Formation for Fluorescence Blue Shift and Quantum Yield Enhancement." *J. Am. Chem. Soc.* **2014**, 136, 8269-8276.
12. Mieno, H., Kabe, R., Notsuka, N., Allendorf, M.D. and Adachi, C., "Long-Lived Room-Temperature Phosphorescence of Coronene In Zeolitic Imidazolate Framework ZIF-8." *Adv. Opt. Mater.* **2016**, 4, 1015-1021.

Chapter 5

Conclusions and future considerations

5.1 Summary

The purpose of my dissertation is to develop bright RTP from metal-free phosphors through the molecular design principle and external agents such as host matrices or plasmonic nanometals. In contrast with widely used organometallic phosphors, metal-free molecules are not considered room-temperature phosphors since the rate of radiative T^1 to S_0 decay is usually very low without heavy-metal atoms; thus, most triplet excitons are consumed through nonradiative processes such as vibrational dissipation at ambient temperature. Recent progress in the field of metal-free phosphors has various demonstrated various methods that achieve bright RTP by reducing the rate of nonradiative decay to be as slow as the rate of phosphorescence radiative decay through phosphorescent crystals or host–guest systems[1,2]. However, the effect of the molecular structure on phosphorescent properties such as SOC or nonradiative decay has not been well studied. Moreover, methods to improve phosphorescent radiative decay are not well established. The molecular design principle and the newly developed method demonstrated in this work provide a new impetus to create a novel bright RTP system with potential applications and unique material properties.

Phosphorescence from organic molecules stems from triplet states, which give these materials unique features. For example, phosphorescent materials are more efficient in solid-state lighting devices because they can use energy from both the singlet and triplet states, which is generated from theoretically 100% charge recombination in the devices[3]. In addition, bioactivities can be detected based on oxygen concentration by exploiting the oxygen quenching properties of phosphorescence, wherein the ground-state triplet oxygen takes energy from the triplet state of the phosphorescent materials, thus quenching their emission[4]. Thus, the long-lived triplets of organic molecules, which last even longer than those of conventional organometallic compounds, are desirable in singlet oxygen generation because they can generate it while the triplet state still exists. Additionally, a high-resolution image

can be obtained from phosphorescent materials because signals with longer lifetimes are easily distinguished from the short-lifetime fluorescence or autofluorescence.

New metal-free phosphors must be developed because of the low performance of previously reported metal-free phosphors (e.g., brightness and color) and the limitations of organometallic compounds such as uncertain toxicity and short-lived triplets. The known design elements of metal-free phosphors such as aldehydes and halides are not guaranteed to achieve bright RTP. The stringent requirements on the host matrix or crystal formation limit the practicality of these organic phosphors. To overcome these limitations, we developed a versatile design principle to fabricate new phosphors.

To improve the QY of phosphorescence, enhancement of the rate of phosphorescence radiative decay is as important as the suppression of vibration. Recent progress reported for RTP has mostly focused on methods to suppress vibration and enhance phosphorescence[5,6]. With high demands for phosphorescent applications, the need for a method to enhance radiative decay is significant.

In Chapter 2, the general design principles of metal-free phosphors were demonstrated by studying the effects of molecular structure on nonradiative decay by intramolecular vibration, phosphorescence radiative decay, and nonradiative decay by intermolecular vibration. The rigidity of molecular structure can decrease nonradiative decay based on intramolecular vibration as much as nonradiative decay by intermolecular vibration, which was generally considered to be dominant in nonradiative decay. It was revealed that carbonyl groups do not exhibit a synergic effect with halides but influence the strength of the heavy-atom effect. The functionality of substitutions on molecules can control SOC and enhance phosphorescence radiative decay as well as tune their color. We first reported that the size of molecules is strongly related to the phosphorescence quenching due to the thermal motion of the polymer matrix. We then demonstrated that the phosphorescent decay can be prevented at room temperature by using small phosphors in a conventional polymer matrix. The molecular design strategy can provide an impetus for developing bright RTP for real applications.

The enhanced phosphorescence from organic phosphors was demonstrated by using LSPR. The concept of LSPR-enhanced phosphorescence was proven using a three-layer sample composed of a Br6/Br6A-doped crystal, a spacer controlled by layer-by-layer technique, and plasmonic nanometals. The thickness layer, density of NPs, and plasmon frequency were optimized to achieve the brightest RTP through most efficient LSPR. We

showed that phosphorescent radiative decay became faster, and phosphorescent intensity was increased by up to 2.8 times in the case of AuNP-55 nm, whose plasmon frequency corresponds to the phosphorescence wavelength. This study may enable bright phosphorescence in electric luminescence devices integrated with plasmonics, which can enhance radiative decay as well as improve light extraction from the device.

We developed a molecular design principle consisting of a phosphorescent ligand for MOFs and demonstrated bright phosphorescence from the phosphor ligand of the MOF–PS composite. The phosphor and ligand construction components should not be connected through π-conjugation because the construction component can alter the intrinsic phosphorescence properties of the phoshor if π-conjugated. To suppress the vibration of the phosphor in MOFs, the phosphor component must be held by the polymer matrix and linkage on frameworks. We discovered that intramolecular collision quenching between the chromophore and the MOF frame causes significant vibration quenching, even at low temperature. By suppressing vibrational motion of chromophore component by filling polystyrene into the MOF, we successfully demonstrated bright RTP from the resulting MOF–PS composite. The photophysical data showed that phosphorescent radiative decay was enhanced. This work suggests a new feasible strategy to both suppress vibration and enhance radiative decay, which improves the brightness of phosphorescence.

The following is the list of peer-reviewed journal papers published based on my PhD research and research collaboration at the University of Michigan.

1. **Jung, J.**, Kwon, MS., Gierschner, J., Millan, B., Kim, J. **, "**Molecular Design for Fluorene Based Metal-free Phosphors in Amorphous Polymer Matrices" , in preparing manuscript. (Chapter 2)
2. Wang$^{(+)}$, H., **Jung$^{(+)}$, J.**, Chung, K, Lim, JW., You, Y., Kim*, J., and Kim*, D., "Optimization Of Coupled Plasmonic Effects for Viable Phosphorescence of Metal-Free Purely Organic Phosphor", *J. Appl. Phys*, **2017**, 122, 153103. (Chapter 3)
3. Lee$^{(+)}$, D., Ma$^{(+)}$, X., **Jung$^{(+)}$, J**., Jeong, E.J., Hashemi, H., Bregman, A., Kieffer, J. and Kim, J., "The Effects of Extended Conjugation Length of Purely Organic Phosphors on their Phosphorescence Emission Properties." *Phys. Chem. Chem. Phys.* **2015**, 29 19096-19103.
4. Yu, Y., Kwon, M.S., **Jung, J**., Zeng, Y., Kim, M., Chung, K., Gierschner, J., Youk, J.H.,

Borisov, S.M. and Kim, J., "Room Temperature Phosphorescence based Dissolved Oxygen Detection by Core-shell Polymer Nanoparticles Having Metal-Free Organic Phosphor." *Angew. Chem. Int. Ed.* **2017**, 129, 16425-16429.

4. Sarkar, S., Hendrickson, H.P., Lee, D., DeVine, F., Jung, J., Geva, E., Kim, J. and Dunietz, B.D., "Phosphorescence in Bromobenzaldehyde can be Enhanced through Intramolecular Heavy Atom Effect.", *J. Phys. Chem. C* **2017**, 121, 3771-3777.
5. Seo, C., Lee, J., Kim, MS., **Jung, J.**, Shin*, H., An, T., Sun, G., Kim*, J., and Kim*, J., "Plasmon-enhanced Phosphorescence of Hybrid Thin Films of Metal-free Purely Organic Phosphor and Silver Nanoparticles", *Chem. Phys. Lett.* **2017**, 676,134.
6. Chung, K., Yang, DS., **Jung, J.**, Seo, D., Kwon, MS., and Kim, J., "A Novel Mechanism for Chemical Sensing based on Solvent-fluorophore-Substrate Interaction: Highly Selective Alcohol and Water Sensor with Large Fluorescence Signal Contrast", *ACS Appl. Mater. & Interfaces* **2016**, 8,28124.
7. Kwon, M.S., Yu, Y., Coburn, C., Phillips, A.W., Chung, K., Shanker, A., **Jung, J**., Kim, G., Pipe, K., Forrest, S.R. Youk, J.H., Gierschner, J., and Kim, J., "Suppressing Molecular Motions for Enhanced Room-temperature Phosphorescence of Metal-Free Organic Materials.", *Nat. Commun.* **2015**, 6, 1-9.
8. Bolton, O., Lee, D., **Jung, J**. and Kim, J., "Tuning the Photophysical Properties of Metal-free Room Temperature Organic Phosphors via Compositional Variations in Bromobenzaldehyde/Dibromobenzene Mixed Crystals.", *Chem. Mater*. **2014**, 26, 6644-6649.
9. Kwon, M.S., Lee, D., Seo, S., **Jung, J.** and Kim, J., ""Tailoring Intermolecular Interactions for Efficient Room-Temperature Phosphorescence from Purely Organic Materials in Amorphous Polymer Matrices.", *Angew. Chem. Int. Ed*. **2014**, 53, 11177-11181.

5.2 Future considerations

The works presented in my dissertation opens a promising new path to develop emerging applications for phosphorescent materials. However, the utility of these phosphors is limited for real applications. For example, even though we suggested a color tuning strategy without significantly reducing the QY of phosphorescence, the range of color is blue to yellow-green, which cannot penetrate skin, implying that these phosphors would be difficult to be used in

bio-applications such as imaging. Because red or near infrared phosphors can penetrate skin, developing low-bandgap phosphors is promising for the field of bio-imaging.

Although we synthesized a series of phosphorescent molecules and obtained a great deal of photophysical data from this series, the computational data could not clearly explain the experimental data. Unlike the simulation of fluorescent molecules that are simply correlated to their experimental data, many PL processes are involved in phosphorescence, which the computation must consider. Moreover, the time-dependent properties of phosphorescence processes such as ISC and nonradiative decay further complicate the computation. A new powerful computational tool for phosphorescence will help us to understand the mechanism of the phosphorescence from organic molecules as well as to predict the phosphorescent properties of newly designed molecules.

We attempted to incorporate surface plasmon into organic lighting-emitting diodes (OLEDs), but progress has been slow. Our group's alumni have attempted to fabricate solution-processed devices, but their results were not attractive yet. We established the device set-up and attempted to optimize OLEDs from derivatives of the BrFL molecule. With a highly thermally stable molecule, we fabricated the device by vacuum deposition method. The BrFL-molecule-based device was able to achieve bright electro-phosphorescence with a high internal quantum efficiency (IQE), but unwanted emission from electron transfer or hole transfer layer had to be removed. The balance of hole and electron recombination in the emitting layer may be solved by the changing materials for the hole transfer layer. Next, we can adapt the optimization conditions of LSPR-enhanced phosphorescence from Chapter 3 into OLEDs in order to improve the IQE and light extraction.

Work to integrate our phosphors into MOF–PS composite has begun in earnest, although potential applications have not been demonstrated. MOFs have the advantage of being highly porous compared to polymer systems. The idea of using phosphorescent MOFs in this way is quite interesting because it can be utilized as a hypersensitive oxygen indicator or for singlet oxygen generation[7]. Unfortunately, Zn-based MOFs are sensitive to humidity and are destroyed by water. Thus, the development of phosphorescent MOFs that are stable under ambient conditions should be devised for potential applications of MOFs

Finally, the phosphorescent decay temperature in doped polymer films must be thoroughly investigated. In Chapter 4, BrFL6 exhibited a phosphorescent intensity drop around 350 K, which is higher than room temperature and is one of the highest temperatures

reported thus far[8]. Interestingly, the temperature of phosphorescent decay of BrFL1 is the α-relaxation temperature in PMMA, in contrast to reported phosphors including benzophenone, which exhibits phosphorescent decay in PMMA at the β-relaxation temperature. In addition, the temperature of phosphorescent decay of BrFL6 is the β-relaxation temperature in PMMA but the α-relaxation temperature in PS, not the γ-relaxation temperature at which the phosphorescence intensity of benzophenone drops. Depending on the conditions of the polymer film (e.g., precipitation or under high vacuum), BrFL6 shows various decay temperatures in PS. To the best of our best knowledge, this phenomenon has not been reported thus far. The accumulated database of phosphorescent decay temperatures depending on the phosphors and polymers will provide guidelines for what polymer and phosphors should be chosen for specific applications.

5.3 References

1. Hirata, S., Totani, K., Zhang, J., Yamashita, T., Kaji, H., Marder, S.R., Watanabe, T. and Adachi, C., "Efficient Persistent Room-temperature Phosphorescence in Organic Amorphous Materials under Ambient Conditions." *Adv. Funct. Mater.* **2013**, 23, 3386-3397
2. Kwon, M.S., Lee, D., Seo, S., Jung, J. and Kim, J., "Tailoring Intermolecular Interactions for Efficient Room-Temperature Phosphorescence from Purely Organic Materials in Amorphous Polymer Matrices.", *Angew. Chem. Int. Ed*. **2014**, 53 11177-11181
3. Baldo, M.A., O'brien, D.F., You, Y., Shoustikov, A., Sibley, S., Thompson, M.E. and Forrest, S.R., "Highly Efficient Phosphorescent Emission from Organic Electroluminescent Devices." *Nature* **1998**, 395, 151-154.
4. Zhang, G., Palmer, G.M., Dewhirst, M.W. and Fraser, C.L., "A Dual-emissive-materials Design Concept Enables Tumour Hypoxia Imaging." *Nat. Mater.* **2009**, 8, 747-751.
5. Hirata, S., "Recent Advances in Materials with Room Temperature Phosphorescence: Photophysics for Triplet Exciton Stabilization." *Adv. Opt. Mater.* **2017**, 5, 1700116
6. Kwon, M.S., Yu, Y., Coburn, C., Phillips, A.W., Chung, K., Shanker, A., Jung, J., Kim, G., Pipe, K., Forrest, S.R. Youk, J.H., Gierschner, J., and Kim, J., "Suppressing Molecular Motions for Enhanced Room-temperature Phosphorescence of Metal-free Organic Materials.", *Nat. Commun.* **2015**, 6, 1-9
7. Bolton, O., Lee, K., Kim, H.J., Lin, K.Y. and Kim, J., "Activating Efficient Phosphorescence from Purely Organic Materials by Crystal Design." *Nat. Chem.* **2011**, 3, 205-210.
8. Mieno, H., Kabe, R., Notsuka, N., Allendorf, M.D. and Adachi, C., "Long-Lived Room-Temperature Phosphorescence of Coronene in Zeolitic Imidazolate Framework ZIF-8." *Adv. Opt. Mater.* **2016**, 4, 1015-1021.